Perpendicular magnetic anisotropy of Co/Pt multilayers on $BiFeO_3$ thin films

Yanjiang Ji
University of Leeds
School of Physics and Astronomy

Submitted in accordance with the requirements for the degree of
Doctor of Philosophy

August, 2022

Intellectual Property Statement

The candidate confirms that the work submitted is his own and that appropriate credit has been given where reference has been made to the work of others.

Acknowledgements

I would like to express my sincere gratitude to my main supervisor at Leeds, Dr. Thomas Moore, for his advice and encouragement during my PhD. I'd like to thank Dr. Thomas Moore for his invaluable advice and comments on reports, project meetings, and thesis writings. I would also like to thank my co-supervisor at Leeds, Prof. Andrew Bell, for his valuable discussions, physical insights, and experience on my project. Additionally, I am grateful to my supervisor at SUSTech, Prof. Lang Chen, for his patience, motivation, and understanding during my studies at Shenzhen.

All the lab works owe much to Dr. Philippa Shepley, Dr. Mannan Ali and Dr Timothy Moorsom at Leeds. I have spent a wonderful year at the Condensed Matter Physics group at Leeds. I would also like to thank Prof. Bryan Hickey, Dr. Gavin Burnell and Prof. Chris Marrows for their comments, questions and helpful suggestions for my transfer report and APR report.

I am also grateful to all the group members at Prof. Lang Chen's lab at Shenzhen, especially Dr. Zedong Xu, Dr. Qi Liu, Dr. Songbai Hu, and Dr. Cai Jin.

Abstract

Pt/Co/Pt trilayers with perpendicular magnetic anisotropy (PMA) were obtained on epitaxial $BiFeO_3$ (BFO) films. The effect of seed Pt thickness on magnetic anisotropy of Pt/Co/Pt trilayers has been investigated. Using as-deposited $BiFeO_3$ films on 16-nm $Ca_{0.96}Ce_{0.04}MnO_3$ (CCMO) buffered $LaAlO_3$ (LAO) substrates, we sputtered Pt(t_{Pt} nm)/Co(0.7 nm)/Pt(4 nm) trilayers on BFO films. PMA is achieved for seed Pt layer as thin as ~ 0.9 nm. Both the coercive field (H_{c}) and the anisotropy field (H_{A}) increase as the seed Pt layer thickness increases. Magnetic properties of Pt/Co/Pt trilayers on pure T-like phase BFO and mixed phase BFO are studied by both superconducting quantum interference vibrating sample magnometer (SQUID-VSM) and anomalous Hall effect (AHE) measurements. The magnetic anisotropy energies (MAE) of these samples are derived from the planar Hall effect (PHE) measurements. We find that the MAE of Pt/Co/Pt on pure T-like phase BFO is larger than that of Pt/Co/Pt on mixed phase BFO. The decrease of MAE of Pt/Co/Pt on mixed phase BFO can be explained by larger surface roughness of mixed phase BFO.

To enhance the coupling between the ferromagnetic layer (Co) and the multiferroic layer (BFO), we sputtered Co(0.7 nm)/Pt(4 nm) bilayers directly on BFO without using a Pt seed layer. These bilayers exhibited slanted hysteresis curves and weak PMA at room temperature. To increase the PMA, we reduce the Co layer thickness to 0.5 nm, which is paramagnetic at room temperature. Perfect square shaped hysteresis loops were attained for Co(0.5 nm)/Pt(4 nm) bilayers when the temperature was lowered below 200 K. In contrast to Pt/Co/Pt trilayers on BFO, the Co/Pt bilayers on mixed phase BFO demonstrated a greater PMA than those on pure T-like phase BFO, indicating that the coupling effect between the Co layer and the BFO layer surpassed the influence of BFO layer roughness. To achieve PMA at room temperature and preserve the direct coupling between the cobalt layer and the BFO layer, we fabricated $[\mathrm{Co}(0.5\ nm)/\mathrm{Pt}(1.2\ nm)]_4$ multilayers on BFO, with the first cobalt layer directly sputtered onto BFO. AHE measurements confirmed the successful achievement of PMA for this structure at room temperature.

Freestanding oxide nanomembranes is a promising technological route for functional oxides to integrate with the main frame silicon based technology. In the final part of this research, a new sacrificial material – $SrCoO_{2.5}$ – is used for fabricating the freestanding BFO film with a Pt/Co/Pt trilayer structure. After releasing from the substrate, the freestanding BFO film with a capping Pt/Co/Pt trilayer structure was transferred to a silicon wafer. The SQUID-VSM measurement of the transferred sample indicated that the PMA is preserved for the freestanding procedures.

Contents

1 Introduction **1**

1.1 The Boltzmann's tyranny 2

1.2 Magneto-electric spin-orbit (MESO) logic device 3

1.3 Pt/Co thin films with PMA 3

1.4 Thesis overview 4

2 Theoretical Background **5**

2.1 Introduction 6

2.2 Multiferroic materials 6

2.3 Misfit strain and BFO phases 8

2.3.1 Lattice mismatch and strain engineering 8

2.3.2 Epitaxial BFO thin films of different phases 8

2.4 Exchange interaction and magnetic anisotropy 10

2.4.1 Exchange interaction 10

2.4.2 Spin-orbit interaction 11

2.4.3 Anisotropy energy 12

2.4.4 Spin models 14

2.5 Summary 19

3 Experimental methods **20**

3.1 Introduction 21

3.2 Sample Fabrication 21

3.2.1 Pulsed Laser Deposition 21

3.2.2 DC Magnetron Sputtering 23

3.3 Structures and Characterizations 24

3.3.1 X-ray diffraction (XRD) 24
3.3.2 X-Ray Reflectivity (XRR) 27
3.3.3 Atomic Force Microscopy (AFM) 29
3.4 Magnetometry 30
3.4.1 Anomalous Hall effect (AHE) Magnetometry 30
3.4.2 SQUID-VSM 32
3.5 Summary 33

4 Pt/Co/Pt trilayers on epitaxial BiFeO$_3$ thin films 34
4.1 Introduction 35
4.2 Samples and Characterizations 35
4.2.1 Epitaxial growth of BiFeO$_3$ films on Ca$_{0.96}$Ce$_{0.04}$MnO$_3$/LaAlO$_3$. 35
4.2.2 DC sputtering of Pt/Co/Pt trilayers on BFO 49
4.3 Magnetic Characterization 50
4.3.1 Magnetic properties of Pt(t$_{\mathrm{Pt}}$ nm)/Co(0.7 nm)/Pt(4 nm) trilayers on BFO 50
4.3.2 Magnetic properties of Pt(0.9 nm, 1.2 nm)/Co(0.7 nm)/Pt(4 nm) trilayers on BFO with different thicknesses 57
4.4 Summary 60

5 Co/Pt multilayers on BFO without the seed Pt layer 62
5.1 Introduction 63
5.2 Samples and Characterization 63
5.2.1 X-ray diffraction and structural characterization 64
5.2.2 XAS measurements 71
5.3 Magnetic characterization 73
5.3.1 Magnetic Properties of Co(0.7 nm)/Pt(4 nm) double layers on BFO 74
5.3.2 Magnetic Properties of Co(0.5 nm)/Pt(4 nm) double layers on BFO 78
5.3.3 Magnetic Properties of [Co(0.5 nm)/Pt(1.2 nm)]$_4$/Pt(2.8 nm) multilayers on BFO 90
5.4 Summary 93

6 Freestanding Pt/Co/Pt/BFO films **95**
6.1 Introduction 96
6.2 Samples and Characterizations 97
6.2.1 Epitaxial growth of BFO films on SCO/SRO buffered STO substrates 97
6.2.2 DC sputtering of Co/Pt multilayers on BFO/SCO/SRO samples 99
6.2.3 Fabrication of FM/BFO freestanding membranes 99
6.2.4 X-ray diffraction and structural characterization 101
6.3 Magnetic Characterization 104
6.4 Summary 107

7 Conclusions **109**
7.1 Summary 110
7.2 Future Work 111

References **113**

List of Figures

2.1 Sketch of the relation between tetragonal (T), orthorhombic (O), rhombhedral (R), and $M_\mathrm{A}, M_\mathrm{B}, M_\mathrm{C}$ phases. Arrows represent the directions of the spontaneous polarization **P**. (Figure is a reproduction from: Zuhuang Chen, et al., Phys. Rev. B **88**, 054114, 2013.) 10

3.1 Diagram of pulsed laser deposition (Figure is a reproduction from Wikimedia Commons, the free media repository). 22
3.2 Schematic of magnetron sputtering. 23
3.3 Schematic illustration of Bragg's Law (Figure is a reproduction from Wikimedia Commons, the free media repository). 24
3.4 (a) Symmetrical-reflection measurement and (b) asymmetrical-reflection measurement for out-of-plane XRD. (Figure is a reproduction from: Toru Mitsunaga, The Rigaku Journal, **25** (1), 2009.) 26
3.5 Schematic of fcc Pt structure with (111) plane (purple) running parallel with the film surface where the grey balls represent the Pt atoms. The incidence X-ray (dashed black line) comes from right to the left and is scattered by the (220) plane (blue). The green plane represents the (200) plane. This figure is generated using VESTA (Visualization for Electronic and Structural Analysis) software. 26

3.6 Log intensity plot of the XRR for Pt/Co/Pt sputtered on $BiFeO_3$ (BFO) thin film on $Ca_{0.96}Ce_{0.04}MnO_3$ (CCMO) buffered $LaAlO_3$ (LAO) substrates (open red squares), the fitted structure via GenX (blue curve) is Pt(4.5)/Co(0.7)/ Pt(1.2)/BFO(20.0)/CCMO(15.9)/LAO (numbers in parentheses are nominal thicknesses in nanometer throughout the thesis, unless stated otherwise). 28

3.7 (a) Schematic of AFM. (b) Schematic of PFM: the sample expands when the polarization of the domain is parallel to the applied electric field. . . 30

3.8 Geometry of the AHE measurement. (Figure is a reproduction from: J. R. Lindemuth et al., Anomalous Hall Effect Magnetometry, Lake Shore Cryotronics, Inc.) 31

3.9 SQUID detection schematic. (Figure is a reproduction from: MPMS 3 User's Manual) 33

4.1 (a) X-ray θ-2θ scans of the BFO films of various thicknesses grown on CCMO buffered LAO substrates. (b) Thickness dependence of the c-axis lattice constants of the T-like phase BFO on CCMO buffered LAO substrates. 37

4.2 Thickness of the BFO/CCMO structure sample can be simulated from the X-Ray Reflectivity (XRR) data (a) and checked by TEM imaging (b). Thickness of the Pt/Co/Pt structure is determined from the growth rate of Pt and Co and checked by EDX line profile (c, d). 38

4.3 XRR of a thin BFO film (a) and a thick BFO film (b) grown on CCMO buffered LAO substrates. Their thicknesses are determined to be 17.6 nm and 54.3 nm, respectively. 39

4.4 X-ray reciprocal space mapping (RSM) plots along ($\bar{1}03$) direction for BFO(17 nm), BFO(23 nm), BFO(38 nm), BFO(43 nm), BFO(54 nm) and BFO(77 nm) on 16nm-CCMO buffered LAO substrates are presented in (a)-(f), respectively. The atomic force microscopy (AFM) images for (a)-(f) are (g)-(l), respectively. 40

4.5 Schematic of (a) the M_C-type monoclinic unit cell and (b) reciprocal-space maps around the ($h0l$) reflection for the monoclinic M_C phase. . . 41

4.6 (a) X-ray $\theta-2\theta$ scans for mixed phase BFO on LAO and CCMO buffered LAO, respectively. RSM($\bar{1}03$) scans for mixed phase BFO on LAO (b) and CCMO buffered LAO (c), respectively. AFM topography images for mixed phase BFO on LAO (d) and CCMO buffered LAO (e), respectively. 43

4.7 Atomic force microscopy topography image of a pure T-like phase BFO sample (a) and a mixed phase BFO sample (b). (c) Cross-section line profile along the red line in (a). (d) Cross-section line profile along the blue line in (b). Both lines are perpendicular to the steps on BFO. . . . 44

4.8 PFM of out-of-plane phase image (a) and amplitude image (b) of the BFO film under electrically writing of ± 5V. Local PFM hysteresis loop: phase signal (c) and amplitude signal (d). 45

4.9 M vs H hysteresis curves for (a) BFO(40)/LAO and (b) BFO(43.6)/CCMO(15)/ LAO measured at room temperature, respectively. (c) Field cooled (FC) out-of-plane measurement of M vs T for Pt(4)/Co(0.7)/Pt(0.9) on BFO(20)/CCMO(15)/ LAO measured at the field of 50 Oe. 48

4.10 AHE signal for Pt/Co/Pt trilayer on as-deposited BFO film (S1) which has the most perfect square-shaped hysteresis loop. AHE signal for Pt/Co/Pt trilayer on acetone cleaned BFO film exposed in air for 5 hours (S2) has a deteriorated square-shaped hysteresis loop. AHE signals for Pt/Co/Pt trilayers on acetone cleaned BFO films exposed in air for 10 days (S3) and 100 days (S4) have more slant-shaped hysteresis loops. AHE signal for Pt/Co/Pt trilayer on ultrasonic acetone cleaned BFO film exposed in air for 300 days (S5) has a much improved square-shaped hysteresis loop. AHE signal for Pt/Co/Pt trilayer on untreated BFO film exposed in air for 300 days (S6) has the most slant-shaped hysteresis loop. 51

4.11 AHE signals for Pt(t_{Pt})/Co(0.7)/Pt(4) trilayers with different thicknesses of seed Pt layer on (a) pure T-like phase BFO thin films and (b) mixed-phase BFO thin films, respectively. Square-shaped AHE hysteresis loops are obtained for all Pt seed layer thicknesses except for the thinnest 0.6 nm case. (c) The coercive field (H_{c}) drops monotonously as the Pt seed layer thickness decreases. The dashed blue line in the figure is a guide to the eye. 53

4.12 Anisotropy field derived from (a) AHE measurement and (b) in-plane SQUID-VSM measurement. 54
4.13 (a) Anisotropy field for Pt(t_{Pt} nm)/Co(0.7 nm)/Pt(4 nm) on T-like phase BFO (open black dots) and mixed phase BFO (open red dots), respectively. (b) The effective perpendicular anisotropy (K_{eff}) rises as the Pt seed layer thickness increases, and it becomes saturated when the Pt layer thickness is $\sim$ 2 nm. (c) The intrinsic perpendicular anisotropy (K_u), drops when the Pt seed layer thickness decreases. 55
4.14 (a) Coercive fields H_{c}, (b) anisotropy fields H_{A}, (c) effective perpendicular magnetic anisotropies K_{eff} and (d) intrinsic perpendicular magnetic anisotropies K_u of Pt(0.9, 1.2)/Co(0.7)/Pt(4) trilayers on BFO thin films with different thicknesses. 58
4.15 The AFM surface morphology images of (a) 19 nm-BFO, (b) 52 nm-BFO and (c) 69 nm-BFO samples, respectively. (d) Anisotropy fields H_{A} of Pt(1.2)/Co(0.7)/Pt(4) trilayers on 19 nm-BFO, 52 nm-BFO and 69 nm-BFO thin films. (e) The sheet intrinsic perpendicular magnetic anisotropies $t \cdot K_u$ vs $2\sigma/W$ plot of Pt(1.2)/Co(0.7)/Pt(4) trilayers on 19 nm-BFO, 52 nm-BFO and 69 nm-BFO thin films. 59

5.1 (a) GIXRD plots with a fixed incident angle of 0.5° for Pt(t)/Co(0.7)/Pt on pure T-like phase BFO with different Pt seed layer thicknesses of 2 nm (blue line), 1 nm (red line) and 0 nm (black line). (b) GIXRD plots with a fixed incident angle of 0.5° for Co(0.5)/Pt on mixed phase BFO (green line), Co(0.5)/Pt on pure T-like phase BFO (blue line), Co(0.7)/Pt on mixed phase BFO (red line) and Co(0.7)/Pt on pure T-like phase BFO (black line), respectively. The peak positions of fcc Pt (111), (200) and (220) are labelled as the grey dashed lines. Other peaks appeared in the figure are due to the BFO/CCMO/LAO heterostructures which are not relevant for studying the polycrystalline Pt texture. 66
5.2 The AFM images of a pure T-like phase BFO thin film (a) before and (b) after the Pt(1.2)/Co(0.7)/Pt(4) trilayer deposition via DC sputtering. 66

5.3 (a)XRD $\theta - 2\theta$ scans of a pure T-like phase BFO thin film (red curve) and a mixed-phase BFO thin film (black curve) on CCMO buffered LAO substrates. (b) XRR scans of Co/Pt double layers on a pure T-like phase BFO film (red curve) and a mixed-phase BFO film (black curve). Combining the growth rate estimation with the XRR fringe positions, the complete structures are determined to be BFO(17)/Co(0.7)/Pt(4.8) (red curve) and BFO(45)/Co(0.7)/Pt(4.8) (black curve), respectively. AFM images for (c) BFO(17)/Co(0.7)/Pt(4.8) and (d) BFO(45)/Co(0.7)/Pt(4.8). 68

5.4 XRR scan raw data (open black square) and the fitting (red curve) for the Co/Pt bilayer on a pure T-like BFO film. The model structure used for fitting is LAO/CCMO(15.0)/BFO(17.5)/CoO(0.4)/Co(0.7)/Pt(4.7), and the fitting parameters are listed in Table (5.1). 69

5.5 (a) XRD $\theta - 2\theta$ scans of a pure T-like phase BFO thin film (red curve) and a mixed-phase BFO thin film (black curve) on CCMO buffered LAO substrates. (b) XRR scans of Co/Pt double layers on a pure T-like phase BFO film (red curve) and a mixed-phase BFO film (black curve). Combining the growth rate estimation with the XRR fringe positions, the complete structures are determined to be BFO(21)/Co(0.5)/Pt(4.0) (red) and BFO(52)/Co(0.5)/Pt(4.0) (black curve), respectively. AFM images for (c) BFO(21)/Co(0.5)/Pt(4.0) and (d) BFO(52)/Co(0.5)/Pt(4.0). 70

5.6 XRR scan raw data (open black square) and the fitting (red curve) for the Co/Pt bilayer on a pure T-like BFO film. The model structure used for fitting is Pt(4.0)/Co(0.4)/CoO(0.3)/BFO(21.5)/CCMO(17.4)/LAO, and the fitting parameters are listed in Table (5.1). 71

5.7 Normalized XAS spectra at the Co L_3 edge showing the oxidation state of ultra thin Co films on pure T-like BFO and mixed-phase BFO films. . 73

5.8 Normalized M vs H hysteresis curves for (a) Co(0.7)/Pt bilayer and (b) Pt(0.6)/Co(0.7)/Pt trilayer on pure T-like phase BFO thin films at room temperature. 75

5.9 The magnetic moment $\mathrm{M}_S \cdot V$ vs cobalt thickness t plot for $5 \times 3\ mm^2$ Co(t)/BFO samples. A linear fit towards zero magnetic moment allows to determine the nominal t_{MDL}. 75

5.10 (a) Temperature dependent AHE signals for Co(0.7)/Pt(4.8) on a pure T-like phase BFO film (black curves) and a mixed-phase BFO film (red curves). Dependence of H_c on temperature for Co(0.7)/Pt(4.8) on (b) a pure T-like phase BFO film and (c) a mixed-phase BFO film. 77

5.11 Temperature dependence field cooled (FC) out-of-plane magnetized magnetization M measured at 50Oe for (a) Co(0.5)/Pt(4) bilayer (black curve) and (b) Pt(1.2)/Co(0.5)/Pt(4) trilayer (red curve) on pure T-like phase BFO films. 79

5.12 Temperature dependent AHE signals for Co(0.5)/Pt(4) on a pure T-like phase BFO film (black curves) and a mixed phase BFO film (red curves). 81

5.13 (a) Temperature dependence of anisotropy fields (H_A) for Co(0.5)/Pt bilayers sputtered on pure T-like phase BFO film (red) and mixed phase BFO film (black), respectively. (b) Log-log plot of the $K_u(T)/K_u(50K)$ vs $M_S(T)/M_S(50K)$ for Co(0.5)/Pt(4) bilayer sputtered on T-like BFO. 83

5.14 (a) Temperature dependences of anisotropy fields H_A for Pt(0.9)/Co(0.7)/Pt(4) on pure T-like phase BFO film (red) and mixed-phase BFO film (black), respectively. (b) Coercive fields H_c for Pt(0.9)/Co(0.7)/Pt(4) on pure T-like phase BFO film (red) and mixed phase BFO film (black), respectively. (c) Field cooled (FC) magnetization (M) vs Temperature (T) curve for Pt(0.9)/Co(0.7)/Pt(4) on pure T-like phase BFO film. (d) Log-log plot of the $K_u(T)/K_u(10K)$ vs $M_S(T)/M_S(10K)$ for Pt(0.9)/Co(0.7)/Pt(4) trilayer sputtered on T-like BFO. 85

5.15 $H_n^{1/2}$ versus H_x plots of Co(0.5)/Pt bilayers on mixed phase and pure T-like phase BFO thin films at 100K. 89

5.16 (a) XRD $\theta - 2\theta$ scans of a pure T-like phase BFO thin film (red curve) and a mixed phase BFO thin film (black curve) on LAO substrates. (b) XRR scans of $[\mathrm{Co}(0.5)/\mathrm{Pt}(1.2)]_4/\mathrm{Pt}(2.8)$ multilayers on a pure T-like phase BFO film (red curve) and a mixed phase BFO film (black curve). AFM images for $[\mathrm{Co}(0.5)/\mathrm{Pt}(1.2)]_4/\mathrm{Pt}(2.8)$ multilayers covered (c) pure T-like phase BFO and (d) mixed phase BFO films. 91

5.17 (a) AHE signals for $[\mathrm{Co}(0.5)/\mathrm{Pt}(1.2)]_4$ multilayers on pure T-like phase BFO (black curve) and mixed phase BFO (red curve). (b) Temperature dependences of coercive fields H_c for $[\mathrm{Co}(0.5)/\mathrm{Pt}(1.2)]_4$ multilayers on pure T-like phase BFO (black square) and mixed phase BFO (red circle). 92

6.1 Design and fabrication of freestanding Pt/Co/Pt/BFO heterotructures. (a) Schematic illustration of the sputtering, exfoliation and transfer process with SCO as the sacrificial layer. (b) The pseudocubic in-plane lattice parameters of SCO (sacrificial material), STO (substrate), SRO and BFO. (c) The surface morphology of as-grown Pt/Co/Pt/BFO on SCO/SRO/STO(100). (d) The surface morphology of SRO/STO(100) after exfoliation. (e) Optical image of freestanding Pt/Co/Pt/BFO nanomembrane grown on SCO/SRO/STO(001) transferred to a $\mathrm{SiO_2}$/Si substrate. (e) The surface morphology of freestanding Pt/Co/Pt/BFO after exfoliation. 98

6.2 XRD $\theta - 2\theta$ plots of the as-grown BFO/SCO/SRO thin film (red curve) and detached SRO/STO film (black curve). The grey dashed line, blue dashed line and black dashed line are used to represent peak positions of BFO (002), SRO (002) and STO (002), respectively. 100

6.3 (a) XRD $\theta - 2\theta$ scans of the as-grown Pt/Co/Pt/BFO/SCO/SRO films on STO substrate (red) and the freestanding Pt/Co/Pt/BFO nanomembrane. (b) Reciprocal space mapping results of the as-grown Pt/Co/Pt/BFO strained film on SCO/SRO buffered STO (001) substrate measured around the STO ($\bar{1}03$) plane and (c) the corresponding freestanding nanomembrane measured around the BFO ($\bar{1}03$) plane. What is more, the freestanding BFO thin film is fully relaxed due to the calculation of the in-plane lattice constant a. 102

6.4 XRD $\theta - 2\theta$ scan around the BFO($\bar{1}03$) diffraction peak. 103

6.5 Specular XRR pattern of the freestanding Pt/Co/Pt/BFO membrane. . 104

6.6 (a) Normalized M vs H hysteresis curves measured at room temperature for as-grown Pt/Co/Pt/BFO/SCO/SRO thin film measured by AHE (red) and freestanding Pt/Co/Pt/BFO nanomembrane measured by SQUID-VSM (black). (b) Normalized M vs H hysteresis curves measured at room temperature for as-grown Pt/Co/BFO/SCO/SRO thin film measured by AHE (red) and freestanding Pt/Co/BFO nanomembrane measured by SQUID-VSM (black). 106
6.7 (a) Field cooled (FC) M vs T measurements for freestanding Pt/Co/Pt/BFO (red curve) and Pt/Co/BFO (black curve) nanomembranes. (b) M vs H measurements for freestanding Pt/Co/Pt/BFO (red curve) and Pt/Co/BFO (black curve) nanomembranes at 10 K. 106

List of Tables

2.1 Misfit strains of BFO calculated for some substrates. 9

3.1 Growth condition for BFO on CCMO buffered LAO substrate. 22

3.2 GenX fitting for Pt/Co/Pt on BFO sample in Figure (3.6), where d represents the thickness of each layer and σ represents the roughness of each layer. 29

4.1 Results of fitting XRR data of BFO samples in Figure 4.2 (a), Figure 4.3 (a) and (b), where d represents the thickness of each layer and σ represents the roughness of each layer. 37

4.2 The lattice parameters of M_C phase extracted from the RSMs in Figure (4.4). 42

5.1 Results of fitting XRR data of BFO/Co(t)/Pt samples in Figure (5.4) and Figure (5.6), where d represents the thickness of each layer and σ represents the roughness of each layer. 72

5.2 Exchange stiffnesses of Co(0.5)/Pt and Pt(0.9)/Co(0.7)/Pt on T-like BFO fitted by different approaches. 88

6.1 Growth condition for BFO on SCO/SRO buffered STO (100) substrate. 98

Abbreviations

AFM	Atomic force microscope
AHE	Anomalous Hall effect
BCC	Body center cubic
BFO	Bismuth ferrite oxide
CCMO	Cerium-doped manganese oxide
CMOS	Complementary metal-oxide semiconductor
DC	Direct current
DMI	Dzyaloshinskii-Moriya interaction
DW	Domain wall
FCC	Face center cubic
FE	Ferroelectric
FM	Ferromagnetic
GIXRD	Grazing-incidence X-ray diffraction
HCP	Hexagonal close packed
IP	In-plane
LAO	Lanthanum aluminate
MAE	Magnetic anisotropy energy
MDL	magnetic dead layer
MESO	Magnetoelectric spin-orbit
OOP	out-of-plane
PFM	Piezoresponse force microscopy
PMA	Perpendicular magnetic anisotropy
PLD	Pulsed laser deposition
RKKY	Ruderman-Kittel-Kasuya-Yosida
RSM	Reciprocal space mapping
RT	room temperature
SQUID	Superconducting quantum interface device
SOC	Spin-orbit coupling
STO	Strontium titanate
TEM	Transmission electron microscopy
XAS	X-ray absorption spectroscopy
XRD	X-ray diffraction
XRR	X-ray reflectometry
ME	multiferroic
UHV	Ultra high vacuum
VSM	Vibrating Sample Magnetometry

CHAPTER 1

Introduction

Information technology industry has become the major driving force for the development of condensed matter physics. In the process of fulfilling the needs for industry, condensed matter physicists also identify new phenomena, reveal mechanisms, uncover principles and expand the frontiers in physics. Today, energy-efficient computing is drastically needed for mobile computing, the Internet of Things (IoT), artificial intelligence and autonomous driving. To store and manipulate information more energy efficiently, we need to design new devices, develop new processes and study new materials.

1.1 The Boltzmann's tyranny

Current computer technology is based on complementary metal-oxide-semiconductor (CMOS) transistors. It utilizes the transport properties of semiconductors for storing and manipulating the data. The ON current (I_{ON}) and OFF current (I_{OFF}) of the transistor is controlled by using an electric field applied across a high-quality insulating gate dielectric. Moore's law is an empirical law which describes a historical trend that the number of transistors in an integrated circuit (IC) doubles about every two years [1]. As the transistors get smaller, their power density stays constant, this is so called Dennard scaling [2]. To continue the Moore's law and Dennard scaling, we need to downsize the transistor and lower the supply voltage. Unfortunately, there are two limits set for the CMOS technology, one is the quantum tunneling which is evident when the transistor is on nanoscale size. Another one is Boltzmann's tyranny which is determined by the Boltzmann distribution law. The supply voltage cannot smaller than 60meV/decade [1] according to the Boltzmann's tyranny, which means we need to apply a 360 mV voltage across the dielectric to obtain 6 decades ($\frac{I_{\mathrm{ON}}}{I_{\mathrm{OFF}}} \sim 10^6$).

The Boltzmann's tyranny is dictated by the fundamental law of physics, which means we cannot surpass this limit by improving the material's property or optimizing the device structure. To make the more energy-efficient computing comes true, we need to use other physical mechanisms to encode the bit. One bit is the information unit of answering one YES/NO question. Order parameters of a bulk material such as electric polarization, magnetization and antiferromagnetic moment are natural choices for storing and manipulating the bits which could surpass the current CMOS technology.

---

[1] The supply voltage cannot smaller than 60meV/decade according to the Boltzmann distribution law. Considering: $\frac{I_{\mathrm{ON}}}{I_{\mathrm{OFF}}} < \exp(eV/k_B T)$, we get $V > \ln 10 \times \frac{k_B T}{e} \approx 60mV$.

1.2 Magneto-electric spin-orbit (MESO) logic device

Magneto-electric spin-orbit (MESO) is a newly proposed technological route for developing low energy cost logical devices. The electric field is applied across the multiferroic/ferroelectric material to switch the magnetization of adjacent ferromagnet through the electromagnetic coupling, then the change in magnetization is read out by the spin-orbit coupling component [3]. Using electric field instead of current, the MESO device of $10 \times 10\ nm^2$ size dissipates only about 1-10 aJ to switch the magnetization at room temperature, and the operating voltage is lowered to 100-300 mV. On the other hand, the Landauer's principle [4] dictates the minimum energy dissipation $k_B T \ln 2$ per bit operation for logically irreversible computation which is about 2.9×10^{-21} J at room temperature. The energy lost for MESO device (1-10 aJ) is at least 3 orders of magnitude larger than the Landauer limit.

The most promising multiferroic material for developing MESO device is bismuth ferrite ($BiFeO_3$, BFO) which is both ferroelectric and antiferromagnetic at room temperature. Many previous studies such as switching in magnetic tunnel junctions (MTJ) [5] and in multiferroic/ferromagnet heterostructures [6] combine BFO with magnetic multilayers of in-plane magnetic anisotropy (IPA). However, films with out-of-plane anisotropy or perpendicular magnetic anisotropy (PMA) which are more favorable for the real devices [7] have been rarely studied.

1.3 Pt/Co thin films with PMA

Multi-stacks with a structure of Pt/Co are usually used for PMA systems. When thickness of Co layer is small enough (between 4-10 Å), the interfacial effect caused by spin-orbit coupling between Co and Pt will exceed the shape anisotropy of Co, thus the easy axis of Co will be redirected from the in-plane direction to the perpendicular direction [8]. Another common structure for realizing PMA is MO_x/Co, where M represents Mg or Al. Extensive studies have been performed on the electric field control of PMA in MO_x/Co structures [9]. What is more, perpendicularly magnetized Pt/Co/Ir thin films have been intensively studied recently due to the opposite sign of Dzyaloshinskii-Moriya interaction (DMI) at Pt/Co and Co/Ir interfaces, which can stabilize and give more control of skyrmionic structures [10]. All of these advances make growing Pt/Co structure with PMA on multiferroic/ferroelectric material an important issue for developing not only MESO devices but also spin wave computing [11] and skyrmion computing [12].

Aside from the integration of multiferroic/ferroelectric material with the PMA layer, the integration of beyond-CMOS devices with current silicon-based CMOS technology is also vital for realizing the next generation energy-efficient computing.

1.4 Thesis overview

This report aims at integrating Co/Pt magnetic multilayers of different specifications with multiferroic $BiFeO_3$ thin films. Some basic concepts such as strain control of phase variants and multiferroic order parameters in $BiFeO_3$ thin films will be introduced first. The magnetic anisotropy and perpendicular magnetic anisotropy (PMA) in Co/Pt multilayers will also be introduced. Then the experimental methods for fabrication and characterization of the samples will be described in chapter 3.

The obtained results of this project are organized as three parts, each consists of a set of samples and their related characterization and measurements. Pt(t)/Co/Pt trilayers sputtered on pure T-like phase and mixed phase $BiFeO_3$ thin films are studied in Chapter 4. The phase variant and thickness of $BiFeO_3$ are determined through XRD and TEM. The seed Pt layer thickness and magnetic Co layer thickness are determined through growth rate and checked by XRR fitting. The magnetic properties of the samples are studied by SQUID-VSM and AHE measurements.

To enhance the couplings between multiferroic layer (BFO) and magnetic layer (Co), Co(x)/Pt bilayers grown directly on BFO are studied in Chapter 5. The temperature-dependent magnetic anisotropy has been studied through SQUID-VSM and AHE measurements. $[Co/Pt]_4$ magnetic multilayers are also grown on BFO without using the Pt seed layer, and a strong PMA is attained in this structure at room temperature.

In the last chapter on the results (Chapter 6), Pt/Co/Pt trilayers with PMA on freestanding BFO thin films are studied. Fabrication procedure of the freestanding Pt/Co/Pt/BFO nanomembrane is described in this chapter. The crystalline structure of BFO is studied by XRD before and after the freestanding procedure. The SQUID-VSM measurement of the freestanding Pt/Co/Pt/BFO nanomembrane reveals that the PMA survives the freestanding procedure.

Lastly, a summary of the results along with the possible future works of this project is given in Chapter 7.

Chapter 2

Theoretical Background

2.1 Introduction

In this chapter some of the theoretical concepts relating to the experimental results in this thesis will be introduced. Firstly, the basic concept of multiferroics will be briefly explained. Then, different phases, e.g. tetragonal, rhombohedral and orthorhombic phases of $BiFeO_3$ (BFO) thin films, obtained through strain engineering are discussed. Then, exchange interaction and magnetic anisotropies of Pt/Co thin films are introduced briefly. Lastly, spin models and spin wave theory are outlined concisely.

2.2 Multiferroic materials

Multiferroics are materials which exhibit multiple ferroic orders in the same phase, the ferroic orders can be ferromagnetism, ferroelectricity, ferroelasticity, and ferrotoroidity. The prefix ferro, meaning iron, was used to describe the material that can retain the order (usually a bulk property) when it is freed of the external applied stimulation such as magnetic field. The terminology is usually extended to include antiferromagnetism as one of the co-existed orders. For example, bismuth ferrite ($BiFeO_3$) as one of the most studied multiferroics exhibits a ferroelectric order, an antiferromagnetic order and a very weak ferromagnetic order.

Ferromagnetism and ferroelectricity are two macroscopic phenomena that can be observed in our daily life. People have known magnetism for several thousand years, iron is a ferromagnetic material which can be magnetized and attracted by lodestone (magnetite, a ferrimagnetic material). Iron nails magnetized by lodestone can attract each other even we put the lodestone away from them. Ferroelectricity has a relatively short history, it is first discovered in Rochelle salt by Joseph Valasek in 1920. The most studied and understood ferroelectric materials up to now are the ABO_3 perovskite oxides such as $BaTiO_3$ and $PbTiO_3$.

Ferromagnetism and ferroelectricity can be understood only on the basis of quantum mechanics. There is no magnetism in the context of classical physics according to the Bohr-Van Leeuwen theorem [13], the modern theory of ferromagnetism is based on the concepts of spin and exchange interaction. For ferroelectricity, the polarization is even ill-defined in a crystalline structure [14] without quantum mechanics, the modern theory of polarization is developed by R. Resta and D. Vanderbilt on the basis of Berry phase and Wannier function [15, 16]. The electronic contribution to the polarization of a crystalline structure is calculated through the expression of a Berry phase in reciprocal space, e.g. q_x, q_y and q_z [16].

$$P_x = \frac{2e}{(2\pi)^3} \int dq_y dq_z \gamma(q_y, q_z) = \frac{2ie}{(2\pi)^3} \sum_{n=1}^{n_b} \int d\mathbf{q} \left\langle u_{n\mathbf{q}} \mid (\partial/\partial q_x)\, u_{n\mathbf{q}} \right\rangle \tag{2.1}$$

The formula given here is for a simple cubic lattice and derived by R. Resta [17]. Currently, the modern theory of polarization is integrated with the popular computer program for performing *ab initio* quantum mechanical calculations such as VASP (the Vienna Ab initio Simulation Package).

Materials that are both ferromagnetic and ferroelectric are known as magnetoelectric multiferroics which are the most frequently studied multiferroics. The magnetoelectric multiferroics are important for two reasons. Firstly, the possibilities of using electric field (**E**) to control magnetization (**M**) or using magnetic field (**H**) to control polarization (**P**) will open the routes for developing devices with new functionalities, especially the energy efficient devices. Secondly, the coexistence of ferromagnetic and ferroelectric orders makes the possibility of realizing four-state memory and logic devices comes true.

However, the magnetoelectric multiferroics are rather rare. N. A. Hill (later known as N. A. Spaldin) has argued that the rarity of magnetoelectric multiferroics is due to the opposite requirements of d orbital electrons for ferromagnetism and ferroelectricity [18]. For ferromagnetic materials, e.g. Fe, Co and Ni, a finite number of electrons are occupied at d orbitals, while for ferroelectric materials, e.g. $BaTiO_3$, there are no electrons at d orbitals, so called d^0-ness. It should be noted that a non-zero electron occupancy of d orbitals is usually needed even for ferrimagnetism and antiferromagnetism. The stereochemically active lone pair is another mechanism for ferroelectricity, for example, the $6s^2$ lone pair on Pb^{2+} ion in $PbTiO_3$ or the $6s^2$ lone pair on Bi^{3+} ion in $BiFeO_3$. Thus, the coexistence of $6s^2$ lone pair on Bi^{3+} ion and $3d^5$ electrons on Fe^{3+} in $BiFeO_3$ makes the bismuth ferrite an ideal candidate for studying magnetoelectric multiferroics. Since the importance of the magnetoelectric multiferroics, we use multiferroics to represent the magnetoelectric multiferroics in the remains of the thesis.

Recently, N. A. Spaldin et al. have classified the multiferroics as four categories, namely two mechanisms for ferromagnetism by two mechanisms for ferroelectricity [19]. The two mechanisms for ferroelectricity are d^0 ferroelectricity and lone pair ferroelectricity. Aside from the aforementioned *d*-electron magnetism, the *f*-electron magnetism also exists such as in strained $EuTiO_3$ [20]. In this thesis, we will mainly study the $BiFeO_3$ which is a lone pair ferroelectricity and *d*-electron magnetism multiferroic material.

2.3 Misfit strain and BFO phases

2.3.1 Lattice mismatch and strain engineering

There are three types of thin film growth modes: (1) the layer-by-layer growth (van der Merwe mechanism), (2) a three-dimensional island growth (Volmer Weber mechanism), and (3) a combination of the layer-by-layer and island growth (Stranski Krastanov mechanism) [21]. In this research, we deposit a perovskite film on top of a perovskite substrate. The film and the substrate are similar materials, which will render a layer-by-layer growth.

The in-plane lattice constants of the film will first follow those of the substrate and then relax to its own value when the thickness of film exceeds a critical thickness. For thin films with a film thickness smaller than the critical thickness, the mismatch of in-plane lattice constants between film and substrate will impose a strain on the film. The misfit strain is described by the lattice mismatch,

$$\varepsilon = \frac{a_s - a_0}{a_s} \tag{2.2}$$

Here, a_0 is the lattice constant for the unstrained film, a_s is the lattice constant for the substrate. As an example, we calculated some misfit strain (TABLE 2.1) values for the BFO ($a_0 = 3.965$Å) and the substrates we often encountered in literature.

2.3.2 Epitaxial BFO thin films of different phases

Bismuth ferrite ($BiFeO_3$) is the only known room temperature multiferroic material so far, which has potential applications for low power electronics such as aforementioned MESO devices in chapter 1. Below the Curie temperature, bulk BFO is considered to have a rhombohedral *R3c* space group structure with a lattice constant of $a = 3.965$Å (pseudocubic index is used throughout this thesis unless otherwise specified). It has a spontaneous ferroelectric order along the pseudocubic [111] direction[22] with a Curie

Substrate	abbreviation	Cut	a_s (Å)	Misfit strain
$LaAlO_3$	LAO	(100)	3.789	-4.65%
$(LaAlO_3)_{0.3}$ $(Sr_2AlTaO_6)_{0.7}$	LSAT	(100)	3.868	-2.51%
$SrTiO_3$	STO	(100)	3.905	-1.54%
$DyScO_3$	DSO	(110)	3.943	-0.56%
$NdScO_3$	NSO	(110)	4.010	1.10 %
$GdScO_3$	GSO	(110)	4.014	1.22 %
$MgAl_2O_4$	MAO	(100)	4.042	1.90%

Table 2.1: Misfit strains of BFO calculated for some substrates.

temperature of $\sim$ 1103K and a G-type antiferromagnetic (AFM) order with a Néel temperature of $\sim$ 673K.

Monoclinic phases

Pulsed laser deposition (PLD) is the most efficient method to grow high-quality crystalline BFO films[22]. When BFO film is epitaxially grown on a mismatched single-crystal substrate (Table 2.1), its symmetry will be lowered from rhombohedral to monoclinic due to the in-plane biaxial strain. There are three different types of monoclinic ferroelectric phases, e.g. M_A, M_B, and M_C, as shown in Figure (2.1).

The polarization $\mathbf{P}$ will also deviate from the [111] direction accordingly: For M_A, $P_x = P_y < P_z$, for M_B, $P_x = P_y > P_z$ (pointing more horizontally), and for M_C, $P_x \neq 0, P_y = 0, P_z \neq 0$. These three low-symmetry monoclinic phases are the intermediate phases that can link the tetragonal (T), rhombohedral (R), and orthorhombic (O) phases. As only monoclinic phases exist in thin films, we often call M_A phase as the R-like phase, M_B phase as the O-like phase, and M_C phase as the T-like phase.

The R-like (M_A) phase BFO is obtained by using small and medium compressive substrates such as STO [22], LSAT, and DSO. The T-like (M_C) phase BFO can be stabilized on a large compressive substrate, such as LAO. T-like phase can coexist with the R-like phase, forming a morphotropic phase boundary [23] with an enhanced ferroelectric and piezoelectric responses. The O-like (M_B) phase BFO is grown on a tensile strain substrate [24], such as NSO.

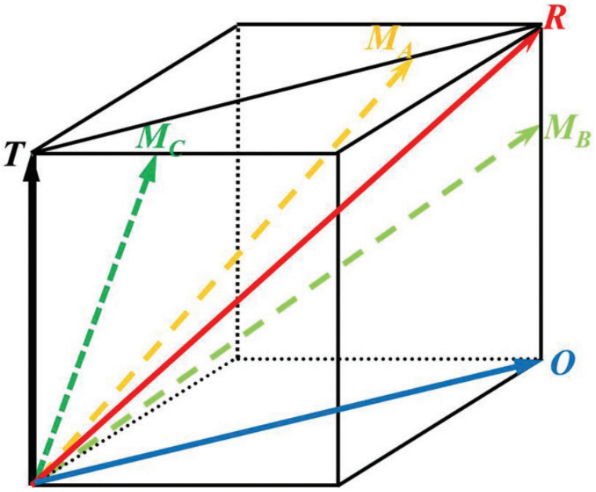

Figure 2.1: Sketch of the relation between tetragonal (T), orthorhombic (O), rhombhedral (R), and $M_\mathrm{A}, M_\mathrm{B}, M_\mathrm{C}$ phases. Arrows represent the directions of the spontaneous polarization $\mathbf{P}$. (Figure is a reproduction from: Zuhuang Chen, et al., Phys. Rev. B **88**, 054114, 2013.)

2.4 Exchange interaction and magnetic anisotropy

2.4.1 Exchange interaction

According to quantum mechanics, an electron not only has a charge e, but also has an intrinsic magnetic moment $\mu_s = -g_s \frac{e}{2m}\mathbf{S}$ arising from an intrinsic degree of freedom which is called spin (represented by operator $\hat{S}$). The magnetism is not arisen from the orbital motion of electronic charge as we had expected from classical electrodynamics, nor from the dipolar interaction of different spins which is too small to explain the room temperature spontaneous magnetization. It is explained by exchange interaction of electrons which is basically a quantum many-body (at least two-body) effect of interacting electrons. The electrons are moving in the coulomb's potential of nuclei and they are interacting with each other through coulomb's interaction too.

The electrons in quantum mechanics can be described as wave-function which is a product of orbital part and spin part $\psi_\mathrm{orb}(...ij...) \times \chi_\mathrm{spin}(...ij...)$, and the product should be antisymmetric as a whole. Then we'll get an effective hamiltonian which can be written as

$$H = -J_{ij}\mathbf{S}_i \cdot \mathbf{S}_j, \tag{2.3}$$

This interaction can explain many physics, it may happen between two electrons in the same atom which accounts for the atomic spectra, or two electrons from two adjacent atoms which explains the chemical bond. Equation (2.3) is also known as the Heisenberg model.

For magnetism, we need more electrons to be involved. Electrons on two non-neighbouring atoms can obtain this form of interaction through the interaction of electrons on another atom which is placed in between the two non-neighbouring atoms. We usually call this superexchange interaction which describes the interaction of the most magnetic materials. Unlike the dipolar interaction ($\sim K$), the exchange interaction J can be as large as $\sim 1000K$, this is the reason why we can observe the phenomenon of magnetism in our daily life. J can be positive, corresponds to spin parallel arrangement which is called ferromagnet; J can also be negative, corresponds to spin anti-parallel arrangement which is called anti-ferromagnet. If the two anti-parallel spins are not equal, for example Tb and Co in TbCo alloy, this is so called ferrimagnet.

The delocalized electrons in metals can also mediate the interaction of two magnetic ions, even these two magnetic moments have a large distance r. The interaction can also written in the form of exchange interaction (Eq. 2.3) with a r-dependent coupling given by

$$J_{\mathrm{RKKY}}(r) \propto \frac{\cos(2k_F r)}{r^3}, \tag{2.4}$$

where k_F is the fermi wave-vector. We can see from the formula that the RKKY interaction has an oscillatory dependence on the distance between the two magnetic moments. This oscillatory behaviour indicates that we can make synthetic antiferromagnet through the coupling of two magnetic layers with a non-magnetic metal layer in-between them.

2.4.2 Spin-orbit interaction

Spin-orbit interaction (Eq. 2.5) can be beautifully derived from the relativistic quantum mechanics which means spin (the intrinsic magnetic moment) is not an ad hoc assumption but an intrinsic requirement of theory of relativity.

$$H_{\mathrm{SO}} = \xi \mathbf{S} \cdot \mathbf{L} = -\frac{\hbar}{4mc^2} \sigma \cdot \mathbf{p} \times (\nabla V) = \frac{1}{2m^2c^2} \left(\frac{1}{r} \frac{\partial V}{\partial r} \right) \mathbf{S} \cdot \mathbf{L}, \tag{2.5}$$

Where V is the coulomb potential, $\mathbf{S} = \frac{\hbar}{2}\sigma$ is the spin operator, and $\mathbf{L} = \mathbf{r} \times \mathbf{p}$ is the orbital angular momentum operator. The spin-orbit interaction is proportional to $\alpha^2 Z^4$, where α is the fine structure constant and Z is the atomic number. So, large spin-orbit interactions usually exist in heavy elements such as Pt, Au, Ta, Bi, et al. For heavy elements, the screening effects due to the outer electrons must be included, thus the interaction scales as $\alpha^2 Z^2$.

Compared with the electron energy ($\sim eV$), spin-orbit interaction is very small ($\xi \sim 0.05eV$), but it is crucial for explaining the magnetic anisotropy and Dzyaloshinskii-Moriya interaction (DMI). Dzyaloshinskii-Moriya interaction (DMI) is also called the anisotropic exchange interaction. Unlike the exchange interaction, the DMI favors the orthogonal alignment of spins which is given by

$$H_{DM} = -\mathbf{D}_{ij} \cdot (\mathbf{S}_i \times \mathbf{S}_j) \tag{2.6}$$

where $\mathbf{S}_i$ and $\mathbf{S}_j$ are adjacent spins, and $\mathbf{D}_{ij}$ is the DMI vector. DMI often happens in magnetic thin film systems which lack spacial inversion symmetry and consist of materials with strong spin-orbit coupling (usually heavy metals with large Z).

2.4.3 Anisotropy energy

The magnet usually has an orientation of preferred direction, we can use this property to represent bits (one bit is the information for answering one ‘yes-no’ question). From a perspective of energy, the energy of a magnetic film can be written as

$$E_{anisotropy} = K\Omega \sin^2 \theta, \tag{2.7}$$

where K is the anisotropy energy density, Ω is the volume of the film, and θ is the angle between the magnetization ($\mathbf{M}_S$) and the normal direction ($\mathbf{n}$) of the film. If $K > 0$, the magnetization will be in the normal direction (either up $\theta = 0$ or down $\theta = \pi$), this is the perpendicular magnetic anisotropy (PMA). If $K < 0$, the minimum of energy will require $\theta = \frac{\pi}{2}$, which corresponds to the magnetization lying in the plane of the thin film, it is in-plane magnetic anisotropy (IPA) for this case. We can see from this discussion that PMA is more favorable for device fabrication, because we do not need to worry about the likelihood of the rotation of the magnetization in the plane.

The anisotropy energy has three contributions, i.e., volume anisotropy E_{volume}, surface anisotropy $E_{surface}$ and shape anisotropy E_{shape}. For magnetic thin films, there is a simple expression for the shape anisotropy $E_{shape} = -\frac{1}{2}\mu_0 M_S^2 \Omega \sin^2\theta$, where M_S is the spontaneous magnetization of the magnet. This term is negative, which means we had better 'maximize' this contribution to lower the energy ($\theta = \frac{\pi}{2}$), in other words the shape anisotropy favors IPA. The shape anisotropy energy is also called the demagnetization energy. Then, we can get an expression for anisotropy energy density

$$K = K_v + \frac{K_s}{t} - \frac{1}{2}\mu_0 M_S^2, \tag{2.8}$$

where K_v is the volume contribution (such as volume magnetocrystalline anisotropy), K_s is the surface contribution, t is the thickness of the thin film. The volume contribution K_v and the surface contribution K_s are usually very small, in most cases the shape anisotropy will dominate, result in an in-plane easy axis (IPA). However, when t is very small and $K_s > 0$, the surface contribution K_s/t dominates and K is positive. In this case the easy axis will be perpendicular to the film (PMA). Letting $K = 0$, we can get the critical thickness t_c of magnetic films for obtaining PMA

$$t_c = \frac{K_s}{\frac{1}{2}\mu_0 M_S^2 - K_v}. \tag{2.9}$$

Physical Origins of PMA

There are several routes to realize PMA, such as $L1_0$-ordered alloys (CoPt, FePt, FePd, etc.) [25], rare earth-transition metal (RE-TM) alloys (TbCo, GdCo) [26], and interface induced PMA. For the interface induced PMA, there are two types of setup, one is ferromagnetic metal in contact with heavy metal, typically Co/Pt or Co/Pd[27], another one is ferromagnetic metal (Co, Fe, CoFe, CoFeB) in contact with oxide (AlO_x, MgO, TaO_x, HfO_x).

The interface will break the spacial inversion, and the electron orbits at the interface will also hybridize. For Co/Pt interface, it is a 3d-5d hybridization (3d is from the Co, and 5d is from the Pt). For FM/Oxide interface, the metal element (Co or Fe) will form chemical bonds with oxygen from oxide, thus a 3d orbit on metal will hybridize with the p orbit on oxygen [28].

Using second order perturbation theory, we can calculate the energy splitting which is largely due to the spin-orbit interaction

$$\Delta E_{SO} = \sum_n \frac{|\langle n| H_{SO} |0\rangle|^2}{E_0 - E_n}. \tag{2.10}$$

Where n denotes the excited states and 0 refers to the ground state. The suitably arranged elements from both layers will exert a suitable ‘crystal field’ on the atoms at the interface which will not happen for the bulk system. Although the heavy atom has a strong spin-orbit interaction, while the oxygen has a weak interaction, both calculation and experiment show that they will both favor an easy axis perpendicular to the interface.

It is important to note that the Pt (111) texture is the premise for realizing PMA at the Co/Pt interface, and the Pt atom will also contribute to the magnetization which is not magnetic in bulk. For FM/oxide interface, the oxidation level at the interface plays an important role, the optimum oxidation level at the interface will render the most obvious PMA phenomenon.

2.4.4 Spin models

In this subsection, some spin models are reviewed and they are fundamental for describing the magnetic properties such as magnetization for this research.

The Hubbard model

The Hubbard model is usually used to describe a many-electron system in a crystalline structure, and it can transform into other spin models through appropriate approaches, such as the Heisenberg model and the Stoner model. The Hubbard model contains two terms, namely the hopping term (t-term) and the Coulomb repulsion term (U term):

$$H = -t \sum_{ij,\sigma} \left(c^{\dagger}_{i\sigma} c_{j\sigma} + h.c. \right) + U \sum_i n_{i\uparrow} n_{i\downarrow}, \tag{2.11}$$

where $c^{\dagger}_i$ and c_j are the creation operator on the i-th site and the annihilation operator on the j-th site, respectively. σ is the spin index which can be either up or down and n_i represents the occupation operator on the i-th site. The hopping term (t-term) in equation (2.11) is used to describe the kinetic energy of the system, and the

Coulomb repulsion term (U term) is used to describe the electron-electron repulsion when two electrons with opposite spin orientations reside at the same lattice site.

If $U/t \gg 1$, the hopping term can be treated as a perturbation. Using the second order perturbation formula [29], the Heisenberg model as expressed in equation (2.3) is obtained with

$$J_{ij} = -\frac{4t^2}{U}. \tag{2.12}$$

Hence, the Hubbard model yields an isotropic antiferromagnetic Heisenberg model in the limit of $U/t \gg 1$. If U/t is not too large, the Hubbard model describes superexchange interactions between neighboring magnetic moments, which may lead to ferromagnetic or antiferromagnetic couplings, depending on the parameters of the model.

The Stoner criterion

The Stoner model describes the itinerant electrons in ferromagnetic metals, such as Fe, Co and Ni. The U term in Hubbard model (2.11) can be expressed as

$$Un_{i\uparrow}n_{i\downarrow} = U\left\{\frac{(n_{i\uparrow}+n_{i\downarrow})^2}{4} - \frac{(n_{i\uparrow}-n_{i\downarrow})^2}{4}\right\},$$

which means that a spontaneous imbalance of $n_{i\uparrow}$ and $n_{i\downarrow}$ can lead to a decrease in Coulomb interaction. The imbalance of $n_{i\uparrow}$ and $n_{i\downarrow}$ will also increase the energy in hopping term of the Hubbard model. If the decrease in potential energy (U-term) exceeds the increase in kinetic energy (t-term), the system will have a spontaneous magnetization. This is the so-called itinerant ferromagnetism.

Suppose initially that there are equal number of up-spins and down-spins, then δn down-spin spontaneously flip, the decrease in potential energy can be expressed as $-U\delta n^2$. The increase in kinetic energy is $dE\delta n$. Considering that only electrons around Fermi surface can flip, $\delta n = \rho(E_F)dE$, where $\rho(E_F)$ is density of state at the Fermi surface. Hence the increase in kinetic energy is $dE\delta n = \rho(E_F)dE^2 = \frac{\delta n^2}{\rho(E_F)}$. The spontaneous magnetization happens when the total change in energy is negative. Finally, we get the well-known Stoner criterion for itinerant ferromagnetism.

$$U\rho(E_F) > 1 \tag{2.13}$$

Only a few natural materials satisfy the Stoner criterion, such as Fe, Co and Ni, the partially filled $3d$ orbital electrons of Fe, Co and Ni are responsible for the criterion.

Spin-wave theory

Using the spin-wave theory, we can calculate the ground state and low-energy properties of Heisenberg model analytically. Suppose $J_{ij} = J > 0$, the ferromagnetic case, we first expand the Hamiltonian (2.3) as

$$H = -J \sum_{l,\delta} \frac{S_l^+ S_{l+\delta}^- + S_l^- S_{l+\delta}^+}{2} + S_l^z S_{l+\delta}^z, \tag{2.14}$$

where $l + \delta$ represents the nearest lattice site of the l-th site. Since $J > 0$, the spins on different lattice sites tend to align each other along the same direction, say the positive $\hat{z}$ direction. Excitations of this ferromagnetic spin system correspond to the departure from the positive $\hat{z}$ direction. Suppose S is the quantum spin number, $m\hbar$ is the eigen-value for operator $\hat{S}^z$, we define the departure of S^z component from the maximum value $S\hbar$ as

$$n = S - m, m = 0, \pm 1, ..., \pm S,$$

where n can be interpreted as number of the magnetic excitations (also known as magnons). The Holstein-Primakoff transformation is introduced to describe the magnetic excitations:

$$\begin{aligned} S^+ &= \hbar\sqrt{2S - a^\dagger a}a \\ S^- &= \hbar a^\dagger \sqrt{2S - a^\dagger a} \\ S_z &= \hbar\left(S - a^\dagger a\right), \end{aligned} \tag{2.15}$$

where $a^\dagger$, a are the boson creation and annihilation operators, respectively, $a^\dagger a = \hat{n}$ is the number operator, n is the eigen-value for $\hat{n}$. Consider the low-energy excitation $n \ll 2S$ and after a Fourier transformation, the isotropic Heisenberg model (2.14) can be diagonalized as

$$H = E_0 + \sum_k \hbar\omega_k a_k^\dagger a_k$$

with the dispersion

$$\hbar\omega_k = 2ZJS(1-\gamma_k), \tag{2.16}$$

where Z is the coordination number of each lattice site, and

$$\gamma_k = \frac{1}{Z}\sum_{\delta} e^{i\mathbf{k}\cdot\delta} \tag{2.17}$$

is the structural factor.

Under the long-wave extreme ($k \to 0$), we have

$$\hbar\omega_k \approx JS\sum_{\delta}(\mathbf{k}\cdot\delta)^2 \tag{2.18}$$

For sc, bcc and fcc lattices, we arrived at an identical formula from equation (2.18),

$$\hbar\omega_k = 2JSa^2k^2 = D_{sw}k^2, \tag{2.19}$$

where a is the lattice constant of the unit cell, and $D_{sw} = 2JSa^2$ is defined as the spin-wave stiffness.

Bloch $T^{3/2}$ law

The linear spin-wave theory can be used to describe low-temperature behaviours such as magnetization and heat capacity. The magnetization $M(T)$ can be expressed as

$$M(T) = g\mu_B \sum_{l}\left(S - \bar{n}_l(T)\right). \tag{2.20}$$

The lattice summations in formula (2.20) can be calculated in reciprocal space, e.g. k-space. Using the Bose-Einstein statistics, magnon number in k-space can be expressed as

$$\bar{n}_k(T) = \frac{1}{e^{\hbar\omega_k/kT}-1}, \tag{2.21}$$

we have

$$M(T) = M(0)\left(1 - \frac{\eta}{QS}\left(\frac{k_BT}{2SJ}\right)^{3/2}\right), \tag{2.22}$$

where $\eta = 0.0587$ for the 3D case [30], $Q = 1, 2, 4$ is number of spins per unit cell for sc, bcc, and fcc lattices, respectively. From equation (2.22), we arrive at the well-known Bloch $T^{3/2}$ law

$$\frac{M(0) - M(T)}{M(0)} = \frac{\eta}{QS} \left(\frac{k_B T}{2SJ} \right)^{3/2} \propto T^{3/2} \tag{2.23}$$

Bloch $T^{3/2}$ law is usually used for fitting the field-cooled magnetization data $M(T)$ to determine the exchange stiffness $A_{ex} = \frac{QJS^2}{a}$. Using A_{ex}, equation (2.22) can be rewritten as

$$\frac{M(T)}{M(0)} = 1 - \eta\sqrt{QS} \left(\frac{k_B T}{2A_{ex}a} \right)^{3/2}, \tag{2.24}$$

where $S = \frac{M(0)a^3}{Qg\mu_B}$ is the spin quantum number. Parameter $\eta = 0.0587$ in formula (2.24) comes in from the summation of magnon excitation numbers $\bar{n}_k(T)$. For isotropic Heisenberg model (formula 2.14), a gapless dispersion $\hbar\omega_k = D_{sw}k^2$ at the long-wave limit exists, leading to a finite integration $\int dk\bar{n}_k(T)$ in 3D. While 2D (or 1D) integration $\int dk\bar{n}_k(T)$ with a gapless dispersion diverges, this divergence is consistent with the disappearance of ferromagnetic order at finite temperature in low dimensional (2D or 1D) isotropic Heisenberg model.

To rescue the ferromagnetic order in 2D, one way is to include the anisotropies in isotropic Heisenberg model. For example, including the two-ion anisotropy term $-K_{ij}S_i^z \cdot S_j^z$ renders an anisotropic Heisenberg model

$$H = -\sum_{i<j} J_{ij}\mathbf{S}_i \cdot \mathbf{S}_j - \sum_{i<j} K_{ij}S_i^z \cdot S_j^z, \tag{2.25}$$

which has a gapped dispersion $\hbar\omega(k) = \hbar\omega_0 + D_{sw}k^2$, where $\hbar\omega_0 = 2ZQKS$ is the gap for spin-wave dispersion [31], $K_{ij} = K$, and Z is the coordination number for each spin on the lattice site.

Thus, the 2D Bloch law is derived by calculating $\int dk\bar{n}_k(T)$ in 2D which yields

$$\Delta M_{2D} = \frac{M(0)k_B T}{4\pi g A_{ex}(0)t} \ln\left[\frac{k_B T}{\hbar\omega_0}\right], \tag{2.26}$$

where t is the thickness of ferromagnetic layer.

2.5 Summary

In this chapter, the physical background of ferroelectricity and ferromagnetism are briefly introduced with special emphasis that both phenomena can only be understood in the context of quantum mechanics. Concepts of of multiferroics, strain-engineering, phase evolution in BFO and PMA which are important for this project are also explained. Lastly, the spin model and the spin wave theory are outlined concisely, which are useful for us to understand the anisotropy and dimensional effect of the ferromagnetism.

CHAPTER 3

Experimental methods

3.1 Introduction

This chapter describes the methods and equipment used to fabricate and characterize the samples studied in this project. BFO films are deposited by Pulsed Laser Deposition (PLD), the Pt/Co magnetic multilayers are sputtered by DC magnetron sputtering. Film thickness is determined by X-ray reflectivity (XRR) and double-checked by Transmission Electron Microscopy (TEM). X-ray diffraction (XRD) is used to determine crystalline quality of the sample, X-ray reciprocal space mapping (RSM) is used to determine the lattice parameters of the sample.

Atomic force microscopy (AFM) is used to study the surface morphology of the thin film, Piezoelectric force microscopy (PFM) is used to probe the electromechanical response of the BFO. The atomic lattice configurations of the thin film can be directly imaged by Transmission Electron Microscopy (TEM). X-ray Absorption Spectroscopy (XAS) is used to determine the element (such as Co) valence state.

The magnetic properties of the Co/Pt multilayers on BFO are examined through the anomalous Hall effect (AHE) magnetometry and superconducting quantum interference device vibrating sample magnetometry (SQUID-VSM).

3.2 Sample Fabrication

3.2.1 Pulsed Laser Deposition

The Pulsed Laser Deposition (PLD) system [32] is used for depositing oxide thin films. There is a high vacuum chamber in the system to hold the multiple targets and substrates. During the film growth, a target with the same stoichiometry as the material that we wish to grow is been used. When the target is bombarded by the high-power pulsed laser, the material is vaporized from the target and travel directly to the heated substrate where the material condenses (FIG. 3.1).

The key parameters that affect the quality of PLD growth include: substrate temperature, oxygen partial pressure and laser fluence. In this project, a stoichiometric $BiFeO_3$ target was used for the laser ablation and we mainly grew $BiFeO_3$ thin films on $Ca_{0.96}Ce_{0.04}MnO_3$ (CCMO) buffered $LaAlO_3$ (LAO) (001) substrates. The growth condition is summarized in Table (3.1).

After the ablation, each sample was cooled down to room temperature (RT) at $20°C$/min under an oxygen pressure of $\sim$ 1000 Pa.

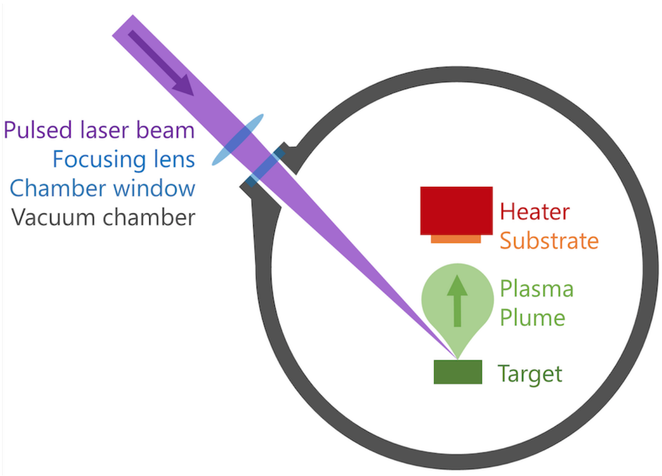

Figure 3.1: Diagram of pulsed laser deposition (Figure is a reproduction from Wikimedia Commons, the free media repository).

Material	Growth Temperature	Oxygen partial pressure	Laser fluence	Repetition rate
CCMO	670 °C	13 Pa	1.0 J/cm^2	5 Hz
BFO	690 °C	13 Pa	1.2 J/cm^2	10 Hz

Table 3.1: Growth condition for BFO on CCMO buffered LAO substrate.

3.2.2 DC Magnetron Sputtering

After deposition of BFO films, a DC magnetron sputtering system (FIG. 3.2) will be used to deposit magnetic layers. Several targets and samples are contained in a high vacuum chamber. Once the pressure in the chamber is low enough ($\sim 5 \times 10^{-8}$ Torr), argon gas with a partial pressure will be introduced into the chamber. Argon gas is ionized and form a plasma by applying an electric field between the target and shield. Driving by the electric field, Argon ions strike the target and knock out more particles including the electrons and neutral atoms, magnetrons under the target use the electric and magnetic fields to confine the electrons close to the surface of the target.

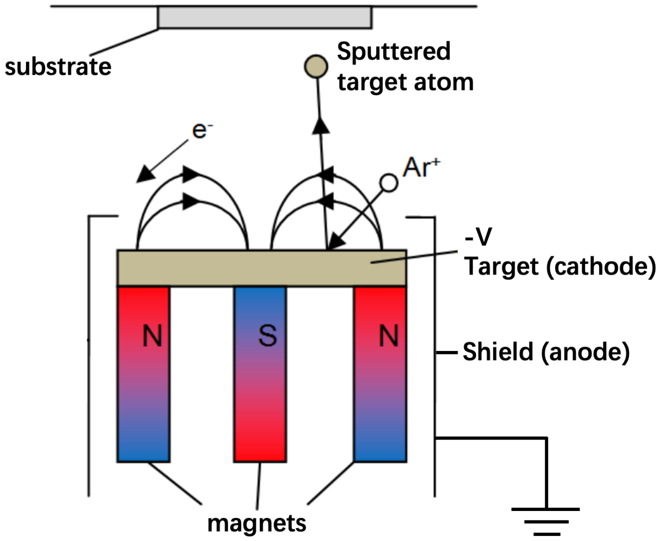

Figure 3.2: Schematic of magnetron sputtering.

More argon atoms will be ionized by electrons (Eq. 3.1), and hence, more neutral atoms will be sputtered from the target which then impinge upon the sample and a thin film of the target material builds up.

$$e^- + Ar \rightarrow Ar^+ + 2e^- \tag{3.1}$$

Insulators such as MO_x should be deposited by using a radio-frequency alternating electric field to avoid the charge accumulation, so called RF magnetron sputtering.

3.3 Structures and Characterizations

3.3.1 X-ray diffraction (XRD)

Atoms aggregated together to form crystalline solids with three dimensional periodic structure through interactions, e.g. covalent bonds, ionic bonds, metallic bonds and Van Der Waals bonds. Series of lattice planes with identical plane normals are denoted by Miller indices (hkl). When a monochromatic X-ray strikes a lattice plane, scattered beams from parallel lattice planes will undergo constructive and destructive interference. The constructive diffraction can be described by Bragg's Law

$$2d_{hkl}\sin\theta = n\lambda, \tag{3.2}$$

where d_{hkl} is the inter-planar spacing, λ is the X-ray wavelength, θ is the incidence angle and n is the order of reflection.

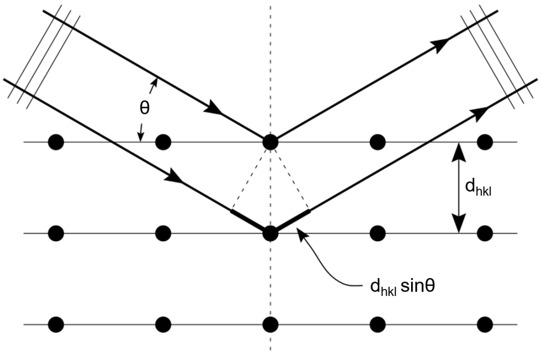

Figure 3.3: Schematic illustration of Bragg's Law (Figure is a reproduction from Wikimedia Commons, the free media repository).

The structure of crystalline solids can be classified as 14 basic crystal structures, e.g. cubic, body center cubic (bcc), face center cubic (fcc), tetragonal, orthorhombic, rhombohedral, monoclinic and triclinic. Here, we use a, b, and c to represent the dimensions of the unit cells, α, β and γ denote the corresponding angles in the unit cells.

For cubic crystal systems, $a = b = c$ and $\alpha = \beta = \gamma = 90°$, we have

$$\frac{1}{d_{hkl}^2} = \frac{h^2 + k^2 + l^2}{a^2}. \tag{3.3}$$

For tetragonal crystal systems, $a = b \neq c$ and $\alpha = \beta = \gamma = 90°$, we have

$$\frac{1}{d_{hkl}^2} = \frac{h^2 + k^2}{a^2} + \frac{l^2}{c^2}. \tag{3.4}$$

For orthorhombic systems, $a \neq b \neq c$ and $\alpha = \beta = \gamma = 90°$, we have

$$\frac{1}{d_{hkl}^2} = \frac{h^2}{a^2} + \frac{k^2}{b^2} + \frac{l^2}{c^2}. \tag{3.5}$$

For monoclinic systems, $a \neq b \neq c$, $\alpha = \gamma = 90°, \beta \neq 90°$, we have

$$\frac{1}{d_{hkl}^2} = \frac{1}{\sin^2\beta}\left(\frac{h^2}{a^2} + \frac{k^2\sin^2\beta}{b^2} + \frac{l^2}{c^2} - \frac{2hl\cos\beta}{ac}\right). \tag{3.6}$$

For triclinic systems, $a \neq b \neq c$, $\alpha \neq \beta \neq \gamma$

$$\frac{1}{d_{hkl}^2} = \frac{1}{V^2}\left(S_{11}h^2 + S_{22}k^2 + S_{33}l^2 + 2S_{12}hk + 2S_{23}kl + 2S_{13}hl\right) \tag{3.7}$$

where $S_{11} = b^2c^2\sin^2\alpha$, $S_{22} = a^2c^2\sin^2\beta, S_{33} = a^2b^2\sin^2\gamma$, $S_{12} = abc^2(\cos\alpha\cos\beta - \cos\gamma)$, $S_{23} = a^2bc(\cos\beta\cos\gamma - \cos\alpha)$ and $S_{13} = ab^2c(\cos\gamma\cos\alpha - \cos\beta)$.

$\theta - 2\theta$ scan

X-ray diffraction of lattice planes that are parallel with the sample surface $(00l)$ is usually employed for checking the crystalline quality, secondary phases and impurities, also for determining the c-lattice constant, so called $\theta - 2\theta$ scan (or $2\theta/\omega$ scan). Before the $\theta - 2\theta$ scan, we usually choose (002) peak of the substrate as the reference for alignment.

In a conventional $\theta - 2\theta$ measurement, the measured lattice planes are parallel to the sample surface. The angles of the incident and the scattered beams have the same angle (θ) as shown in Figure 3.4 (a), so called symmetrical reflection measurement.

Grazing Incidence X-ray Diffraction (GIXRD)

If the incident angle α of the X-ray beam is fixed to a very small value (0.5 - 3°) and only the detector is scanned to measure inclined lattice planes is known as asymmetrical reflection measurement (Figure 3.4, b). The asymmetrical reflection measurement with small incident angle is usually called the grazing incidence X-ray diffraction (GIXRD).

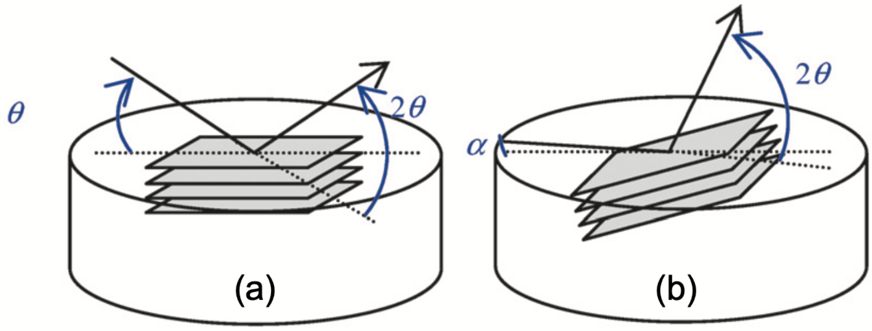

Figure 3.4: (a) Symmetrical-reflection measurement and (b) asymmetrical-reflection measurement for out-of-plane XRD. (Figure is a reproduction from: Toru Mitsunaga, The Rigaku Journal, **25** (1), 2009.)

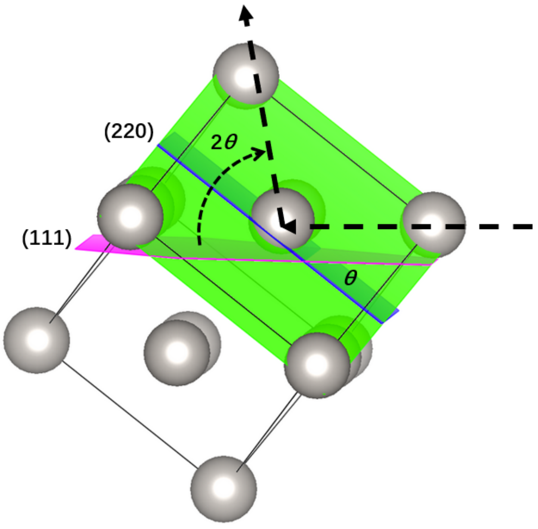

Figure 3.5: Schematic of fcc Pt structure with (111) plane (purple) running parallel with the film surface where the grey balls represent the Pt atoms. The incidence X-ray (dashed black line) comes from right to the left and is scattered by the (220) plane (blue). The green plane represents the (200) plane. This figure is generated using VESTA (Visualization for Electronic and Structural Analysis) software.

GIXRD is suitable for studying a polycrystalline thin film with random or weak preferred orientation. In this project, we use GIXRD to check the existence of Pt (111) texture in the top sputtered Co/Pt multilayers on BFO. The fcc Pt structure is illustrated in Figure (3.5), where the (111) planes (purple) are parallel to the film surface. The inclined (220) planes (blue) intersect with the horizontal (111) planes, resulting in an intersection angle of $\sim 35^\circ$. This angle is in proximity to the constructive diffraction condition for (220) planes, i.e. $2\theta \sim 67.5^\circ$. Hence, Pt (111) grains in a polycrystalline thin film will lead to the appearance of a (220) peak in GIXRD.

X-ray Reciprocal Space Mapping (RSM)

If we align the sample with specific series of lattice planes other than $(00l)$ planes [33], for example (103) planes, scanning in ω and 2θ will render us information on in-plane and out-of-plane lattice constants, this is so-called reciprocal space mapping (RSM). RSM (103) or RSM $(\bar{1}03)$ is often employed to determine the in-plane a lattice constant and out-of-plane c lattice constant for pseudo-cubic lattice cells. The RSM (103) data is often represented in 2D q_z vs q_x plots and the strong diffraction peak caused by the substrate in RSM is usually used as the absolute value for calibration.

3.3.2 X-Ray Reflectivity (XRR)

Since X-ray can penetrate into material with penetration length $\propto \sin(\theta/\mu)$, where μ is the material permeability. Thicknesses of thin films can be determined from the constructive and destructive interferences between grazing incident X-ray beams scattered by top film surface and bottom film/substrate interface by using the Bragg's Law

$$2d \sin\theta = n\lambda, \tag{3.8}$$

where d is the thickness of thin film, λ is the wave length of X-ray and n is the order of reflection. In this research, we use Cu $K_{\alpha 1}$ radiation with $\lambda = 1.5406$Å. If the sample film has very flat surface and very small interface roughness, thickness of ~ 100 nm can be estimated from discriminating peak positions of different orders in 2θ scan. The oscillation in 2θ scan caused by different orders of diffraction peaks are also called Kiessig fringes. Thickness of thin film d can be estimated from the separation of peaks $\theta_{m+1} - \theta_m$ as

$$d \approx \frac{\lambda}{2} \times \frac{1}{\theta_{m+1} - \theta_m}. \tag{3.9}$$

In addition, there would be 100% reflection for incidence angles less than the critical angle θ_c [34] which varies depending upon the electronic density ρ of the material as $\theta_c \propto \sqrt{\rho}$.

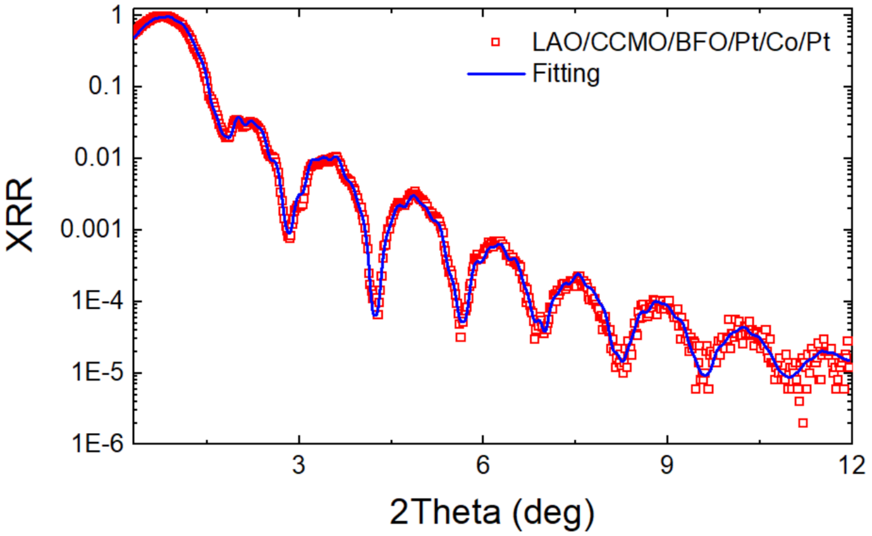

Figure 3.6: Log intensity plot of the XRR for Pt/Co/Pt sputtered on $BiFeO_3$ (BFO) thin film on $Ca_{0.96}Ce_{0.04}MnO_3$ (CCMO) buffered $LaAlO_3$ (LAO) substrates (open red squares), the fitted structure via GenX (blue curve) is Pt(4.5)/Co(0.7)/Pt(1.2)/BFO(20.0)/CCMO(15.9)/LAO (numbers in parentheses are nominal thicknesses in nanometer throughout the thesis, unless stated otherwise).

To determine the thickness of thin film, a XRR simulation based on GenX software [35] is usually used which is specially useful for fitting film with multilayer structure. As long as the clear oscillations were obtained through the low-angle XRR scan, thicknesses of different layers can always be fitted with high accuracies. In Figure (3.6), a curve fitting for Pt/Co/Pt trilayer structure is presented with the fitting parameters listed in Table (3.2), where d represents the thickness of each layer and σ represents the roughness of each layer.

Parameter	Value
σ_{LAO}	2.6 ± 0.6 Å
d_{CCMO}	159 ± 2 Å
σ_{CCMO}	2.8 ± 0.3 Å
d_{BFO}	200 ± 2 Å
σ_{BFO}	2 ± 1 Å
d_{seedPt}	12 ± 2 Å
σ_{seedPt}	3 ± 2 Å
d_{Co}	7.2 ± 0.2 Å
σ_{Co}	5 ± 1 Å
d_{topPt}	45.2 ± 0.1 Å
σ_{topPt}	2.1 ± 0.1 Å

Table 3.2: GenX fitting for Pt/Co/Pt on BFO sample in Figure (3.6), where d represents the thickness of each layer and σ represents the roughness of each layer.

3.3.3 Atomic Force Microscopy (AFM)

Atomic force microscopy (AFM) is a very sensitive type of scanning probe microscopy which can track the topography of the sample surface by using a tip mounted on a cantilever. The deflection of the cantilever is related with the tip-sample distance and it is magnified by the laser point deviated from the relaxed position (FIG. 3.7 a) and registered as a non-zero voltage: negative for bending toward the sample and positive for bending away. There are several modes for AFM, e.g. contact mode, AC mode (tapping mode) and PFM mode. In AC mode, the tip is not scanned across the sample surface in constant contact. Instead, the cantilever vibrated near its resonance frequency causing the tip to oscillate up and down while the tip scanning the sample surface which means the tip only comes into close contact with the sample surface intermittently, thus save the lifetime of the probe tip.

Piezoresponse force microscopy (PFM) is a variant of atomic force microscopy (AFM) that allows imaging and manipulation of piezoelectric/ferroelectric domains by using the converse piezoelectric effect (CPE). It can discriminate domain structures from several nanometers to 100 μm. In PFM mode, the sample is grounded and a conductive AFM tip is used to apply the electric field onto the sample. The tip we

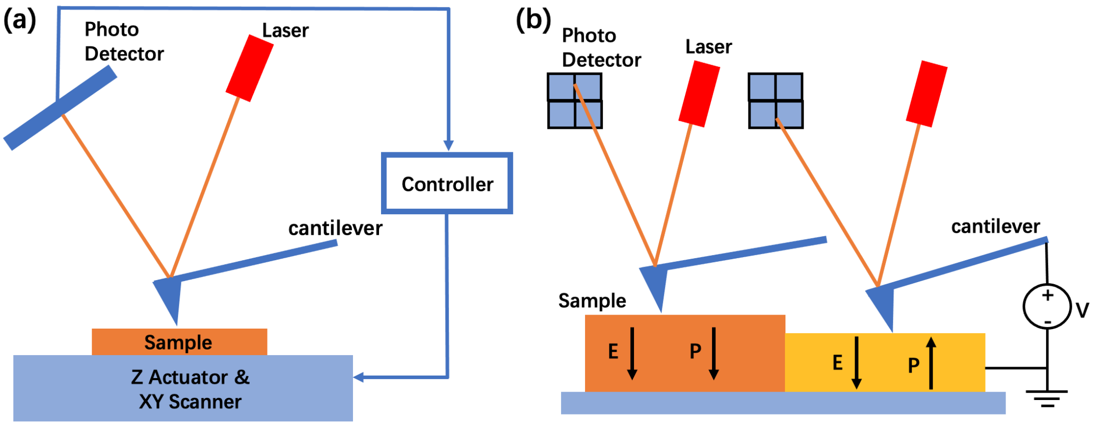

Figure 3.7: (a) Schematic of AFM. (b) Schematic of PFM: the sample expands when the polarization of the domain is parallel to the applied electric field.

used in PFM is a sharp conductive probe which is manufactured by coating a conductive material such as platinum, gold, tungsten and even conductive diamond to a silicon probe. Due to the CPE, the sample locally expands or contracts according to the different direction of the polarization of the FE domain as shown in Figure 3.7 (b). The force between the tip and the sample surface can be measured by the movement of cantilever, thus mapping out the FE domain structures.

In this project, we use Asylum Research MFP-3D atomic force microscope (AFM) to image the surface topography and the vertical PFM.

3.4 Magnetometry

Anomalous Hall effect (AHE) magnetometry and superconducting quantum interference vibrating sample magnometer (SQUID-VSM) are the most often used techniques for characterizing magnetic properties of the thin film samples.

3.4.1 Anomalous Hall effect (AHE) Magnetometry

Anomalous Hall Effect (AHE) magnetometry is a useful tool for measuring the hysteresis loops for magnetic metal systems. In a Hall effect measurement, there are three terms in the Hall voltage (V_H) [36, 37],

$$V_H = \left(\frac{R_0 I}{t}\right) B\cos\alpha + \left(\frac{\mu_0 R_s I}{t}\right) M\cos\theta + \left(\frac{kI}{t}\right) M^2 \sin^2\theta \sin 2\phi \qquad (3.10)$$

where t is the film thickness, R_0 is the ordinary Hall coefficient, R_s is the AHE coefficient, and the angles α, θ, and ϕ are defined in Figure (3.8). α is the angle between the applied magnetic field and the normal to the sample, θ is the angle between the magnetization and the normal (Z axis), and ϕ is the angle between the current direction (X axis) and in plane component of the magnetization.

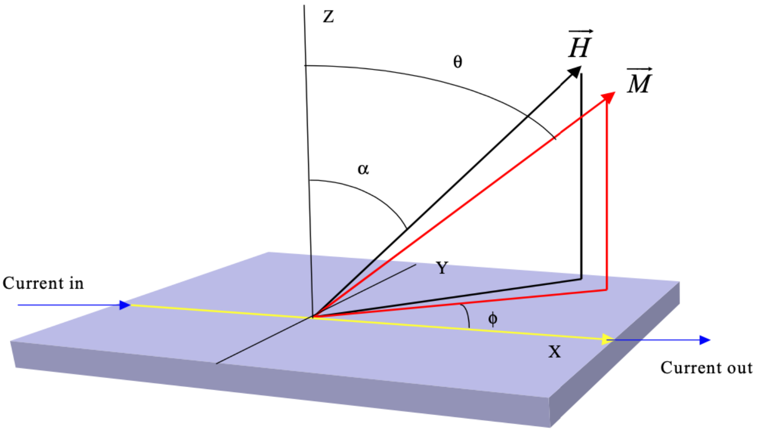

Figure 3.8: Geometry of the AHE measurement. (Figure is a reproduction from: J. R. Lindemuth et al., Anomalous Hall Effect Magnetometry, Lake Shore Cryotronics, Inc.)

The first term in Eq. (3.10) is the ordinary Hall effect (OHE) which arises from the Lorentz force acting upon the conduction elections. The OHE depends on the z-component of the $\vec{B}$ field (B_z) and produces a voltage perpendicular to B_z and the current I. The second term is the anomalous Hall effect (AHE) which arises from the spin dependent scattering mechanisms [38]. The AHE term depends on the perpendicular component of the magnetization $\vec{M}$, and results a voltage perpendicular to M_z and I. The third term is so called planar Hall effect (PHE), or anisotropic magnetoresistance (which is different from angular magnetoresistance). The PHE is a second order effect of magnetization $\vec{M}$ which is proportional to the square of the planar component of $\vec{M}$ ($M\sin\theta$).

It is important to note that all these three terms are inversely proportional to the film thickness t, this makes AHE magnetometry an important tool for measuring ultra-thin metal magnetic films.

In this project, the AHE magnetometry is often used to measure the magnetic films with PMA. For PMA measurement, the $\vec{B}$ field is perpendicular to the thin film, which implies that $\alpha = 0$, suppose the magnetization $\vec{M}$ is also perpendicular to the thin film, $\theta = 0$, which yields,

$$V_H = \left(\frac{R_0 I}{t}\right) B + \left(\frac{\mu_0 R_s I}{t}\right) M \tag{3.11}$$

The Hall resistance is defined as:

$$R_H = \frac{V_H}{I} = \left(\frac{R_0}{t}\right) B + \left(\frac{\mu_0 R_s}{t}\right) M \tag{3.12}$$

It is evident that, the variation of magnetization with changing magnetic filed B can be extracted from Eq. (3.12) by subtracting the B linear contribution. While in real measurement, the B linear contribution to resistance is often negligible when compared with the M linear contribution. Thus the shape of the $R_H - B$ loop resembles the $M - H$ hysteresis loop.

In this project, we use the Quantum Design Physical Property Measurement System (PPMS) to perform the AHE measurements.

3.4.2 SQUID-VSM

The principle of SQUID-VSM is based on the Faraday's law which states that the emf is given by the rate of change of the magnetic flux $\mathcal{E} = -\frac{d\Phi}{dt}$. A magnetic sample oscillates at a known frequency inside the pick-up coils. The moving magnetic moment will induce an alternating current (AC) signal into the coils which are inductively coupled to a superconducting quantum interference device (SQUID). Then, a measurable voltage is induced by the SQUID. The MPMS 3 Quantum Design SQUID-VSM was used to measure the $M - H$ hysteresis loos and $M - T$ curves of the thin film samples in this project.

The SQUID-VSM measures the magnetic moment of thin film as well as the substrate induced by the applied magnetic field. The field can be applied either parallel to the sample surface or perpendicular to the sample surface in this project. After the measurement, the linear diamagnetic contribution (depends on the substrate) should be deducted from the measured $M - H$ hysteresis loop to get the moment of the thin

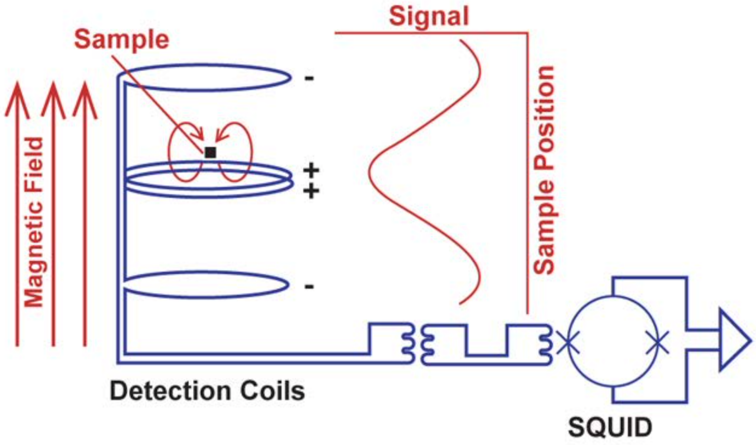

Figure 3.9: SQUID detection schematic. (Figure is a reproduction from: MPMS 3 User's Manual)

film. This clumsy looking procedure is compensated by the high accuracy of the measurement. The typical error of the SQUID-VSM measurement by Quantum Design's MPMS 3 is $\sim 1.5 \times 10^{-8}$ emu [39]. Supposing that the measured film has the dimension of 5 mm × 3 mm × 1 nm, the error of magnetization is estimated to be ~ 1 emu/cm^3 which is less than 0.1% of the Co magnetization.

In this research, we will combine the advantages of both methods, the SQUID-VSM method is used to measure the $M - H$ curves (for both in-plane and out-of-plane geometries) and the $M - T$ curves, the AHE method is used to measure the $R - H$ curves and the anisotropy fields.

3.5 Summary

Methods of preparation, characterisation and measurement of Co/Pt multilayers on BFO thin films have been discussed in this chapter. Only methods operated in person are described. BFO thin films were deposited by pulsed laser deposition (PLD) and the Co/Pt multilayers were sputtered by DC magnetron sputtering. Surface topography of the thin film was recorded by using the AFM. Structural and thickness of the thin films were examined by XRD $\theta - 2\theta$ scan, RSM and XRR. Magnetic properties of the FM/BFO heterostructures were examined by AHE magnetometry and SQUID-VSM.

Chapter 4

Pt/Co/Pt trilayers on epitaxial $BiFeO_3$ thin films

4.1 Introduction

The basic structure we will study in this chapter is Pt/Co/Pt/BFO/CCMO/LAO, where BFO represents $BiFeO_3$, CCMO represents $Ca_{0.96}Ce_{0.04}MnO_3$ and LAO represents $LaAlO_3$.

To investigate the interplay of bismuth ferrite (BFO) and Pt/Co/Pt trilayers with perpendicular magnetic anisotropy (PMA), we need to reduce the thickness of Pt seed layer as much as possible. Pt/Co/Pt trilayer is a classic structure that exhibits PMA which usually consists of a large thickness of Pt seed layer (2-3 nm) to ensure the formation of Pt (111) crystallographic texture on a silicon substrate which hosts the Pt/Co interfacial PMA. Pt, with its face-centered-cubic (fcc) structure, is expected to have the lowest surface energy with crystals oriented in the close packed {111} planes. However, the absence of a cube-on-cube epitaxial relationship between Pt (111) and BFO (001) raises doubts about achieving Pt growth with (111) texture on BFO (001) thin films. In a recent study, PMA was achieved in Pt/Co/AlO_x trilayers sputtered onto a TiO_2 terminated $SrTiO_3$ (001) substrate using just a 1 nm Pt seed layer[40], suggesting the possibility of realizing Pt (111) texture in ultra-thin Pt seed layer on (001)-oriented perovskite films.

In this chapter, we will present results of magnetic properties of Pt/Co/Pt trilayers with varius thicknesses of Pt seed layers on BFO films on $Ca_{0.96}Ce_{0.04}MnO_3$ (CCMO) buffered $LaAlO_3$ (001) substrates. The magnetic hysteresis loops are studied using both a Vibrating Sample Magnetometer (VSM) and an AHE magnetometer. The magnetic anisotropy field (H_A) is measured using a method based on the anomalous Hall effect (AHE). The effect of different surface treatments of BFO on the magnetic anisotropy of Pt/Co/Pt is also studied.

4.2 Samples and Characterizations

4.2.1 Epitaxial growth of $BiFeO_3$ films on $Ca_{0.96}Ce_{0.04}MnO_3/LaAlO_3$

To achieve the best PMA for Pt/Co/Pt trilayer and make the results more comparable, we need to fabricate BFO samples with similar surface topographies and very small roughness. Bismuth ferrite (BFO) thin film grown on a large compressive strain ($< -4.3\%$) substrate such as $LaAlO_3$ (LAO) usually has a step-terrace morphology with a very flat surface which is ideal for subsequent sputtering of metal layers. Unlike the rhombohedral (R-) like phase BFO grown on moderate compressive strained substrates such as $SrTiO_3$ (STO) and $DyScO_3$ (DSO), the thin BFO film grown on LAO is a tetragonal (T-) like phase.

In this study, we choose to fabricate thin BFO films with various thicknesses (16-80 nm) on 16-nm CCMO buffered $LaAlO_3$ (001) substrates by pulsed laser deposition (PLD), using conditions listed in Table (3.1) in Chapter 3. CCMO (a = 3.770 Å) has a little smaller lattice constant than that of LAO (a = 3.789 Å). Inserting a layer of CCMO between LAO and BFO will not change the large compressive strain that imposes on BFO, actually a T-like BFO phase stabilizes on CCMO buffered LAO [41] substrates more easily and stably than directly on LAO. What is more, the CCMO layer serves as the back electrode for piezoresponse force microscopy (PFM) measurement in this project.

X-ray diffraction and structural characterization

X-ray diffraction (XRD) measurements, including high-angle $\theta - 2\theta$ scan, low-angle X-ray reflectometry (XRR) and reciprocal space mapping (RSM) were carried out to determine the thickness, crystal structure and lattice parameters of the thin film by using a SmartLab X-ray Diffractometer with Cu $K_{\alpha 1}$ radiation (λ = 1.5406 Å). HAADF-STEM and EDS were conducted using a double-aberration-corrected transmission electron microscopy (Thermo Fisher Themis Z G2 60-300) operated at 300 kV to analyze the thickness and crystal structure of the thin films.

Figure 4.1 (a) displays a typical $\theta - 2\theta$ X-ray diffraction (XRD) logarithm plot of the six BFO samples with various thicknesses, e.g. 17 nm, 23 nm, 38 nm, 43 nm, 54 nm and 77 nm, on a 16-nm CCMO buffered LAO substrates. Aside from the T-BFO (001), T-BFO (002), CCMO (001), CCMO (002), LAO (001) and LAO (002) peaks, there are no other impurity peaks. The c-axis lattice constants are derived from the XRD plot and presented with the change of the film thicknesses in Figure 4.1 (b).

The thicknesses of the films can be determined by fitting the X-ray reflectometry (XRR) data through using the GenX software[35], and cross-checked by transmission electron microscopy (TEM) (Figure 4.2).

The typical fitting curves for a thin BFO film and a thick BFO film are presented at Figure (4.3). The structural parameters extracted from the curve fittings are presented in Table (4.1). Due to the rapid increase in the surface roughness of thicker BFO films,

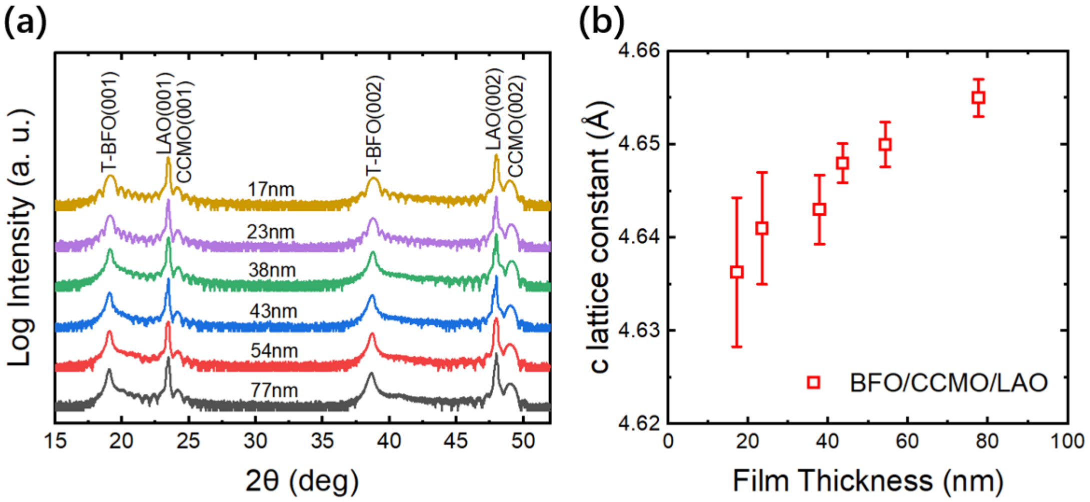

Figure 4.1: (a) X-ray θ-2θ scans of the BFO films of various thicknesses grown on CCMO buffered LAO substrates. (b) Thickness dependence of the c-axis lattice constants of the T-like phase BFO on CCMO buffered LAO substrates.

the oscillation in XRR disappears, making the fitting impossible. The thickest film with a successful fitting in this research is a 77-nm BFO sample.

Sample	σ_{LAO} (Å)	d_{CCMO} (Å)	σ_{CCMO} (Å)	d_{BFO} (Å)	σ_{BFO} (Å)
Figure 4.2 (a)	0.1 ± 0.1	178 ± 3	1 ± 1	233 ± 1	0.1 ± 0.1
Figure 4.3 (a)	0.1 ± 0.1	166 ± 1	1.5 ± 0.8	176 ± 1	2 ± 1
Figure 4.3 (b)	0.1 ± 0.1	156 ± 2	0.1 ± 0.1	543 ± 3	4.4 ± 0.3

Table 4.1: Results of fitting XRR data of BFO samples in Figure 4.2 (a), Figure 4.3 (a) and (b), where d represents the thickness of each layer and σ represents the roughness of each layer.

The $(\bar{1}03)$ RSMs and AFM images for all six samples shown in Figure (4.1) are presented in Figure (4.4). The most remarkable peaks aside from the LAO peak and the CCMO peak are located at the lower part of the $(\bar{1}03)$ RSMs (FIG. 4.4 a - f). It is clear from the RSMs that the $(\bar{1}03)$ reflection splits into a triplet structure as a consequence of the existence of four monoclinic domains. This is the signature of monoclinic M_{C} phase [42].

In M_{C}-type monoclinic distortion (FIG. 4.5 a), the simple tetragonal unit cell skews

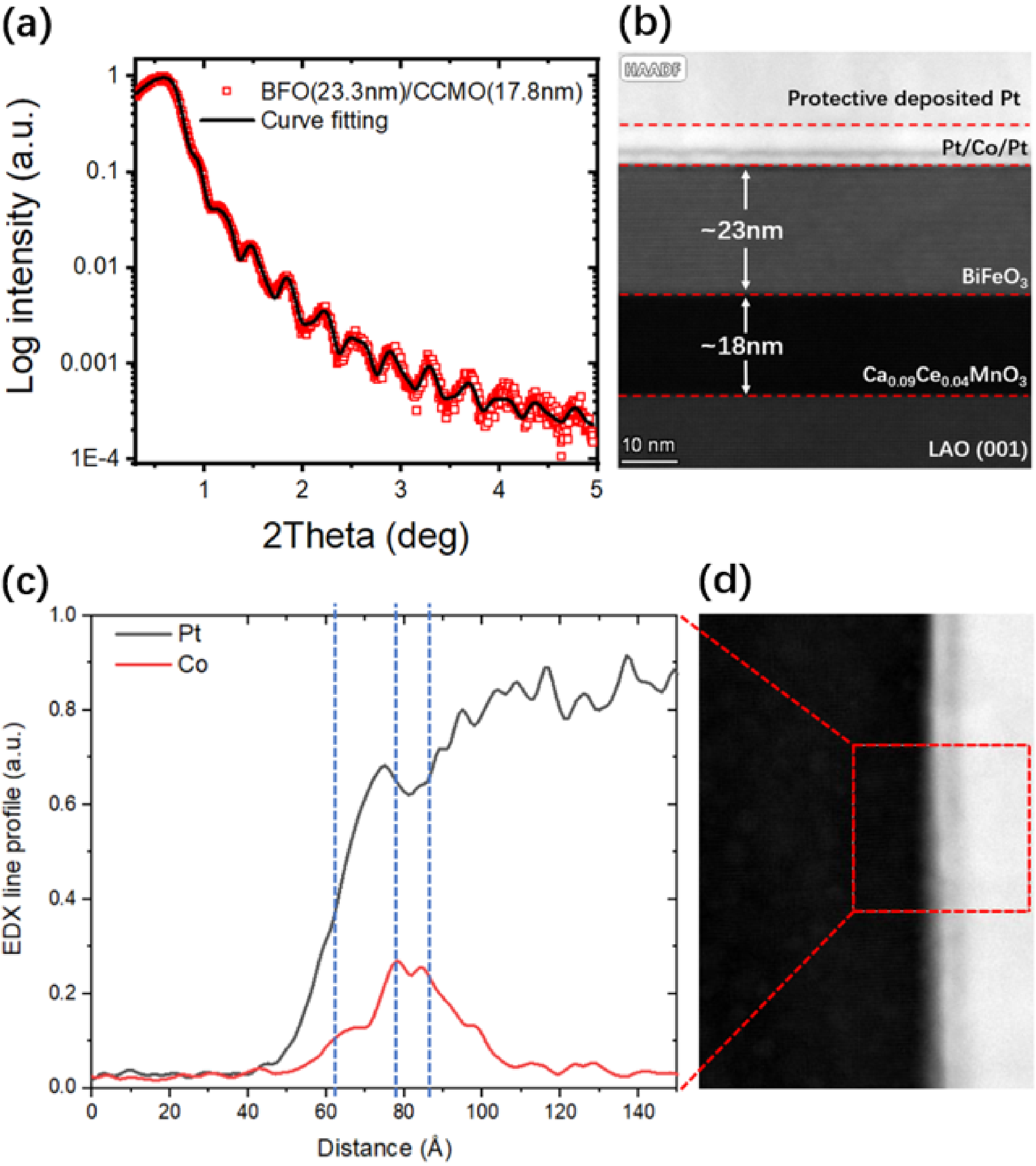

Figure 4.2: Thickness of the BFO/CCMO structure sample can be simulated from the X-Ray Reflectivity (XRR) data (a) and checked by TEM imaging (b). Thickness of the Pt/Co/Pt structure is determined from the growth rate of Pt and Co and checked by EDX line profile (c, d).

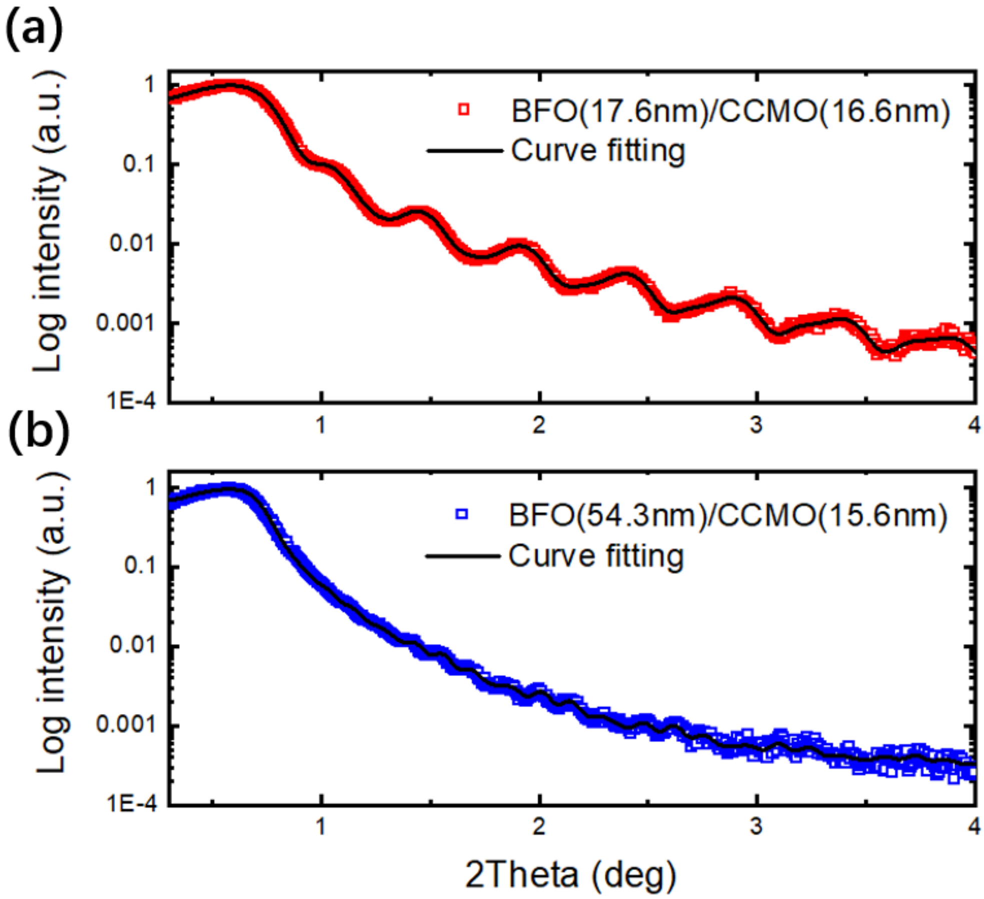

Figure 4.3: XRR of a thin BFO film (a) and a thick BFO film (b) grown on CCMO buffered LAO substrates. Their thicknesses are determined to be 17.6 *nm* and 54.3 *nm*, respectively.

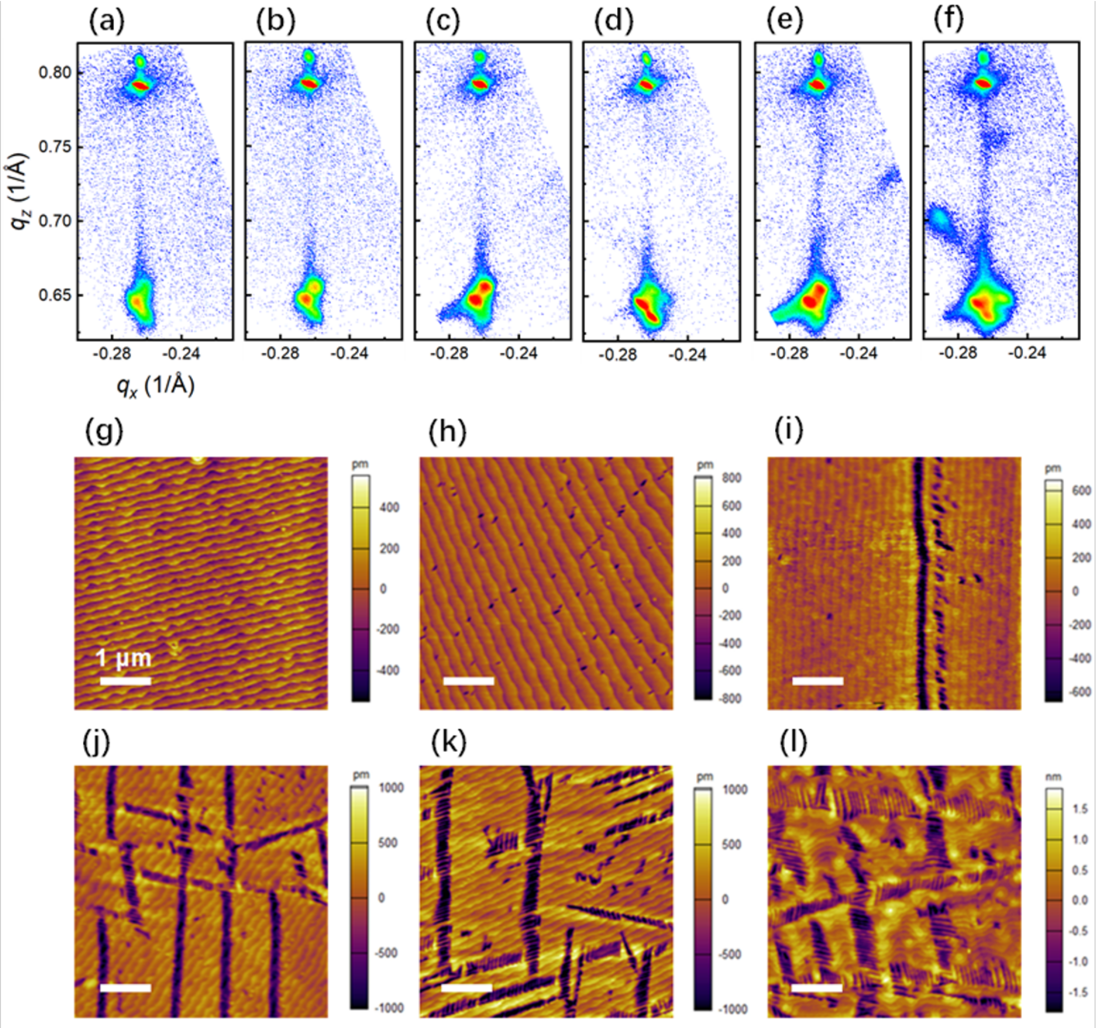

Figure 4.4: X-ray reciprocal space mapping (RSM) plots along ($\bar{1}03$) direction for BFO(17 nm), BFO(23 nm), BFO(38 nm), BFO(43 nm), BFO(54 nm) and BFO(77 nm) on 16nm-CCMO buffered LAO substrates are presented in (a)-(f), respectively. The atomic force microscopy (AFM) images for (a)-(f) are (g)-(l), respectively.

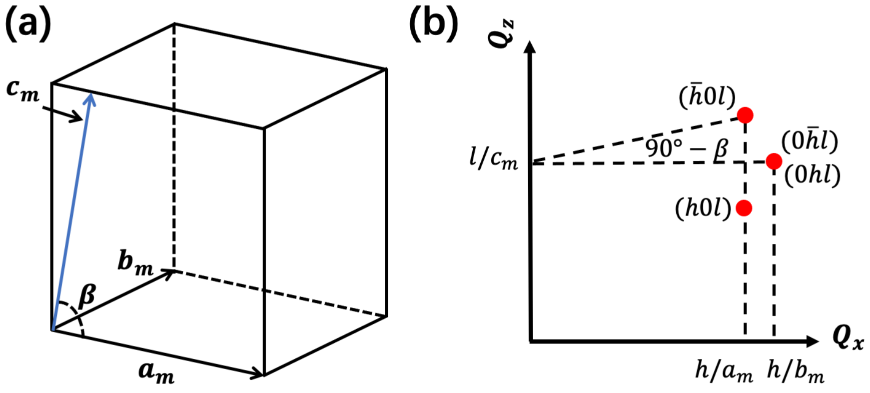

Figure 4.5: Schematic of (a) the M_C-type monoclinic unit cell and (b) reciprocal-space maps around the $(h0l)$ reflection for the monoclinic M_C phase.

along [100] direction, where β is the angle between c_m and a_m-b_m plane. In addition, there are four equivalent skewing directions for the monoclinic M_C phase, e.g. [100], $[\bar{1}00]$, [010] and $[0\bar{1}0]$, corresponding to the four domains of the M_C phase. Using the d-spacing formula for monoclinic structure (Eq. 3.6), we find that:

$$\frac{1}{d_{\bar{h}0l}} > \frac{1}{d_{0\bar{h}l}} = \frac{1}{d_{0hl}} > \frac{1}{d_{h0l}}. \tag{4.1}$$

Hence, the $(h0l)$ reflection of the M_C phase will split into three adjacent peaks: $(\bar{h}0l)$ peak is shifted upward and $(h0l)$ peak is shifted downward with $(0\bar{h}l)$ and $(0hl)$ peaks at the central (FIG. 4.5 b).

Following Chen *et al.*'s terminology [42], we denote this M_C distorted phase as tetrogonal (T-) like phase. Using the definition of the reciprocal lattice vectors, the lattice parameters (a_m, b_m, c_m, and β) of the T-like phase fulfill the geometric relations sketched in Figure 4.5 (b), thus we can extract the lattice parameters of the T-like phase BFO from the RSMs as shown in Table 4.2.

Although the lattice parameters extracted from RSMs are not accurate due to the large errors in determining the peak positions, our result agrees qualitatively with previous studies on BFO grown on LAO [23, 42, 43]. The lattice parameter along c-axis is elongated to ~ 4.65 Å, while the in-plane lattices (~ 3.8 Å) are still strained with the LAO substrates, the tetragonality $(2c/(a+b))$ is estimated to be ~ 1.23.

When the BFO thickness is less than ~ 25 nm, only T-like phase is seen from the RSMs (Figure 4.4 a, b) and more diffraction peaks are found as the BFO thickness

ID	Sample	a_m (Å)	b_m (Å)	c_m (Å)	β (°)
(a)	BFO (17 nm)	3.81 ± 0.03	3.75 ± 0.03	4.64 ± 0.01	88.5 ± 0.5
(b)	BFO (23 nm)	3.84 ± 0.02	3.77 ± 0.02	4.64 ± 0.01	88.2 ± 0.3
(c)	BFO (38 nm)	3.85 ± 0.03	3.77 ± 0.02	4.64 ± 0.01	88.1 ± 0.3
(d)	BFO (43 nm)	3.83 ± 0.02	3.75 ± 0.02	4.65 ± 0.01	88.1 ± 0.3
(e)	BFO (54 nm)	3.81 ± 0.02	3.72 ± 0.02	4.65 ± 0.01	88.2 ± 0.3
(f)	BFO (77 nm)	3.79 ± 0.02	3.72 ± 0.02	4.66 ± 0.01	88.4 ± 0.4

Table 4.2: The lattice parameters of M_C phase extracted from the RSMs in Figure (4.4).

increases (Figure 4.4 c, d, e, and f). This implies that there are multiple phases co-existed in thick BFO samples to relax the strain.

To illustrate the BFO phases clearly, two thick BFO films ($\sim$ 100 nm, derived from the growth rate calculation) on LAO substrate and CCMO buffered LAO substrate are grown for the XRD scan. From the XRD and RSM, we can see that introduction of the CCMO as the buffer layer does not change the phases of BFO. A clear R-like BFO peak is identified around 45.5° in the (002) region, two other vague peaks which can be denoted as S_0 [44] and Triclinic (Tri-) 1 [45] from previous literature are also observed in the (002) region (Figure 4.6 a). Aside from R-like, Tri-1 and S_0, Tri-2 is identified through the RSM($\bar{1}03$) scan for both samples (Figure 4.6 b, c). For convenience, we refer to these thicker BFO samples with multiple phase coexistence as mixed phase BFO (shortened as M-BFO), thin BFO samples with only T-like phase as pure T-like phase (shortened as T-BFO).

Atomic force microscopy and piezoresponse force microscopy

Surface topography and out-of-plane piezoresponse force microscopy (PFM) measurements were carried out on an Asylum Research MFP-3D-SA scanning probe microscope in AC and PFM modes at room temperatrure.

Thin BFO samples have a perfect step-terrace featured morphology which are presented in Figure 4.4 (g) and (h). When the sample thickness is larger than $\sim$ 25 nm, the darker region with a striped structure emerges at the step-terrace featured sample surface. As the sample thickness increases, the darker region expands to larger

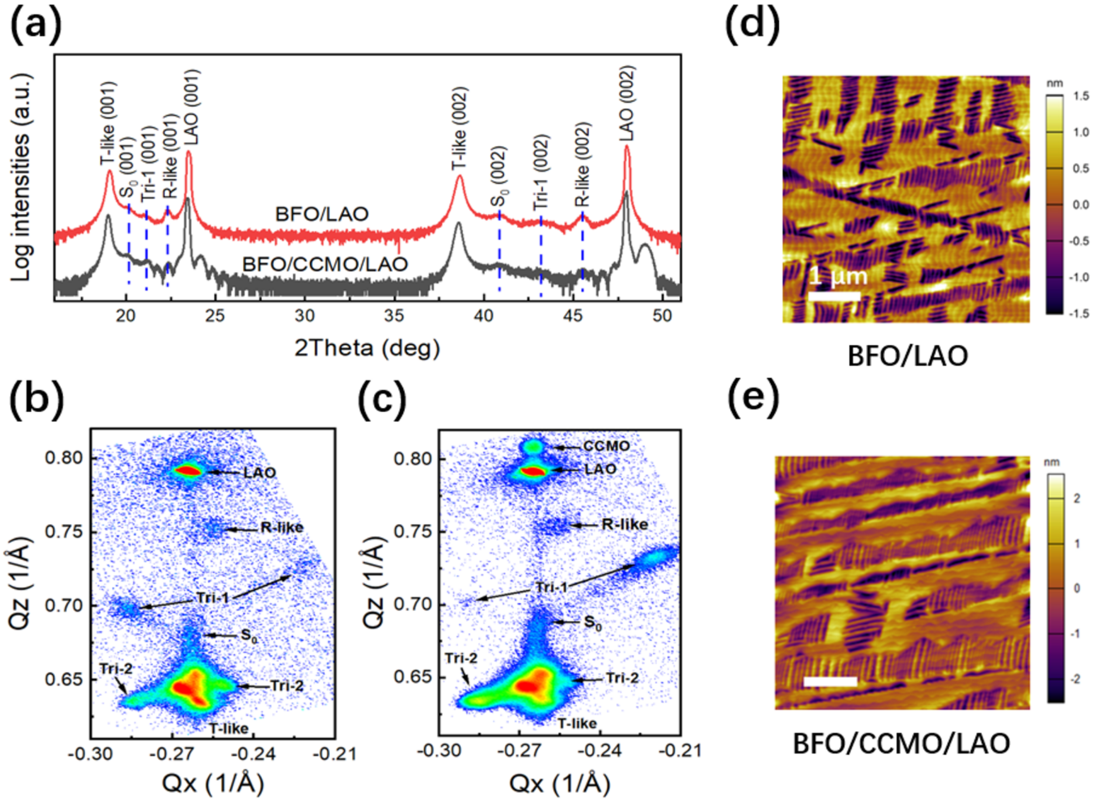

Figure 4.6: (a) X-ray $\theta - 2\theta$ scans for mixed phase BFO on LAO and CCMO buffered LAO, respectively. RSM($\bar{1}03$) scans for mixed phase BFO on LAO (b) and CCMO buffered LAO (c), respectively. AFM topography images for mixed phase BFO on LAO (d) and CCMO buffered LAO (e), respectively.

fraction of the sample surface (Figure 4.4 i - l and Figure 4.6 d, e). The step-terrace morphology has an atomic flatness, the step height is one unit cell (~ 4 Å), the step width is ~ 200 nm as shown in Figure (4.7).

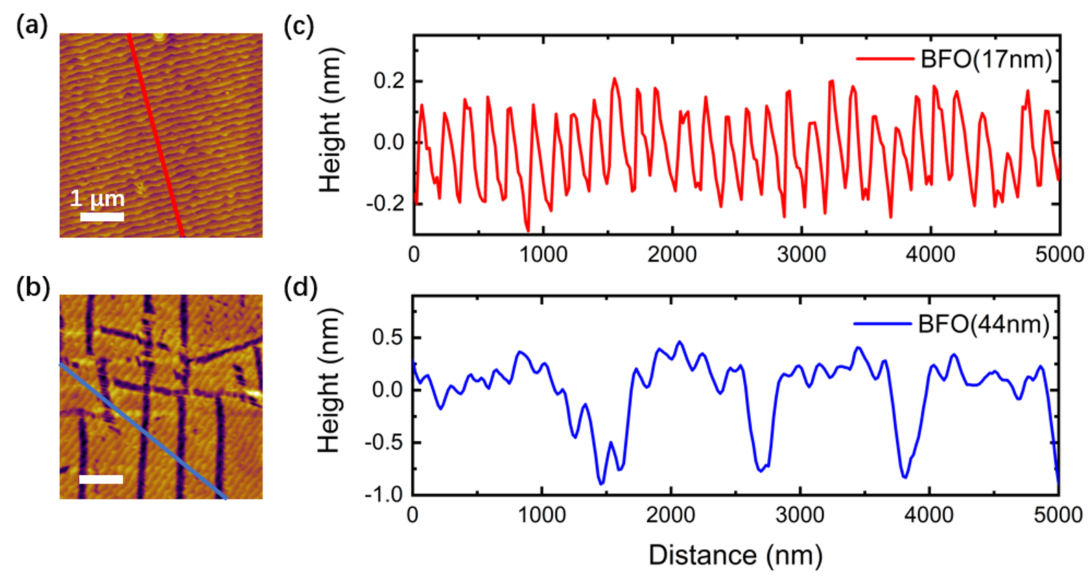

Figure 4.7: Atomic force microscopy topography image of a pure T-like phase BFO sample (a) and a mixed phase BFO sample (b). (c) Cross-section line profile along the red line in (a). (d) Cross-section line profile along the blue line in (b). Both lines are perpendicular to the steps on BFO.

The ferroelectric property of the BFO thin film is examined through the piezoresponse force microscopy (PFM), domain switching images after electric poling and the local hysteresis loops are recorded. Figure 4.8 (a) shows the out-of-plane PFM phase image of BFO domains after the poling with ± 5V. The sharp phase contrasts reveal that the BFO domains are switched into two opposite orientations respectively, indicating that the polarization state is indeed reversible. The out-of-plane phase signal of as-grown BFO has the same color tone as the + 5V poled region, indicating that the as-grown BFO has a spontaneous downward polarization. Bulk polarization of ferroelectric material can be engineered by the electrostatic boundary condition. In this case, the interfacial CCMO/BFO is $Ca_{0.96}Ce_{0.04}O$ termination, which leads to the downward polarization orientation in BFO [41].

The out-of-plane amplitude signal after the poling with ± 5V is presented in Figure

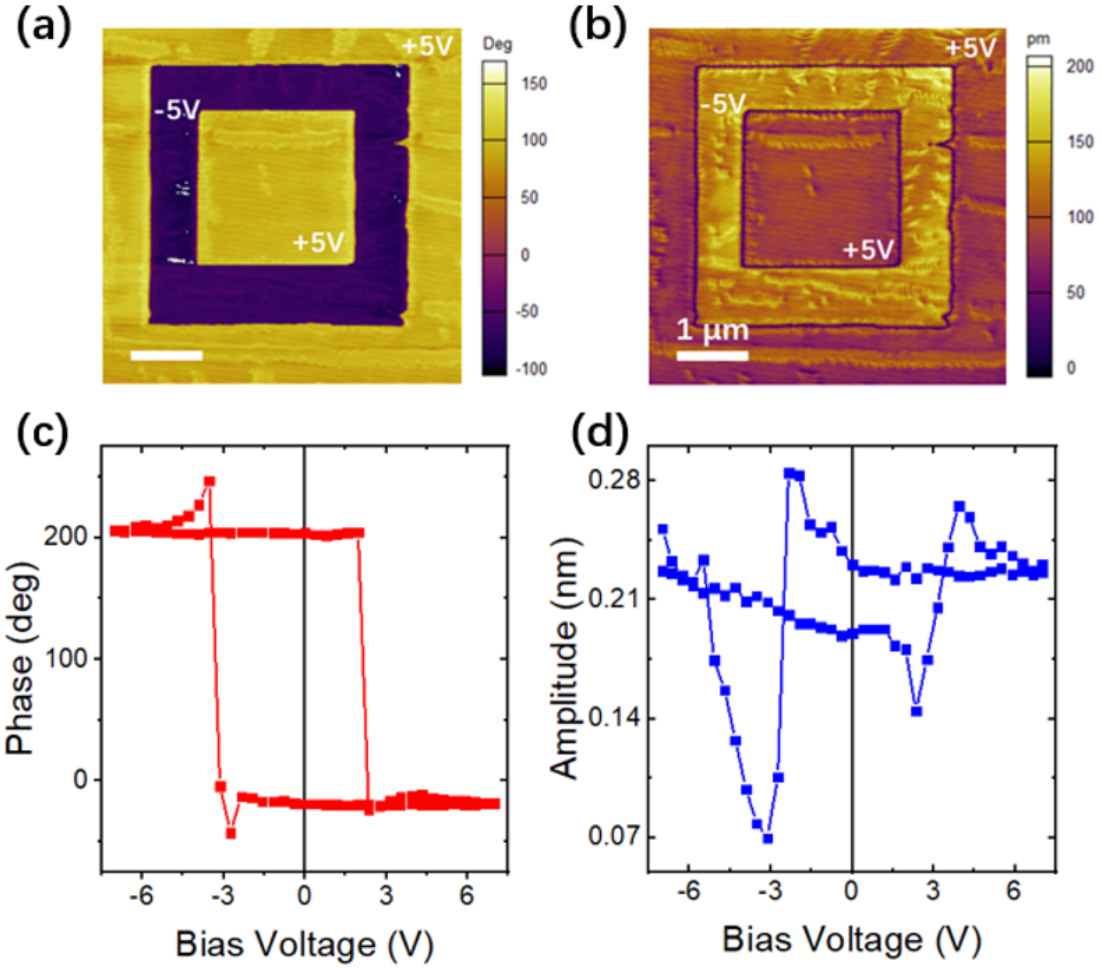

Figure 4.8: PFM of out-of-plane phase image (a) and amplitude image (b) of the BFO film under electrically writing of ± 5V. Local PFM hysteresis loop: phase signal (c) and amplitude signal (d).

4.8 (b), domain walls are observed at the boundaries of the -5V poled region, indicating that the domains in the ± 5V poled regions are aligned in the opposite out-of-plane directions. Figure 4.8 (c) and (d) present the hysteresis loop with 180° switching and the butterfly-like amplitude loop, respectively. The phase loop in Figure 4.8 (c) is asymmetry as observed in previous reference[46], which is explained by the internal bias field in the BFO film from the asymmetric built-in fields at the BFO/CCMO interface and/or asymmetric distributions of trapped charges[47].

The polarization of BFO can be engineered by choosing different BFO/oxide interface [48, 49], for example the BFO thin film grown on SRO-coated STO substrate has a downward polarization and the BFO thin film grown directly on STO substrate has an upward polarization [49]. It is extremely valuable for us to study the influence of BFO polarization on magnetic properties of the adjacent magnetic multilayers. Unfortunately, the Thomas-fermi screening length [50, 51] of Pt is very small (~ 0.6Å) [52], the electric field generated by the polarization will be screened completely by the seed Pt layer of $\sim 1\ nm$ thickness.

The magnetic properties of thin BFO films on CCMO buffered LAO substrates

The ferromagnetism of epitaxial thin BFO film is a long time controversial problem, it is now believed that there is no significant ferromagnetism for pure phase BFO. It is a G-type anti-ferromagnet (AFM) plus a weak ferromagnetism caused by the canting of the neighboring anti-aligned spins for the R-like phase BFO. The saturation magnetization of R-like BFO thin film measured by SQUID-VSM is usually as small as $\sim$ 1emu/cm^3 [53]. Large saturation magnetization values measured in R-like BFO thin films are usually attributed to the appearance of $\gamma - \mathrm{Fe_2O_3}$ impurity phase [54].

For T-like BFO, neutron scattering measurements have confirmed the existence of G-type antiferromagnetism and the Néel temperature (T_N) is estimated to be $324K$ [55]. In addition to the G-type AFM structure with spin moments confined to the film plane, the C-type AFM structure as the minority phase is also identified. The pure T-like phase BFO film has negligible saturation magnetization (smaller than 1emu/cm^3) via SQUID-VSM measurements as demonstrated by He et al. [56], but mixed phase BFO film has larger saturation magnetization of 5-8 emu/cm^3. The existence of R-like phase and T-R phase boundaries in mixed phase BFO renders the larger saturation magnetization. In addition, the magnetic moment of the mixed phase BFO is more likely to distribute on the surface of the thin film, making the mixed phase BFO a valuable object for studying the coupling between the BFO thin film and the adjacent FM layer.

In this research, we fabricate BFO thin films on CCMO buffered LAO substrates. Epitaxial CCMO thin films on compressive $\mathrm{YAlO_3}$ (YAO) substrates ($a_{pc} = 3.71\text{Å}$) exhibit a FM phase transition at $\sim$ 110K [57], and the coercive field for CCMO film at 15K is $\sim$ 1 T. But CCMO has a little smaller lattice constant ($a_{pc} = 3.77\text{Å}$) than that of LAO ($a_{pc} = 3.79\text{Å}$), whether the CCMO thin film on tensile strained LAO substrate is FM or not at low temperature is not clear to us.

Using the SQUID-VSM, we measured the magnetic properties of the BFO thin films grown on LAO substrate and CCMO buffered LAO substrate. Room temperature magnetization hysteresis curves for BFO thin films of similar thicknesses ($\sim 40\ nm$) on LAO substrate and CCMO buffered LAO substrate are presented in Figure (4.9) (a) and (b). Both samples are mixed phase BFO samples, and they have similar saturation magnetization values of $\sim$ 5emu/cm^3 measured at the in-plane geometry which are in agreement with the results obtained by He et al [56]. The out-of-plane saturation magnetization for BFO on CCMO buffered LAO substrate ($\sim$ 9emu/cm^3) is slightly higher that that for BFO on LAO substrate ($\sim$ 8emu/cm^3). In summary, there are no significant differences observed from the M vs H measurements for BFO thin films on LAO substrate and CCMO buffered LAO substrate. The magnetic contribution from CCMO can be neglected because the CCMO is not a ferromagnetic material at room temperature.

Figure (4.9) (c) shows the field cooled (FC) magnetic moment M vs T of Pt/Co/Pt on BFO on CCMO buffered LAO measured at the out-of-plane geometry. In this research, we are interested in the magnetic properties of the Co/Pt multilayers grown on BFO, to avoid the contribution coming from the BFO and the CCMO layers, following procedure is employed. The sample is first demagnetized and then cooled down to 10K in 300 Oe. Then a field of 50 Oe was applied, the M vs T curve was measured upon warming. Since 300 Oe is strong enough to magnetize the Co/Pt multilayers to saturation magnetization and not strong enough to magnetize the BFO and the CCMO layers, the $M(T)$ curve obtained from this procedure only reflects the temperature dependent magnetic properties of the Co/Pt multilayers on BFO. From Figure 4.9 (c),

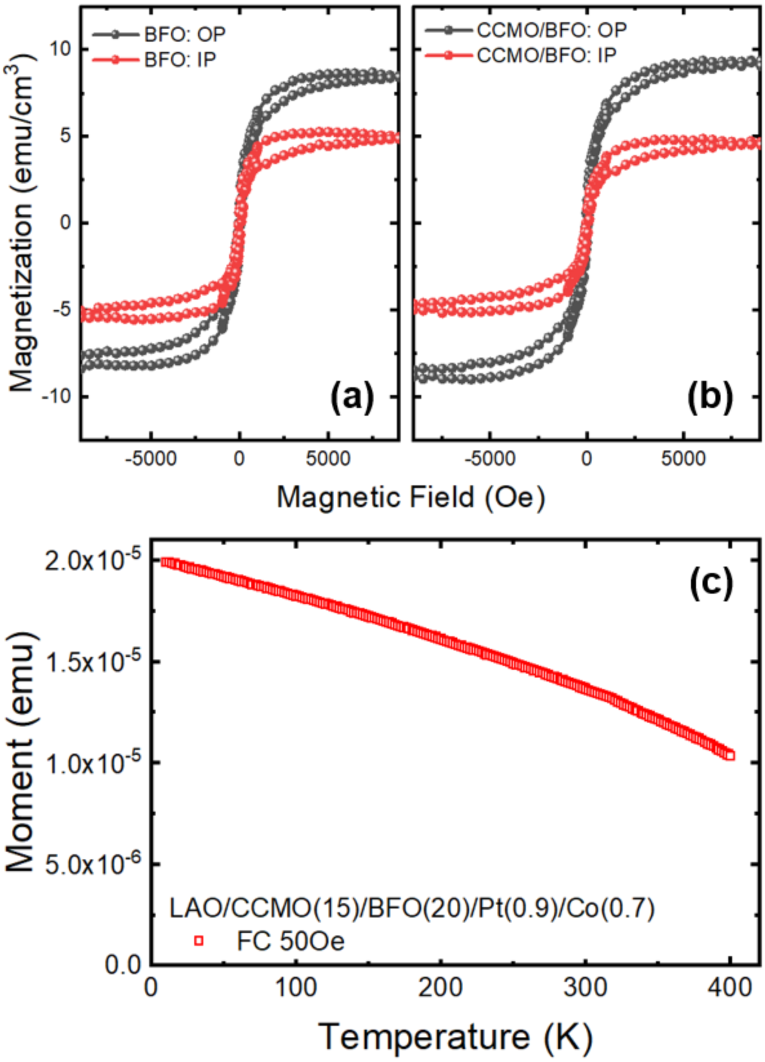

Figure 4.9: M vs H hysteresis curves for (a) BFO(40)/LAO and (b) BFO(43.6)/CCMO(15)/ LAO measured at room temperature, respectively. (c) Field cooled (FC) out-of-plane measurement of M vs T for Pt(4)/Co(0.7)/Pt(0.9) on BFO(20)/CCMO(15)/ LAO measured at the field of 50 Oe.

we can also see that the FC $M(T)$ curve is flat and continuous from 10K to 400K, there is no evidence of mixing significant magnetic contribution from the BFO layer or the CCMO layer.

4.2.2 DC sputtering of Pt/Co/Pt trilayers on BFO

Pt/Co/Pt trilayers were deposited by DC magnetron sputtering at room temperature in a 2.0 mTorr Ar atmosphere. Pt and Co targets were deposited with 30W. The deposition rates were $\sim 1.0\text{Å}/s$ for Pt and $\sim 0.5\text{Å}/s$ for Co. The trilayers sputtered on BFO in this Chapter consist of Pt(1.2)/Co(0.7)/Pt(4) (numbers in parentheses are nominal thicknesses in nanometer throughout the thesis, unless stated otherwise), the seed Pt layer of 1.2 *nm* is sputtered first on BFO, then 0.7 *nm* of Co, finally a 4 *nm*-Pt capping layer is sputtered. The thickness of Pt and Co are determined by the growth rate of Pt and Co respectively, and checked by TEM (Figure 4.2 c, d) and XRR simulation (Figure 3.6).

Comparison of different surface treatments

Quality of perovskite oxide/Pt interface is another crucial factor for obtaining PMA in Pt/Co/Pt trilayer structures. The best way for obtaining high quality interface is to use a multi-chamber system which guarantees the sputtering of metal layers without breaking the vacuum condition. Due to the limitation of the facilities, we have to take the samples out of the PLD chamber before transferring them to the sputtering chamber. The samples are kept in the lab for several days or longer time before we have the time-slot for sputtering. The sample surface is likely to be contaminated or deteriorated by the surrounding air during this process. Aside from the dust, the surface of the $BiFeO_3$ layer is easily adsorbed or attached by CO_2 and H_2O when exposed to air. Contamination of the BFO surface upon exposure to air may have adverse effects on the magnetic properties of the Pt/Co multilayer.

To clean the sample surface and keep the sample surface at the same growth condition, acetone or isopropanol (IPA) is usually used for cleaning the sample surface. A recent study [58] shows that different surface treatments of the perovskite oxides may result different magnetic hysteresis loops for the covering metal magnetic layers. A successful surface treatment is identified as the most perfect squareness of the out-of-plane AHE hysteresis loop.

To study the influence of different surface treatments of BFO on the magnetic properties of the covering Pt/Co/Pt trilayers. Mixed phase BFO thin films of about 45 *nm* are chosen for the investigation, several types of surface treatments are employed for these samples:

- As deposited sample: S1.
- Acetone clean using soaked cotton ball: S2, S3, S4.
- Ultrasonic acetone clean for 10 min: S5.

Figure 4.10 presents AHE measurements on Pt/Co/Pt trilayers on six different mixed phase BFO samples. S1 is the as deposited BFO sample which means we put it immediately into the sputtering chamber when we took it out from the PLD chamber. It is not surprising that Pt/Co/Pt trilayer on S1 has the most perfect squareness of the AHE hysteresis loop.

Acetone is a commonly used chemical cleaning agent which is very efficient for removing organic molecules such as fats. S2, S3 and S4 are three BFO samples with different exposure time, 5 hour, 10 days and 100 days respectively. Although these three samples are all cleaned by acetone-soaked cotton ball, none of them has a perfect square-shaped AHE hysteresis loop. S5 and S6 are two BFO samples with similar exposure time of about 300 days. S5 is ultrasonic cleaned in acetone for 10 minutes and S6 is untreated. Pt/Co/Pt on S5 has a much improved square-shaped AHE hysteresis loop, although the squareness is not as good as the Pt/Co/Pt on as deposited BFO sample. Pt/Co/Pt on S6 has the most slant-shaped AHE hysteresis loop.

To make the following studies more comparable and repeatable, only as-deposited BFO samples are used for DC sputtering of the metal layers in this project.

4.3 Magnetic Characterization

4.3.1 Magnetic properties of Pt(t_{Pt} nm)/Co(0.7 nm)/Pt(4 nm) trilayers on BFO

Pt(t_{Pt})/Co(0.7)/Pt(4) trilayers with various Pt seed layer thicknesses are sputtered via DC magnetron sputtering on pure T-like phase BFO (T-BFO) and mixed phase BFO (M-BFO). The pure T-like phase BFO films with similar thicknesses of about 20 *nm* are

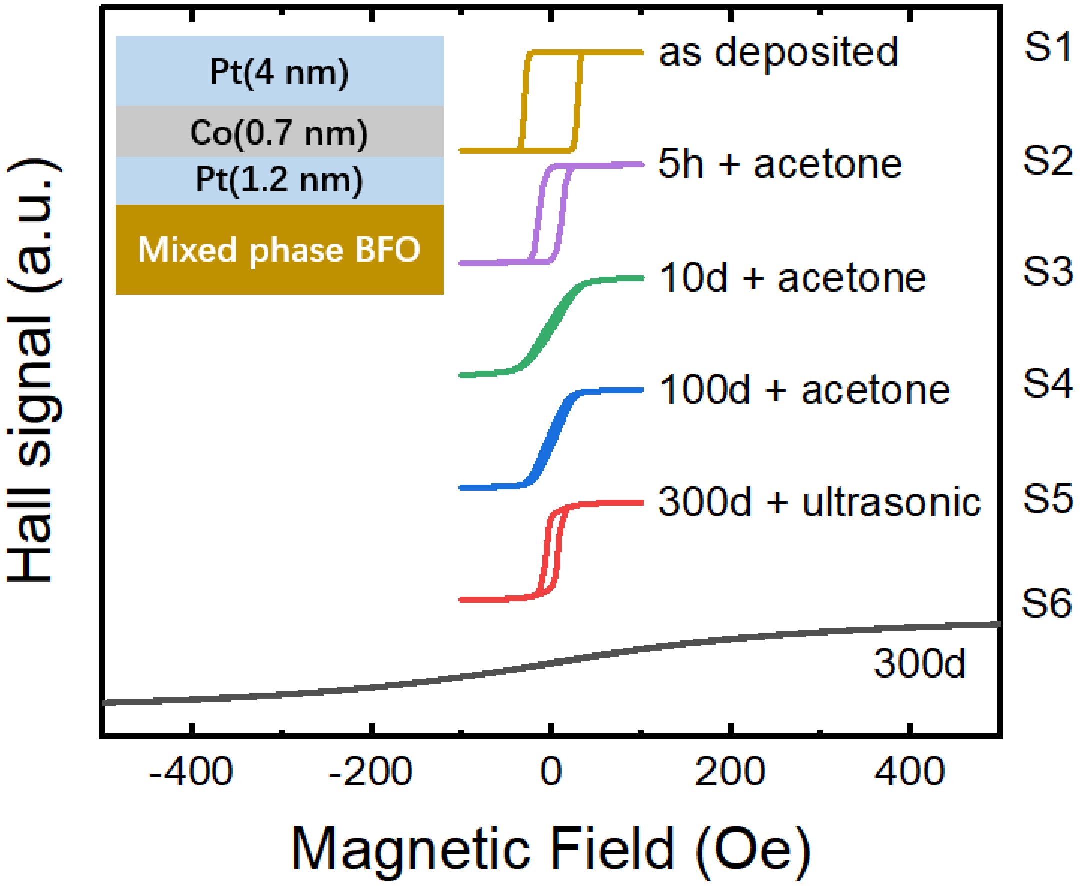

Figure 4.10: AHE signal for Pt/Co/Pt trilayer on as-deposited BFO film (S1) which has the most perfect square-shaped hysteresis loop. AHE signal for Pt/Co/Pt trilayer on acetone cleaned BFO film exposed in air for 5 hours (S2) has a deteriorated square-shaped hysteresis loop. AHE signals for Pt/Co/Pt trilayers on acetone cleaned BFO films exposed in air for 10 days (S3) and 100 days (S4) have more slant-shaped hysteresis loops. AHE signal for Pt/Co/Pt trilayer on ultrasonic acetone cleaned BFO film exposed in air for 300 days (S5) has a much improved square-shaped hysteresis loop. AHE signal for Pt/Co/Pt trilayer on untreated BFO film exposed in air for 300 days (S6) has the most slant-shaped hysteresis loop.

deposited on 16-nm CCMO buffered LAO substrates. The pure T-like BFO film has a perfect step-terrace featured surface with a very small surface roughness of about 130 pm. Sputtering of Pt/Co/Pt trilayers on BFO does not change the surface topography significantly, which signifies the very high quality of the DC sputtering.

Figure 4.11 (a) presents the AHE signals for Pt(t_{Pt})/Co(0.7)/Pt(4) trilayers on pure T-like phase BFO films. Square-shaped AHE hysteresis loops, indicating good PMA for Pt/Co/Pt trilayers on BFO are obtained for Pt seed layer as thin as 0.9 nm. The coercive field H_{c} increases as the Pt seed layer thickness increases (Figure 4.11 c, black open squares). The Pt(0.6)/Co/Pt trilayer has a slant-shaped AHE hysteresis loop, which signifies the loss of PMA, or vanish of the effective perpendicular magnetic anisotropy energy K_{eff}. This decreasing tendency of H_{c} can be explained as the deteriorated Co/Pt interface caused by the very thin Pt seed layer.

AHE signals for Pt/Co/Pt trilayers on mixed phase BFO with thicknesses of about 45 nm are presented in Figure 4.11 (b). The typical AFM topography for mixed-phase BFO is shown in Figure 4.7 (b), the shark gill-shaped dark region which corresponds to the R-like phase BFO is embedded in the brighter T-like phase BFO. The typical surface roughness for 45 nm-thick mixed-phase BFO is about 300 pm. The Pt/Co/Pt trilayer on mixed-phase BFO also lost the PMA when Pt seed layer is $\sim$ 0.6 nm thick. The overall trending of H_{c} (Figure 4.11 c) of Pt/Co/Pt on mixed-phase BFO (red open squares) is similar with Pt/Co/Pt on T-like phase BFO (black open squares). To investigate the different influence of mixed-phase BFO and pure T-like phase BFO on covering Pt/Co/Pt quantitively, we shall measure the anisotropy field H_{A} and then calculate the magnetic anisotropy energy density K_{eff}.

The perfect squareness of AHE hysteresis loop of Pt/Co/Pt on BFO thin film (Figure 4.11 a and b) indicates that the magnetization switches uniformly over the sample, which guarantees the precise measurement of anisotropy field H_{A} using the anomalous Hall effect (AHE).

As an example, we determine the anisotropy field of Pt(1.2)/Co(0.7)/Pt(4) on pure T-like phase BFO thin film from both the AHE measurement and the in-plane SQUID-VSM measurement. The AHE signal for Pt(1.2)/Co(0.7)/Pt(4) on pure T-like phase BFO thin film is presented in Figure 4.11 (a) (blue line). The anisotropy field derived from AHE measurement in Figure 4.12 (a) is about 2200 Oe, which is in good agreement with the value derived from the in-plane SQUID-VSM measurement in Figure 4.12 (b).

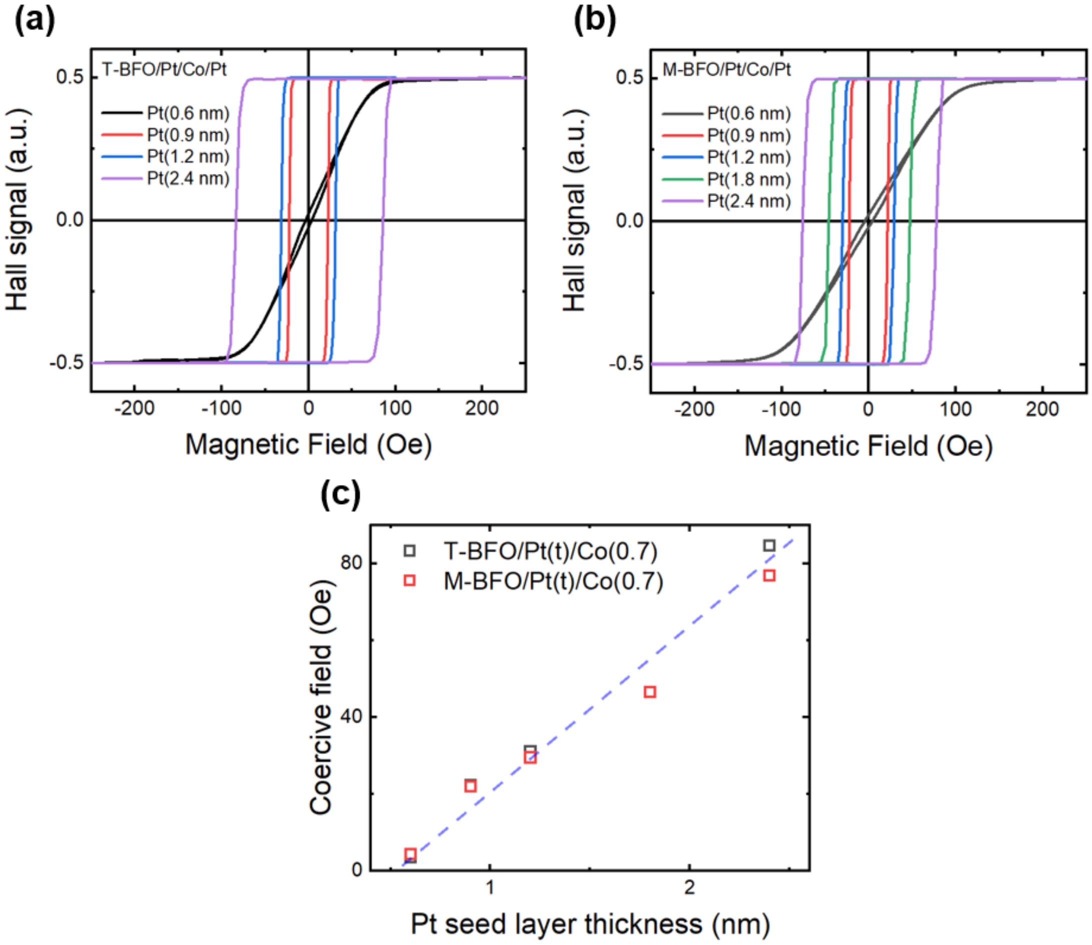

Figure 4.11: AHE signals for Pt(t_{Pt})/Co(0.7)/Pt(4) trilayers with different thicknesses of seed Pt layer on (a) pure T-like phase BFO thin films and (b) mixed-phase BFO thin films, respectively. Square-shaped AHE hysteresis loops are obtained for all Pt seed layer thicknesses except for the thinnest 0.6 *nm* case. (c) The coercive field (H_c) drops monotonously as the Pt seed layer thickness decreases. The dashed blue line in the figure is a guide to the eye.

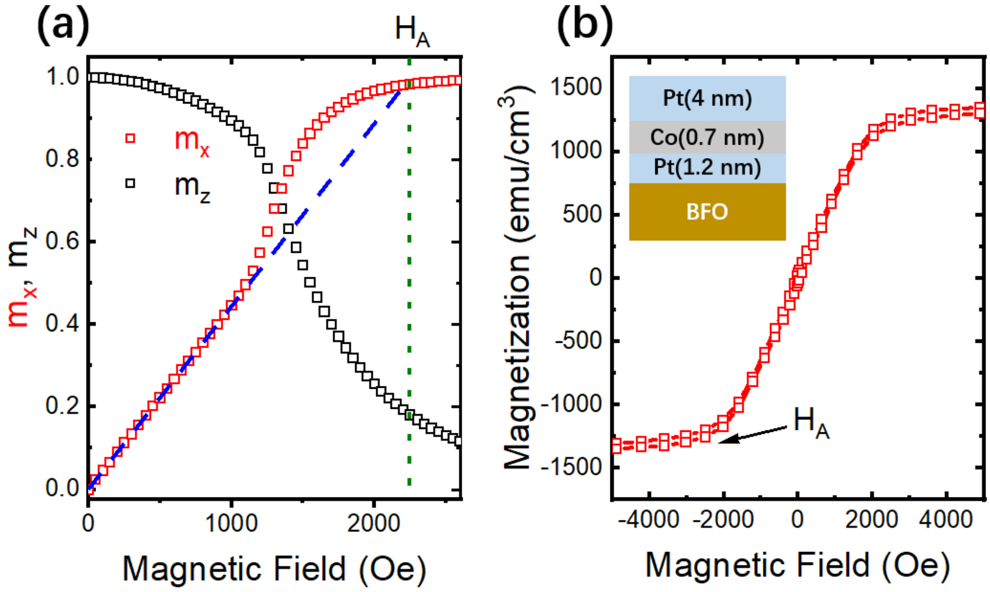

Figure 4.12: Anisotropy field derived from (a) AHE measurement and (b) in-plane SQUID-VSM measurement.

Since the AHE signal only reflects the magnetization of metal layer, it is more accurate and appropriate for us to derive the anisotropy field of Pt/Co/Pt on BFO from the AHE measurement.

Figure 4.13 (a) presents the anisotropy field of Pt/Co/Pt with various Pt seed layer thicknesses on pure T-like BFO (black open squares) and mixed-phase BFO (red open squares) thin films, respectively. The anisotropy fields of Pt/Co/Pt on both pure T-like and mixed phase BFO thin films rise as the Pt seed layer thickness increases. For Pt seed layer thickness larger than $\sim 2\ nm$, the anisotropy field (H_A) of Pt/Co/Pt on mixed-phase BFO is about 3000 Oe and stabilizes around this value (Figure 4.13 a). Pt/Co/Pt trilayers on both pure T-like phase and mixed-phase BFO thin films have similar anisotropy fields of $\sim$ 3000 Oe for large Pt seed layer thickness of 2.4 nm. For thin Pt seed layer thicknesses, e.g. 0.9 nm and 1.2 nm, anisotropy fields of Pt/Co/Pt trilayers on pure T-like BFO films are larger than those of Pt/Co/Pt trilayers on mixed phase BFO films, suggesting that pure T-like BFO thin films have a more favorable condition than mixed phase BFO films for hosting the PMA.

The effective perpendicular magnetic anisotropy K_{eff} (Figure 4.13 b) obtained from calculating $K_{eff} = \frac{\mu_0}{2} M_\mathrm{S} H_\mathrm{A}$ is usually used for quantify the degree of PMA, where M_S

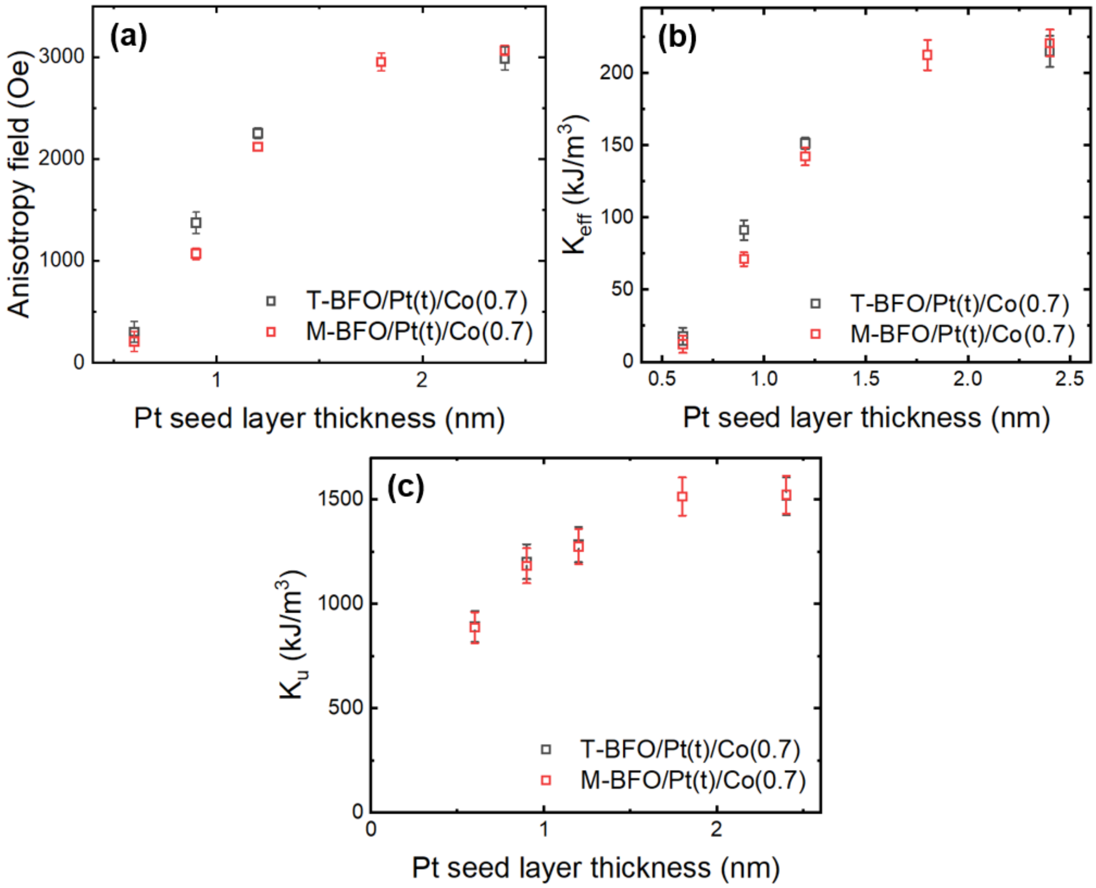

Figure 4.13: (a) Anisotropy field for Pt(t_{Pt} nm)/Co(0.7 nm)/Pt(4 nm) on T-like phase BFO (open black dots) and mixed phase BFO (open red dots), respectively. (b) The effective perpendicular anisotropy (K_{eff}) rises as the Pt seed layer thickness increases, and it becomes saturated when the Pt layer thickness is $\sim$ 2 nm. (c) The intrinsic perpendicular anisotropy (K_u), drops when the Pt seed layer thickness decreases.

is measured from the SQUID-VSM measurement for each sample.

Considering

$$K_{eff} = \left(K_V - \frac{\mu_0}{2}M_S^2\right) + \frac{K_S^{up}}{t} + \frac{K_S^{down}}{t}, \tag{4.2}$$

where t is the cobalt layer thickness, K_V is the bulk anisotropy, $-\frac{1}{2}\mu_0 M_S^2$ is the shape anisotropy, K_S^{up} and K_S^{down} correspond to the up Co/Pt interface anisotropy and down Pt/Co interface anisotropy. Since all samples studied here are covered by the same 4-nm Pt capping layer, we shall have similar K_S^{up} for all samples. The Pt seed layer thickness (t_{Pt}) dependence of K_{eff} shall mainly attribute to the down Pt/Co interface (K_S^{down}).

To make the discussion easier, we calculated the intrinsic perpendicular anisotropy K_u by accounting for the shape anisotropy $K_u = K_{eff} + \frac{\mu_0}{2}M_S^2$ (Figure 4.13 c). Now, K_u can be expressed as

$$K_u = K_V + \frac{K_S^{up}}{t} + \frac{K_S^{down}}{t} \tag{4.3}$$

Noting that the bulk anisotropy K_V is usually expected to be negligible for amorphous transition metal films [59], we approximated the K_u as

$$K_u \approx \frac{K_S^{up}}{t} + \frac{K_S^{down}}{t}. \tag{4.4}$$

The up Co/Pt interface usually has less contribution than the down Pt/Co interface to the total magnetic anisotropy [60] and the identical 4-nm Pt layers are covered on all samples, thus we only need to focus our discussions on the down Pt/Co interface as follows.

First the Pt/Co interface quality weakens as the Pt seed layer thickness (t_{Pt}) decreases and the Pt (111) texture expects to be lost completely when $t_{\mathrm{Pt}} < 1\mathrm{ML}$. Second the Pt atoms adjacent to Co layer are also magnetized due to the proximity effect at the Pt/Co interface which will lead to the enhancements of saturation magnetization M_{S} and Curie temperarure T_{c} for Pt/Co/Pt trilayers [60]. According to a X-ray magnetic circular dichroism study [61], the magnetic moment of the magnetized Pt atom decreases exponentially with the distance from the Pt/Co interface with a characteristic decay length of 0.41 nm. It is estimated that $\sim 90\%$ of the induced Pt magnetization is concentrated within a 1-nm ($\sim$ 4 ML) region close to the interface which corresponds to the thinnest Pt seed layer thickness of ~ 0.9 nm for establishing a firm PMA in Pt/Co/Pt structure on BFO. And the saturation of K_{eff} and K_u in Figure (4.13) when $t_{\mathrm{Pt}} \sim 2$ nm corresponds to ~ 99 % of the total induced Pt magnetization. Hence the behaviours of K_{eff} and K_u in Figure 4.13 (b) and (c) are qualitatively explained.

4.3.2 Magnetic properties of Pt(0.9 nm, 1.2 nm)/Co(0.7 nm)/Pt(4 nm) trilayers on BFO with different thicknesses

In this subsection, we study the BFO thickness influence of the magnetic properties of the upper grown Pt/Co/Pt trilayers. In Figure 4.13 (b) and (c), we already observed a decrease in K_{eff} and K_u upon increasing the BFO thickness. Two series of samples are sputtered, series A consists of the Pt/Co/Pt trilayers with fixed 1.2-*nm* Pt seed layers on BFO thin films of various thicknesses (from 20-70 *nm*), series B consists of the Pt/Co/Pt trilayers with smaller 0.9-*nm* Pt seed layers on BFO.

All samples have rectangular shaped hysteresis loops and no obvious exchange bias fields are observed. The coercive fields (H_{c}) are derived from the hysteresis loops and shown in Figure 4.14 (a). H_{c} decreases as the BFO thickness increases for both series. Figure 4.14 (b) shows the underlying BFO layer influence of the anisotropy field of the covering Pt/Co/Pt trilayer. The anisotropy fields for Pt(1.2)/Co(0.7)/Pt(4) trilayers on BFO of various thicknesses are between 1800 - 2200 Oe, which are significantly higher than those for Pt(0.9)/Co(0.7)/Pt(4) trilayers on BFO. What is more, Pt/Co/Pt trilayers on pure T-like phase BFO thin films have larger anisotropy fields than Pt/Co/Pt trilayers on mixed-phase BFO thin films, the difference is about 200 Oe for Pt(1.2)/Co(0.7)/Pt(4) trilayers (Figure 4.14 b, black) and about 350 Oe for Pt(0.9)/Co(0.7)/Pt(4) trilayers (Figure 4.14 b, red). But we cannot say H_{A} decreases as the BFO thickness increases, because there is an exception in Figure (4.14). The Pt(1.2)/Co(0.7)/Pt(4) on 69 *nm*-BFO has a larger H_{A} value than that of Pt(1.2)/Co(0.7) /Pt(4) on 52 *nm*-BFO. Similar exceptions also happened for the K_{eff} vs BFO thickness plot (Figure 4.14 c) and the K_u vs BFO thickness plot (Figure 4.14 d).

Mixing of the T-like phase and the R-like phase when the BFO film thickness is larger than 27 *nm* usually leads to a larger surface roughness due to the emergence of the morphotropic phase boundaries (MPB). The surface anisotropy K_S is always reduced by roughness [62–64], the change of the surface anisotropy ΔK_S can be estimated by

$$\frac{\Delta K_S}{K_S} = -\frac{2\sigma}{W}, \tag{4.5}$$

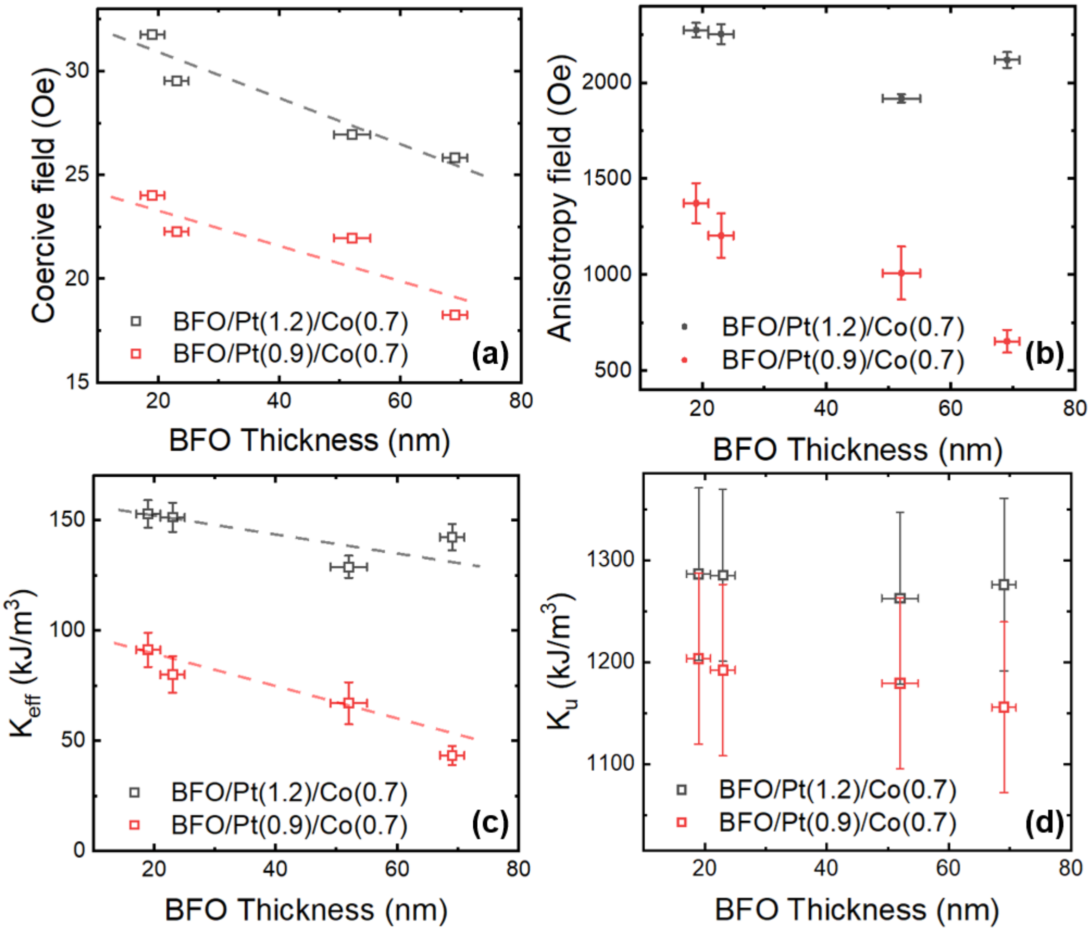

Figure 4.14: (a) Coercive fields H_c, (b) anisotropy fields H_A, (c) effective perpendicular magnetic anisotropies K_{eff} and (d) intrinsic perpendicular magnetic anisotropies K_u of Pt(0.9, 1.2)/Co(0.7)/Pt(4) trilayers on BFO thin films with different thicknesses.

where σ denotes the mean vertical deviation from a reference plane, and W is the average lateral size of flat areas. The existence of the step-and-terrace featured surface morphology for our samples makes the estimation of the formula (4.5) possible. Here we use the step width measured from AFM as W, and root mean square roughness of the films measured from AFM as σ. Although the surface roughness σ increases monotonously upon increasing the BFO thickness, the step width of the T-like matrix may vary from 50 nm - 400 nm regardless of the thickness of the BFO films, thus giving rise to the anomalous data point that goes against the apparent trend.

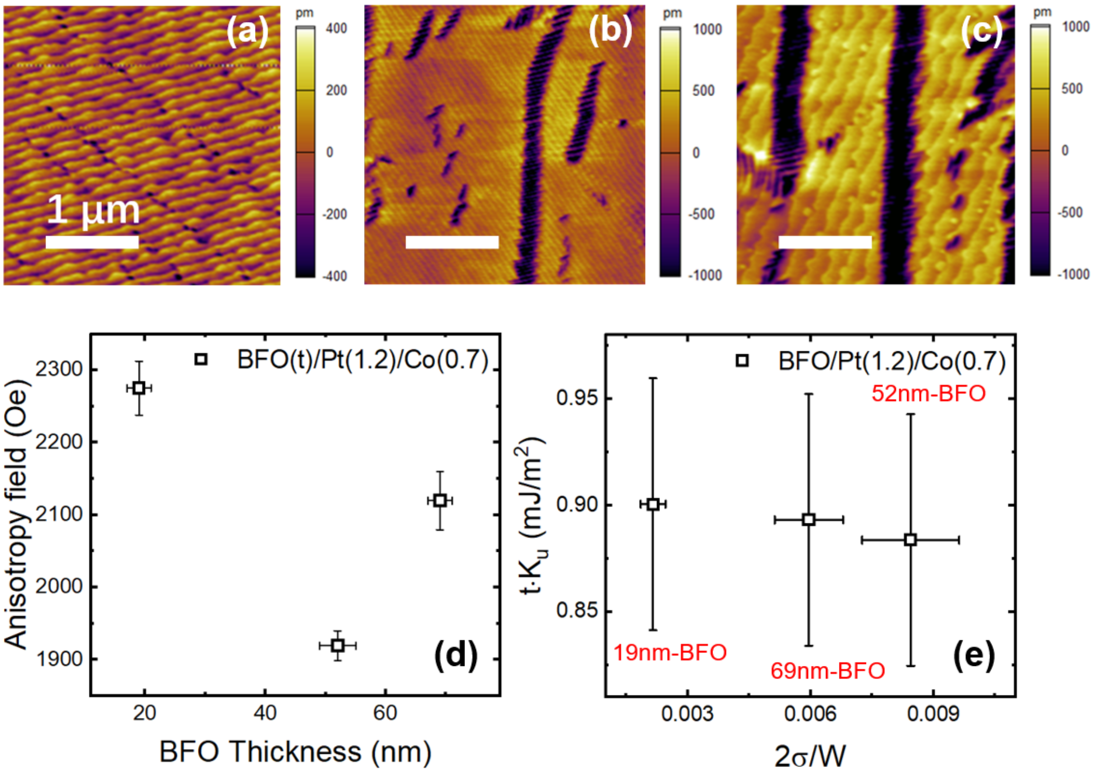

Figure 4.15: The AFM surface morphology images of (a) 19 *nm*-BFO, (b) 52 *nm*-BFO and (c) 69 *nm*-BFO samples, respectively. (d) Anisotropy fields H_A of Pt(1.2)/Co(0.7)/Pt(4) trilayers on 19 *nm*-BFO, 52 *nm*-BFO and 69 *nm*-BFO thin films. (e) The sheet intrinsic perpendicular magnetic anisotropies $t \cdot K_u$ vs $2\sigma/W$ plot of Pt(1.2)/Co(0.7)/Pt(4) trilayers on 19 *nm*-BFO, 52 *nm*-BFO and 69 *nm*-BFO thin films.

To elucidate the roughness influence of the magnetic properties of the Pt/Co/Pt trilayers on BFO films with different thicknesses, we choose three samples from series A, e.g. 16 *nm*-BFO sample, 52 *nm*-BFO sample and 69 *nm*-BFO. The AFM surface morphology of 19 *nm*-BFO, 52 *nm*-BFO and 69 *nm*-BFO samples are shown in Figure 4.15 (a), (b), and (c) respectively. The surface roughness and the averaged step width can be determined from Figure 4.15 (a-c). The surface roughnesses (σ) are 126 *pm* for 19 *nm*-BFO, 244 *pm* for 52 *nm*-BFO and 575 *pm* for 69 *nm*-BFO, respectively. The relative errors of σ are taken as $\sim 10\%$. The averaged step widths (W) are estimated as 117 *nm* for 19 *nm*-BFO, 58 *nm* for 52 *nm*-BFO and 193 *nm* for 69 *nm*-BFO, respectively. The relative errors of W are also taken as $\sim 10\%$. In Figure 4.15 (d), the anisotropy fields vs BFO thickness is presented where the H_A of Pt/Co/Pt on 69 *nm*-BFO film is larger than that of Pt/Co/Pt on 52 *nm*-BFO film. Since the roughness of 52 *nm*-BFO sample (244 *pm*) is smaller than that of 69 *nm*-BFO sample (575 *pm*), this unexpected small value of H_A, and hence unexpected small value of K_u for 52 *nm*-BFO sample need to be explained.

Here, we introduce the sheet intrinsic perpendicular magnetic anisotropy $t \cdot K_u$ and re-presented the data as the $t \cdot K_u$ vs $2\sigma/W$ plot in Figure 4.15 (e). For $t \cdot K_u$, we have

$$t \cdot K_u = t \cdot K_u^0 - \alpha \frac{2\sigma}{W}, \tag{4.6}$$

where t is the thickness of Co, K_u^0 is the intrinsic perpendicular magnetic anisotropy of ideal flat surface, α is the geometric factor which depends on the actual shape of the terraces [62]. The linear relation of $t \cdot K_u$ and $2\sigma/W$ is restored in Figure 4.15 (e) and the geometric factor (α) is estimated to be ~ 2.6 which is significantly higher than the usual value as ~ 1. Considering the large error bar in $t \cdot K_u$ which is the aftermath of calculating the shape anisotropy ($\frac{1}{2}\mu_0 M_S^2$) where we use ~ 50 emu/cm^3 as the error for the saturation magnetization (M_S), this value is acceptable. What is more, the curved feature of the steps in thin film surface morphologies (Figure 4.15 a-c) and other factors such as deteriorated Pt (111) texture at the bottom Pt/Co interface for more T/R-mixing may also contribute to the seemingly large geometric factor.

4.4 Summary

Pt(t_Pt)/Co(0.7)/Pt(4) trilayers were sputtered on BFO films of various thicknesses on 16 *nm*-CCMO buffered LAO substrates. Phases and crystallinity of BFO films were examined by using X-ray diffraction, surface topography of BFO thin films were studied by using AFM. Both XRD and AFM studies showed that BFO films thinner than 25 *nm* were pure T-like phase with a step-terrace featured surface, thicker BFO films were mixed phase BFO with a shark gill featured structure embedded in the T-like matrix. Perfect squareness of AHE hysteresis loops were obtained for Pt(1.2)/Co(0.7)/Pt(4) trilayers on as-deposited BFO thin films, revealing the most optimum surface condition for integrating metal layers with PMA on BFO. PMA was achieved for Pt(t_{Pt})/Co(0.7)/Pt(4) trilayer with a Pt seed layer as thin as 0.9 nm on both pure T-like BFO and mixed phase BFO. Unlike the metal magnetic multilayers with PMA on Cr_2O_3, no obvious exchange bias fields were found for these Pt/Co/Pt trilayers with PMA on BFO. Finally, the anisotropy fields for Pt(0.9, 1.2)/Co(0.7)/Pt(4) trilayers were determined by using the AHE, we find that for both cases, Pt/Co/Pt trilayers on pure T-like phase BFO have a larger anisotropy field than Pt/Co/Pt trilayers on mixed phase BFO. The fluctuation of the anisotropic energy for Pt/Co/Pt on BFO even for the same film thickness can be explained by the roughness influence of the surface anisotropy of the Pt/Co/Pt trilayers inherited from the BFO surface morphology.

CHAPTER 5

Co/Pt multilayers on BFO without the seed Pt layer

5.1 Introduction

In chapter 4, the PMA for Pt/Co/Pt trilayer with a seed Pt layer as thin as 0.9 nm has been achieved which is still thick enough for screening the electric field from the bottom multiferroic/ferroelectric layer to influence the Co layer. To increase the couplings between the multiferroic/ferroelectric layer and the ferromagnetic layer and provide more control options for the device, one strategy is to grow the Co layer directly on top of the multiferroic/ferroelectric layer. Without the seed Pt layer, the formation of Pt (111) texture for the capping Pt layer is in doubt, even if the Pt (111) texture is survived, the magnetic anisotropy energy for the Co/Pt multilayer will be significantly reduced due to the absence of the down Pt/Co interface [60].

Several advances are made in deposition of metal magnetic multilayers with PMA on perovskite oxides. Vermeulen et al. deposit Co layer directly on isopropanol (IPO) treated $SrTiO_3$ (STO) and obtain a good PMA for Co at room temperature [58]. Lin et al. have successfully achieved PMA on CoFeB/BTO structure and found that the interfacial magnetic anisotropy energy of the CoFeB depends on the different as-grown polarizations of BTO layer[65]. Increasing the number of Co/Pt interfaces is another way to achieve PMA without using the Pt seed layer. Huang et al. have achieved the PMA for the magnetic multilayer $[Co(0.6)/Pt(0.5)]_2$ deposited directly on $Bi_{0.85}La_{0.15}FeO_3$ [66].

In this chapter, Co layers of various thicknesses, e.g. 0.7 *nm* and 0.5 *nm* are sputtered directly on pure T-like phase BFO and mixed-phase BFO films, then 4-*nm* protecting Pt layers are sputtered on top of the Co layers. Magnetic properties of the Co/Pt double-layers on BFO are examined through SQUID-VSM and AHE measurements. Finally, the $[Co(0.5)/Pt(1.2)]_4$ magnetic multilayers are deposited directly on BFO without sputtering the Pt seed layer. The PMA is achieved for this $[Co(0.5)/Pt(1.2)]_4$ structure on both pure T-like BFO and mixed-phase BFO thin films at room temperature.

5.2 Samples and Characterization

In this chapter, we prepared three sample series: (1) Co(0.7)/Pt(4) bilayers on pure T-like phase BFO and mixed-phase BFO films, (2) Co(0.5)/Pt(4) bilayers on pure T-like phase BFO and mixed-phase BFO films, (3) $[Co(0.5)/Pt(1.2)]_4/Pt(2.8)$ multilayers on pure T-like phase BFO and mixed-phase BFO films.

Using the growth condition listed in chapter 3 (Table 3.1), we grow pure T-like phase BFO and mixed-phase BFO films on 16-*nm* CCMO buffered LAO substrates. Then we transferred the as-deposited BFO films to the sputtering chamber as soon as we took them out from the PLD chamber.

Polycrystalline magnetic multilayers were sputtered on BFO films. The base pressure was better than 5.0×10^{-8} Torr. The Ar partial pressure was 2.0 mTorr for Co and 1.5 mTorr for Pt. The deposition power was 30 W for both Co and Pt. Deposition rates were determined from the growth of thick monolayers of both materials and calibrated by checking the thickness of superlattices of Co/Pt. Samples with clear XRR oscillations were also selected for fitting the thicknesses of the CCMO, BFO, Co and Pt, respectively.

5.2.1 X-ray diffraction and structural characterization

X-ray diffraction (XRD) measuremnts, e.g. grazing incidence X-ray diffraction (GIXRD), high-angle $\theta - 2\theta$ scan, low-angle X-ray reflectometry (XRR) were carried out to determine the Pt (111) texture, thickness, crystal structure and crystalline quality of the Pt/Co/BFO heterostructures by using a SmartLab X-ray Diffractometer with Cu $K_{\alpha 1}$ radiation ($\lambda = 1.5406$ Å). GIXRD is used for checking the presence of Pt (111) texture in Pt/Co/BFO heterostructures. XRR is used for determining the layer thicknesses, e.g. Pt layer, Co layer, CCMO layer and BFO layer. XRD $\theta - 2\theta$ scan is used for checking the crystal structure and crystalline quality of the epitaxial BFO/CCMO thin films on LAO substrates. Surface morphologies of the BFO thin films and Co/Pt multilayers covered BFO thin films were examined by using an Asylum Research MFP-3D-SA scanning probe microscope in AC mode at room temperature.

GIXRD measurements of BFO/Co/Pt samples

Without the seed Pt layer, texture of the capping Pt layer should be influenced by the underlying Co layer, hence the existence of Pt (111) texture at the up Co/Pt interface is questionable. To examine the Pt (111) texture, we usually use the out-of-plane XRD $\theta - 2\theta$ scan, checking for the existence of the $\sim 39.75°$ peak in 2θ. But, this method is not feasible for examining the Pt (111) texture sputtered on T-like phase BFO due to the closeness of T-BFO (002) peak ($\sim 38.76°$) and Pt (111) peak ($\sim 39.75°$) in 2θ, the weak Pt (111) peak is completely overshadowed by the strong T-BFO (002) peak as shown in Figure 5.3 (a) and 5.5 (a).

As we have demonstrated in Figure (3.5) in Chapter 3, the Pt (220) peak in grazing incidence X-ray diffraction (GIXRD) corresponds to the Pt (111) peak in out-of-plane XRD $\theta - 2\theta$ scan, we use the GIXRD method to check the Pt (111) texture in Co/Pt multilayers sputtered on BFO. The results of GIXRD with a fixed incidence angle of 0.5° for Co/Pt multilayers on CCMO buffered BFO thin films are presented in Figure (5.1). Two series of FM/BFO samples are prepared for the GIXRD scans. One sample series consists of Pt(t_{Pt})/Co(0.7)/Pt trilayers with various Pt seed layer thicknesses of 2 *nm*, 1 *nm* and 0 *nm* on pure T-like phase BFO thin films, the results are shown in Figure 5.1 (a). Another sample series consists of Co(t_{Co})/Pt bilayers with various Co thicknesses of 0.7 *nm* and 0.5 *nm* on mixed-phase and pure T-like phase BFO thin films, the results are shown in Figure 5.1 (b). In this Chapter, we will mainly study the magnetic properties of Co/Pt bilayers on mixed-phase and pure T-like phase BFO thin films.

The existence of capping Pt (111) texture for Co/Pt bilayers on both mixed-phase and pure T-like phase BFO films is proved by identifying the Pt (220) peak at $\sim$ 67.44° in GIXRD as shown in Figure 5.1 (b). The polycrystalline nature of the Co/Pt multilayers sputtered on BFO is evident since the appearance of all major fcc Pt peaks, e.g. (111), (200) and (220) in GIXRD as shown in Figure 5.1 (a) and (b). Generally speaking, the Pt (111) and (220) peaks are higher than the (200) peak, but we can't see the systematic changing trend as we vary the Pt seed layer thicknesses (Figure 5.1, a). This is in agreement with the GIXRD results from Parakkat et al.'s work [8] on Pt/Co/Pt trilayers without using Ta as the the buffer layer on SiO_2 substrate.

Parakkat et al. [8] also suggested that the Pt seed layer might adopt Volmer Weber (island-like) growth mode on SiO_2 substrate, which will lead to an incomplete coverage for Pt seed layer on SiO_2 when the Pt thicknesses are between 1-3 *nm*. Considering the atomically flat BFO surfaces as evidenced by the step-terrace featured topographies, this is not true for the Co/Pt multilayers sputtered on BFO. The Frank-van der Merwe (layer by layer) growth mode was always adopted for thin layers of Pt or Co sputtered on atomically flat BFO surface as verified by the AFM images of the Co/Pt multilayers sputtered BFO.

The AFM images of a pure T-like phase BFO thin film before and after the Pt(1.2)/Co

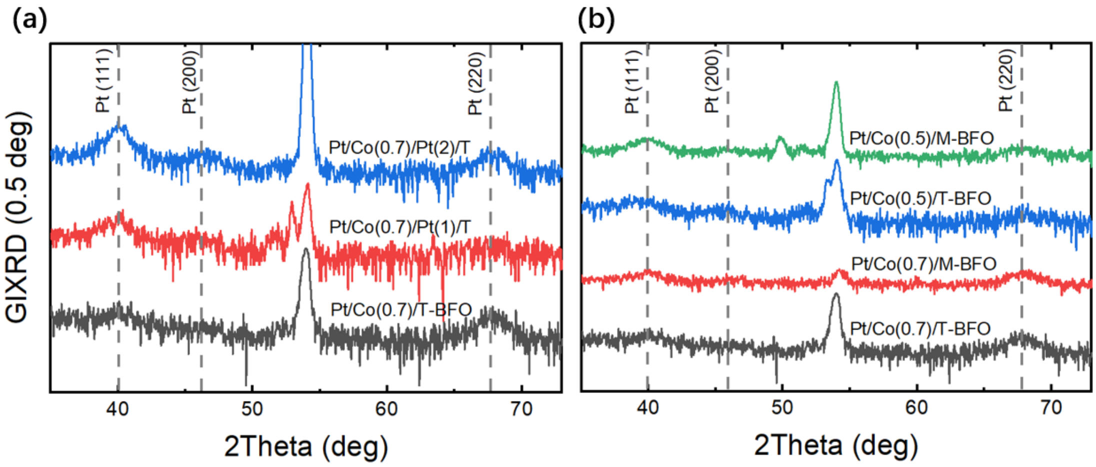

Figure 5.1: (a) GIXRD plots with a fixed incident angle of 0.5° for Pt(t)/Co(0.7)/Pt on pure T-like phase BFO with different Pt seed layer thicknesses of 2 *nm* (blue line), 1 *nm* (red line) and 0 *nm* (black line). (b) GIXRD plots with a fixed incident angle of 0.5° for Co(0.5)/Pt on mixed phase BFO (green line), Co(0.5)/Pt on pure T-like phase BFO (blue line), Co(0.7)/Pt on mixed phase BFO (red line) and Co(0.7)/Pt on pure T-like phase BFO (black line), respectively. The peak positions of fcc Pt (111), (200) and (220) are labelled as the grey dashed lines. Other peaks appeared in the figure are due to the BFO/CCMO/LAO heterostructures which are not relevant for studying the polycrystalline Pt texture.

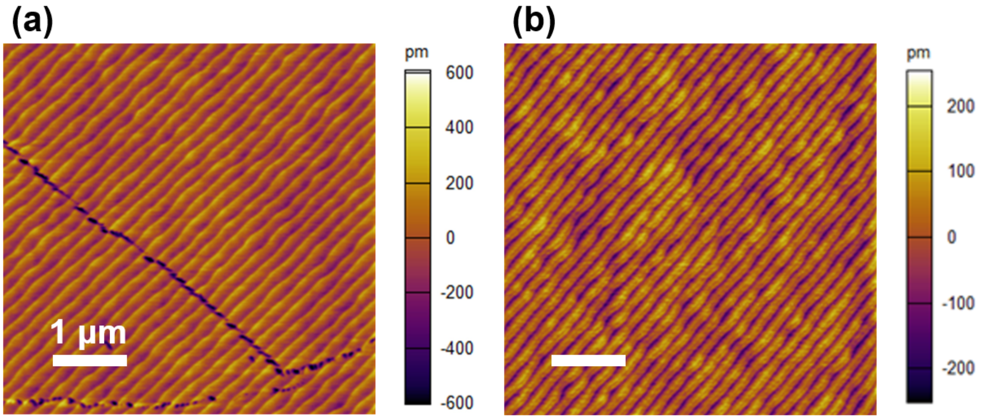

Figure 5.2: The AFM images of a pure T-like phase BFO thin film (a) before and (b) after the Pt(1.2)/Co(0.7)/Pt(4) trilayer deposition via DC sputtering.

(0.7)/Pt(4) trilayer deposition via DC sputtering are shown in Figure 5.2 (a) and (b) which show exactly the same step-terrace featured topographies and almost identical surface roughnesses. The root mean square (RMS) roughness (R_q) for uncovered BFO has a slightly larger value of $\sim$ 120 pm than the RMS roughness of $\sim$ 100 pm for Pt/Co/Pt covered BFO.

In summary, although the Co/Pt multilayers sputtered on BFO are polycrystalline by nature, the capped Pt layers at the up Co/Pt interface are significantly (111) textured as evidenced by the GIXRD of Co(t_{Co} = 0.7, 0.5)/Pt bilayers sputtered on both mixed phase BFO and pure T-like phase BFO thin films. Hence, the perpendicular magnetic anisotropies (PMA) are likely to happen in this BFO/Co(t_{Co})/Pt structure.

XRD, XRR and AFM characterizations

The XRD, XRR and AFM measurements for Co(0.7)/Pt(4) bilayers sputtered on epitaxial BFO films are presented in Figure (5.3). Figure 5.3 (a) shows $\theta - 2\theta$ x-ray diffraction (XRD) scans for BFO thin films with different thicknesses, e.g. 17 *nm* (red curve) and 45 *nm* (black curve) on CCMO buffered LAO substrates. Aside from the BFO, CCMO and LAO peaks, no impurities or secondary phases are presented in figure 5.3 (a). The thicknesses of BFO layer and CCMO layer can be estimated through the deposition rates obtained from chapter 4 and checked by XRR fittings and TEM measurements.

The thicknesses of Co and Pt layer can be estimated from the growth rate of Co and Pt and checked by XRR fittings. Surface Morphologies of the BFO/Co/Pt heterostructures are studied through AFM after sputtering of the Co/Pt bilayers, which are presented in figure 5.3 (c) and (d). Despite the Co/Pt bilayers sputtered on BFO, surface morphologies changes little compared with the un-sputtered BFO thin films. This implies layer-by-layer growth of Co/Pt being sputtered onto BFO, leading to the formation of a very flat and continuous Co/Pt bilayer.

The AFM image of the Co/Pt bilayer on the 17-*nm* BFO film in figure 5.3 (c) shows a step-and-terrace featured surface morphology with a surface roughness of only $\sim$ 110 pm which is inherited from the topography of the underlying pure T-like phase BFO film. Whereas, the AFM image of the Co/Pt bilayer on the 45-*nm* BFO film in figure 5.3 (d) shows a typical mixed phase surface morphology. It exhibits dark shark-gill featured regions embedded in the flat T-like matrix, which is determined by the

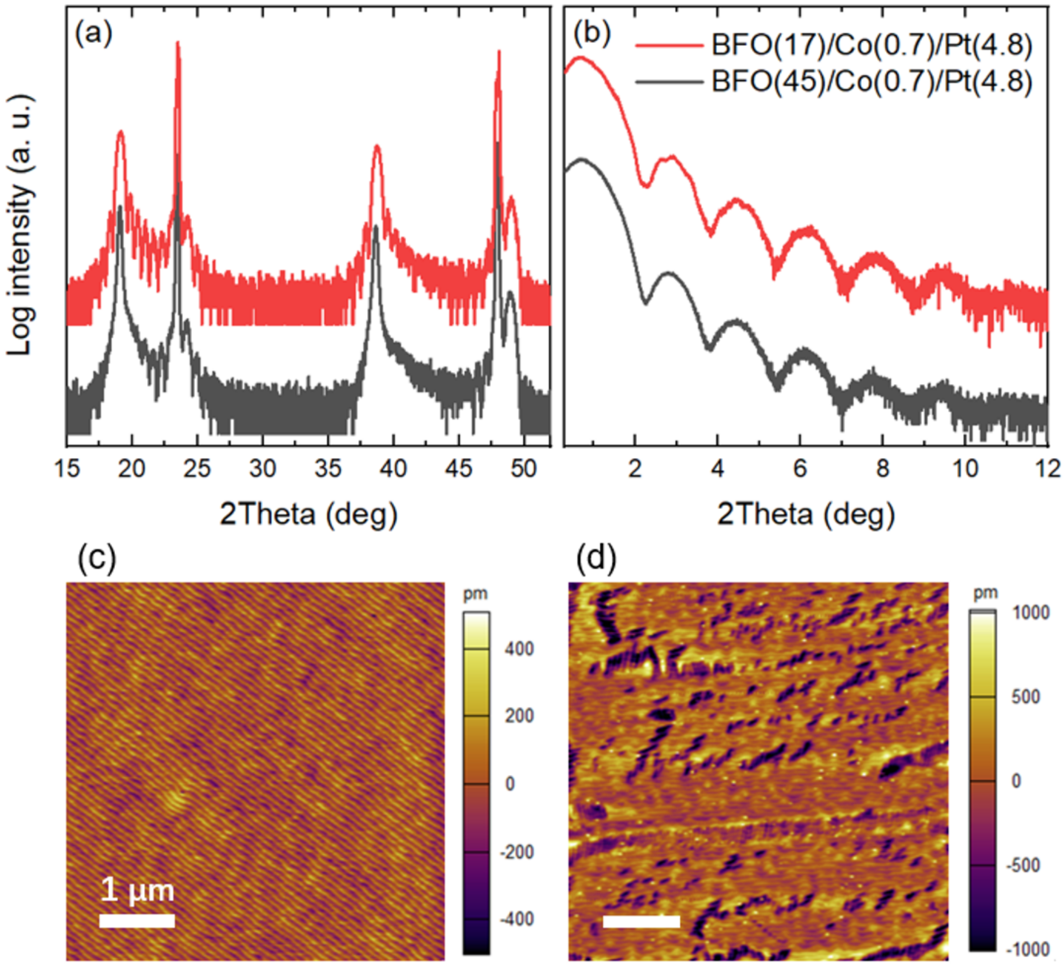

Figure 5.3: (a)XRD $\theta - 2\theta$ scans of a pure T-like phase BFO thin film (red curve) and a mixed-phase BFO thin film (black curve) on CCMO buffered LAO substrates. (b) XRR scans of Co/Pt double layers on a pure T-like phase BFO film (red curve) and a mixed-phase BFO film (black curve). Combining the growth rate estimation with the XRR fringe positions, the complete structures are determined to be BFO(17)/Co(0.7)/Pt(4.8) (red curve) and BFO(45)/Co(0.7)/Pt(4.8) (black curve), respectively. AFM images for (c) BFO(17)/Co(0.7)/Pt(4.8) and (d) BFO(45)/Co(0.7)/Pt(4.8).

underlying mixed phase BFO film. The surface roughness for Co/Pt on mixed-phase BFO is about 350 pm which is almost identical with the un-covered BFO film of similar thickness.

From figure 5.3 (b), oscillation with small periods can be seen from the XRR plot of Co/Pt bilayer on a pure T-like phase BFO thin film (red line). Hence we fit the XRR data using the GenX software [35] as shown in Figure 5.4, and the fitting parameters are listed in Table (5.1).

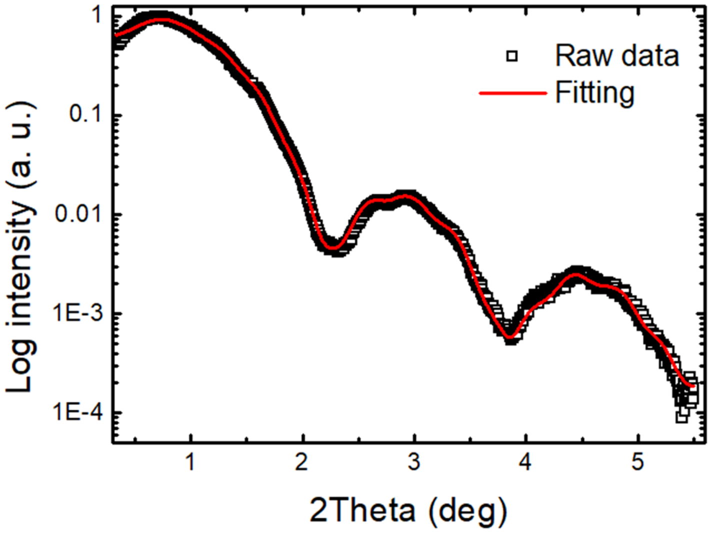

Figure 5.4: XRR scan raw data (open black square) and the fitting (red curve) for the Co/Pt bilayer on a pure T-like BFO film. The model structure used for fitting is LAO/CCMO(15.0)/BFO(17.5)/CoO(0.4)/Co(0.7)/Pt(4.7), and the fitting parameters are listed in Table (5.1).

The fitted Co(0.7)/Pt(4.7) is almost identical with the structure we calculated from the growth rates of Co and Pt which is Co(0.7)/Pt(4.8). To get the optimum fitting result, we also insert a thin layer of CoO of about 0.4 *nm* between the Co layer and the BFO layer. Since the Co atoms in adjacent to oxides are easily influenced by the nearby oxygen atoms in oxides, it is not surprising that some Co atoms at the BFO/Co interface are oxidized to form CoO.

The XRD, XRR and AFM measurements for the second sample series, Co(0.5)/Pt(4) bilayers sputtered on pure T-like phase BFO and mixed-phase BFO films are presented in Figure 5.5.

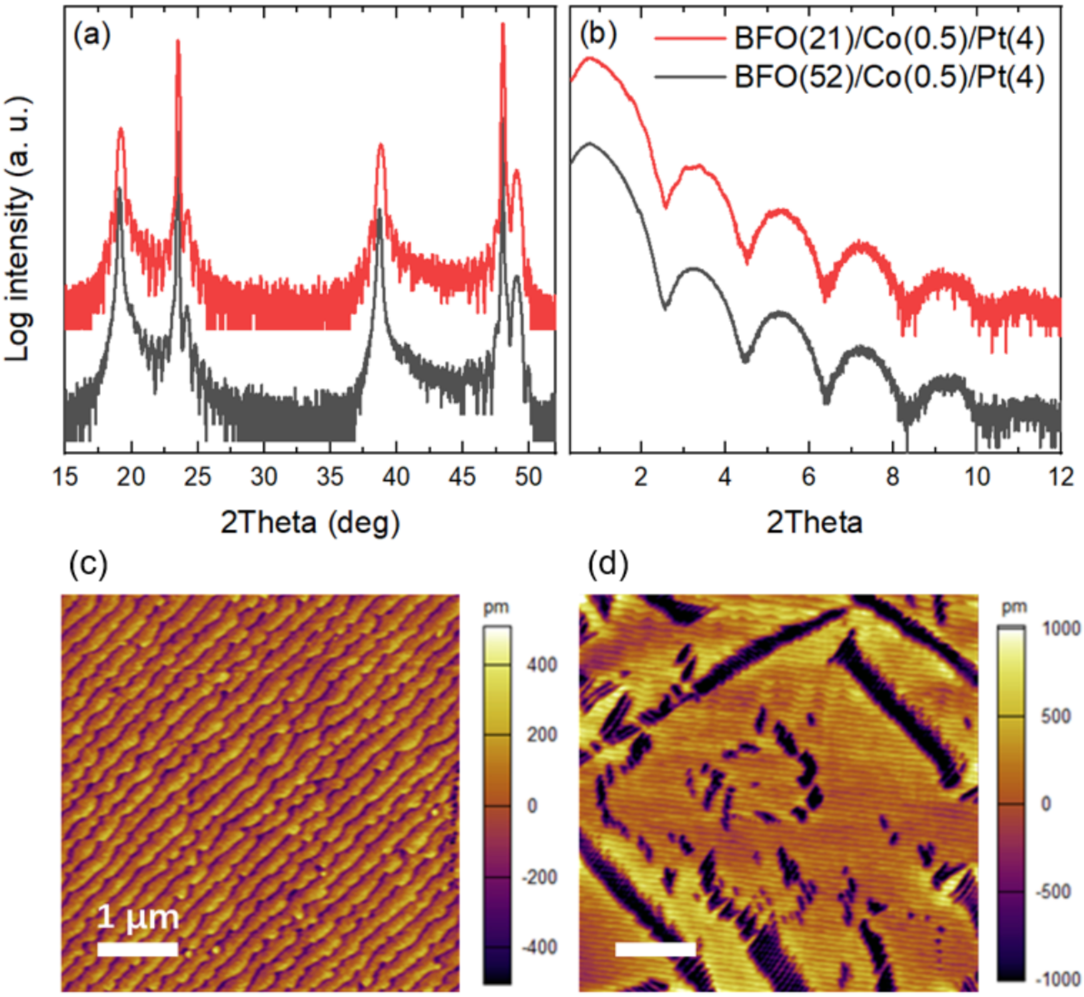

Figure 5.5: (a) XRD $\theta - 2\theta$ scans of a pure T-like phase BFO thin film (red curve) and a mixed-phase BFO thin film (black curve) on CCMO buffered LAO substrates. (b) XRR scans of Co/Pt double layers on a pure T-like phase BFO film (red curve) and a mixed-phase BFO film (black curve). Combining the growth rate estimation with the XRR fringe positions, the complete structures are determined to be BFO(21)/Co(0.5)/Pt(4.0) (red) and BFO(52)/Co(0.5)/Pt(4.0) (black curve), respectively. AFM images for (c) BFO(21)/Co(0.5)/Pt(4.0) and (d) BFO(52)/Co(0.5)/Pt(4.0).

Using the GenX software, we have fitted the XRR data of Co(0.5)/Pt on pure T-like phase BFO film which exhibits clear oscillations of small periods superimposed on oscillations with large periods (Figure 5.5, b) to determine the sample structure. The optimum fitting is presented in figure 5.6, and the fitting parameters are listed in Table (5.1).

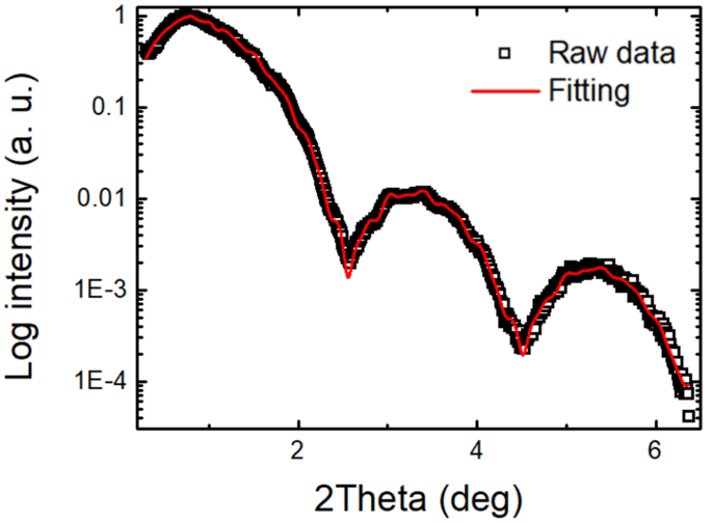

Figure 5.6: XRR scan raw data (open black square) and the fitting (red curve) for the Co/Pt bilayer on a pure T-like BFO film. The model structure used for fitting is Pt(4.0)/Co(0.4)/CoO(0.3)/BFO(21.5)/CCMO(17.4)/LAO, and the fitting parameters are listed in Table (5.1).

The fitted Co(0.45)/Pt(4.0) structure is very close to the planned structure of Co(0.5)/Pt(4), indicating the high accuracy of the growth rates we estimated for Co and Pt. Similar to the Co(0.7)/Pt sample series, a thin CoO layer of thickness ~ 0.3 *nm* is required to achieve the optimum fitting.

5.2.2 XAS measurements

X-ray photoelectron spectroscopy (XPS) and X-ray absorption spectroscopy (XAS) are usually used for studying the formation of CoO at the Co/oxide interface [67]. XPS studies on Co/Pt bilayers on $SrTiO_3$ thin films[58] suggest the existence of a thin CoO layer between the Co and the $SrTiO_3$. It is also reported that the oxygen atoms can diffuse from $CaTiO_3$ (CTO) layer to the adjacent Co layer at the CTO/Co interface,

Parameter	Co(7 Å)/BFO	Co(5 Å)/BFO
σ_{LAO} (Å)	2 ± 2	3 ± 2
d_{CCMO} (Å)	150 ± 2	174 ± 2
σ_{CCMO} (Å)	2 ± 2	3 ± 1
d_{BFO} (Å)	175 ± 2	215 ± 1
σ_{BFO} (Å)	2 ± 2	2 ± 2
d_{CoO} (Å)	4 ± 1	3 ± 1
σ_{CoO} (Å)	2 ± 2	1 ± 1
d_{Co} (Å)	7 ± 1	4 ± 1
σ_{Co} (Å)	3 ± 1	3 ± 1
d_{Pt} (Å)	47 ± 1	40 ± 1
σ_{Pt} (Å)	1 ± 1	1 ± 1

Table 5.1: Results of fitting XRR data of BFO/Co(t)/Pt samples in Figure (5.4) and Figure (5.6), where d represents the thickness of each layer and σ represents the roughness of each layer.

leading to the formation of CoO[68]. In addition, the formation of CoO layer at the Co/oxides interface is responsible for the enhanced perpendicular magnetic anisotropy [58, 68].

XAS is usually used for studying the oxidation state of Co thin film, it gives information on the chemical composition averaged over the Co layer. Using XAS, Manchon et al. [67] have revealed the presence of CoO at the AlO$_x$/Co interface of AlO$_x$/Co/Pt trilayers and established the corresponding relation with the maximum of PMA and the appearance of Co-O bondings at the AlO$_x$/Co interface. Bi et al. [69] have also demonstrated the existence of CoO at the Gd_2O_3/Co interface of Gd_2O_3/Co/Pt trilayers. What is more, the Co oxidation state at the Gd_2O_3/Co interface can be controlled reversibly by applying a voltage across the Gd_2O_3 layer.

To study the the oxidation state of Co at the BFO/Co interface, we performed the XAS measurements for Co(1)/Pt(4) bilayers sputtered on pure T-like phase and mixed-phase BFO thin films

The Co L_3 edge absorption peaks of the Co(1)/Pt(4) bilayers on both pure T-like phase BFO (red curve) and mixed-phase BFO films (black curve) are presented in

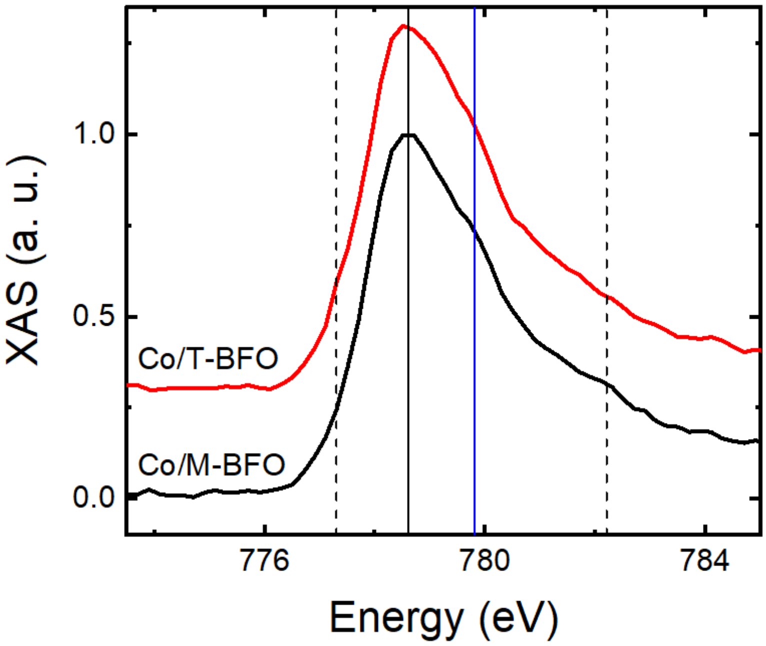

Figure 5.7: Normalized XAS spectra at the Co L_3 edge showing the oxidation state of ultra thin Co films on pure T-like BFO and mixed-phase BFO films.

Figure 5.7. In addition to the main Co peak at 778.6 eV (vertical black line), a shoulder is clearly seen at 779.8 eV (vertical blue line), indicating the existence of CoO at the BFO/Co interface which expects to induce a PMA [67]. Two other peaks at 777.3 and 782.2 eV (vertical dashed lines), characteristic of CoO are also identified in Figure 5.7. Overall speaking, there are no significant differences between the XAS spectra of Co on pure T-like phase BFO and mixed-phase BFO films.

5.3 Magnetic characterization

Anomalous hall effect (AHE) magnetometry and Superconducting quantum interference vibrating sample magnometer (SQUID-VSM) are employed to study the magnetic properties of Co/Pt multilayers on BFO thin films (shortened as FM/BFO heterostructures).

The SQUID-VSM is an accurate method for measuring the magnetic moments of both the film and the substrate as a whole. So we need to deduct the contribution from the substrate to get the correct magnetic moment for the thin film. As a comparison, although we cannot get the moment value from the AHE measurement directly, it is a clean and elegant method for studying the magnetization in magnetic metal layer. When the magnetic field is applied perpendicular to the film, the AHE resistance R_H is proportional to the out-of-plane magnetization M_z in metal [36], the shape of the R vs H hysteresis loop exactly represents the shape of the M vs H hysteresis loop of magnetic metal layer, the clumsy deducting procedure is unnecessary in AHE. Using AHE, we can readily measure the coercive field, the anisotropy field and even DMI field.

5.3.1 Magnetic Properties of Co(0.7 nm)/Pt(4 nm) double layers on BFO

Weak PMA of Pt/Co/BFO at room temperature

The normalized $M-H$ hysteresis curves for Co(0.7)/Pt bilayer on pure T-like phase BFO thin films measured both in out-of-plane direction and in-plane direction via SQUID-VSM at room temperature are shown in Figure 5.8 (a). As a comparison, the $M-H$ hysteresis curves for out-of-plane and in-plane magnetized Pt(0.6)/Co(0.7)/Pt trilayer on pure T-like phase BFO thin films are also presented in Figure 5.8 (b).

Both samples have weak perpendicular magnetic anisotropies (PMA) due to the absence of the squareness of the hysteresis curves and larger in-plane anisotropy fields than the out-of-plane anisotropy fields. The effective magnetic anisotropy energy K_{eff} for both samples can be estimated from the area between the in-plane and perpendicular magnetization curves [70]. Using the in-plane and out-of-plane measured $M-H$ curves of both samples, the effective magnetic anisotropy energies K_{eff} are estimated to be $\sim$ 37 kJ/m^3 for Pt/Co(0.7)/BFO and $\sim$ 19 kJ/m^3 for Pt/Co(0.7)/Pt(0.6)/BFO, respectively. The K_{eff} enhancement of $\sim$ 18 kJ/m^3 is small as compared with the typical K_{eff} values of $\sim$ 200 kJ/m^3 we have obtained for Pt/Co/Pt/BFO samples in Chapter 4. As both samples have the same Co(0.7)/Pt up interfaces, the K_{eff} enhancement of Pt/Co(0.7)/BFO sample should attribute to the BFO/Co(0.7) down interface. The interfacial anisotropy of BFO/Co should be influenced by the oxidation state of Co at the interface according to Manchon et al. [67]

What is more, the magnetic dead layer t_{MDL} is usually studied through the $M_S\cdot$ V vs t_{Co} plot, the nominal t_{MDL} is estimated to be ~ 2.2Å from Figure (5.9), which corresponds to $\sim$ 1 ML of Co fcc (111) (~ 2.05Å). It should be noted that the true t_{MDL} is

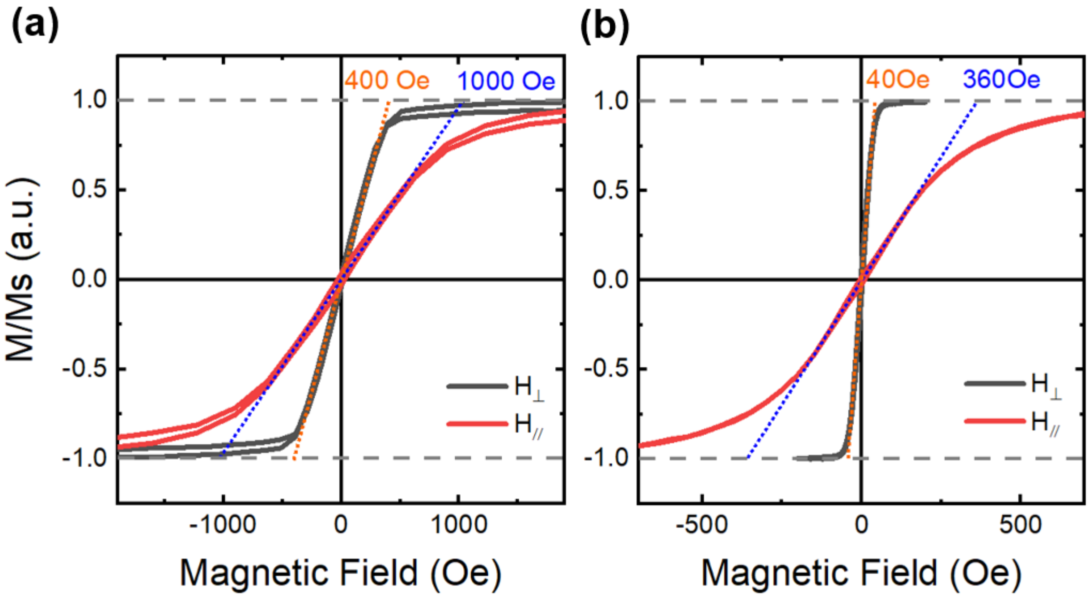

Figure 5.8: Normalized M vs H hysteresis curves for (a) Co(0.7)/Pt bilayer and (b) Pt(0.6)/Co(0.7)/Pt trilayer on pure T-like phase BFO thin films at room temperature.

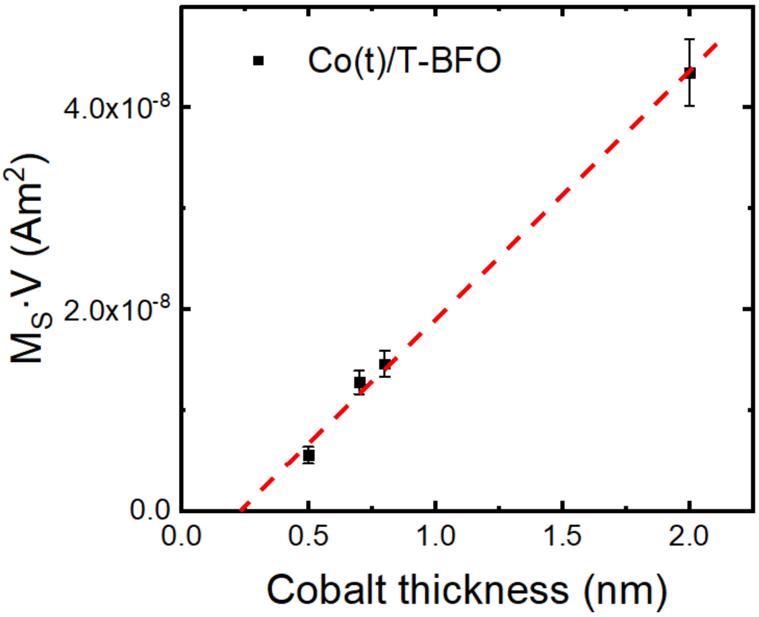

Figure 5.9: The magnetic moment $M_S \cdot V$ vs cobalt thickness t plot for 5×3 mm^2 Co(t)/BFO samples. A linear fit towards zero magnetic moment allows to determine the nominal t_{MDL}.

difficult to infer from the $M_S \cdot V$ vs t_{Co} plot due to the additional magnetization of the Co/Pt interface and the large errors in determining the area of each sample. Considering the difficulty of determine t_{MDL}, we didn't use the reduced volume for calculating the saturation magnetization M_S to make the data processing more consistently.

In chapter 4, we have demonstrated that the Bulk BFO on CCMO buffered LAO substrate has a downward polarization (polarization point towards the substrate) through PFM, and the downward polarization could raise the density of oxygen vacancies and suppress the Co oxidation at the interface according to Zhang et al. [49]

Temperature dependence of AHE hysteresis loops

Temperature dependences of out-of-plane (OOP) magnetic hysteresis loops are measured through the anomalous Hall effect (AHE) method for Co(0.7)/Pt bilayers sputtered on both pure T-like phase BFO and mixed-phase BFO thin films as shown in Figure 5.10 (a).

The MH hysteresis loop at fixed temperature is already hard to explain, needless to say the temperature dependence of MH hysteresis loop, it contains several competing energies, e.g. the exchange stiffness, the magnetic anisotropy energy (MAE), Zeeman energy, the thermal fluctuation energy and the pinning energy barrier et al.

Behaviours of temperature dependence of AHE measured MH hysteresis loops in Figure 5.10 (a) can be described as three temperature regions.

(1) At low temperature (below 100 K), Co(0.7)/Pt bilayers on both pure T-like phase and mixed-phase BFO films have rectangular shaped hysteresis loops with enhanced coercive fields H_c as lowering the temperature. Since the domain walls are mostly pinned at low temperature due to the small thermal fluctuation (kT), Co(0.7)/Pt bilayer on mixed-phase BFO thin film has a larger coercive field (H_c) due to the presence of more pinning sites [71] influenced by the T/R-mixing region at the BFO/Co interface. Strong pinning arises when the defects (pinning sites) have a dimension comparable to the domain wall width δ_{DW}, and planar defects are the most effective pinning sites than line and point defects for the whole wall finds itself with a more favorable energy when it fits the defect [72]. According to Moreno et al. [73], the typical domain wall width for Co is estimated to be $\sim 20 - 30\ nm$ which exactly matches the width of R-like stripe $\sim 30\ nm$ [23, 74] on mixed-phase BFO film surface.

(2) Wasp-waisted hysteresis loops were observed for both samples at the medium

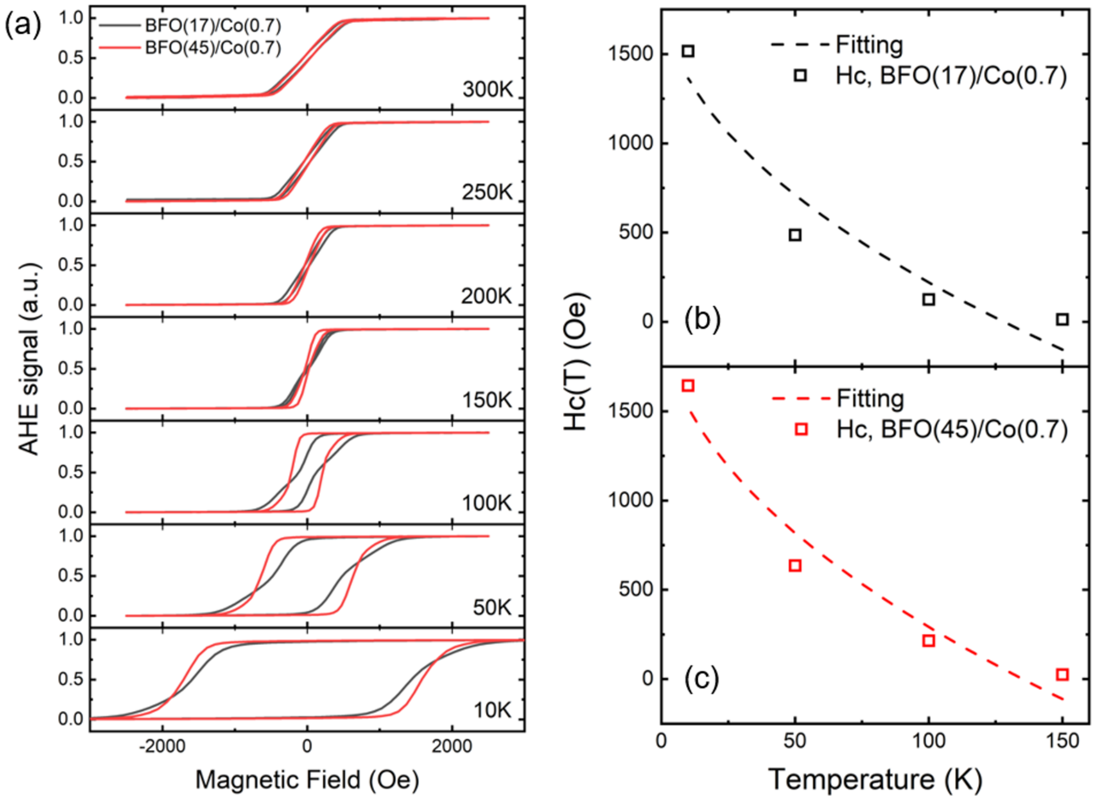

Figure 5.10: (a) Temperature dependent AHE signals for Co(0.7)/Pt(4.8) on a pure T-like phase BFO film (black curves) and a mixed-phase BFO film (red curves). Dependence of H_c on temperature for Co(0.7)/Pt(4.8) on (b) a pure T-like phase BFO film and (c) a mixed-phase BFO film.

temperature range between 100K-150K.

The wasp-waist shaped hysteresis loops are usually explained as the presence of multiple (at least two) grains with different coercive fields H_c [75]. Sample regions with large H_c were populated by pinned domain walls, while the regions with small H_c were populated by unpinned domain walls. The pinned domain walls populated region has a more rectangular shaped hysteresis loop, and the unpinned domain walls populated region has a slanted shape hysteresis loop with a small out-of-plane anisotropy field H_A, characteristic of weak PMA.

Mixture of these two regions renders the wasp-waisted hysteresis loop. Since Co(0.7)/Pt bilayer on pure T-like phase BFO has larger proportion of unpinned domain walls, it has a more narrowed wasp-waist for the hysteresis loop.

(3) Finally, for the high temperature region ($>$ 150 K), most domain walls are unpinned due to the elevated thermal fluctuation energy k_BT, slanted hysteresis loops determined by small MAE K_{eff} are observed for this temperature region.

It should be noted that the results of Co/Pt bilayers sputtered on BFO thin films we described here are in contrary to the results of Pt/Co/Pt trilayers sputtered on BFO (Chapter 4), Pt/Co/Pt trilayers sputtered on pure T-like phase BFO usually have a larger MAE K_{eff} than Pt/Co/Pt trilayers on mixed-phase BFO due to the smaller roughness induced K_{eff} reduction.

Temperature dependences of coercivity fields (H_c) for Co(0.7)/Pt bilayers sputtered on both pure T-like phase BFO film (black) and mixed-phase BFO film (red) are presented in Figure 5.10 (b) and (c), respectively. Unlike the superparamagnetic Co nanoparticles, coercivity fields (H_c) of the Co(0.7)/Pt bilayers on BFO only roughly following $H_c(T) = H_c(0) \times \left(1 - (T/T_B)^{1/2}\right)$, which is consistent with the results of CoFeB(1) sputtered on R-like phase BFO film [76].

5.3.2 Magnetic Properties of Co(0.5 nm)/Pt(4 nm) double layers on BFO

To study the MAE K_{eff} quantitively, we need to determine the anisotropy field H_A precisely using the AHE measurements. The not ideally rectangular shaped hysteresis loops (Figure 5.10 a) of Co(0.7)/Pt bilayers sputtered on BFO thin films hindered us from calculating the anisotropy field H_A via AHE measurements. The Co(0.5)/Pt bilayers sputtered on BFO thin films with improved squareness of hysteresis loops are used for studying the anisotropy fields H_{A}, and hence K_{eff}.

Curie temperature T_c of Co(0.5)/Pt bilayer on BFO

Aside from the enhancement of MAE K_{eff}, Curie temperature T_c also expects to be reduced due to the decrease of the ferromagnetic Co thickness from 0.7 Å to 0.5 Å [8, 60]. Compared with the Pt(1.2)/Co(0.5)/Pt trilayer on BFO, Co(0.5)/Pt bilayer on BFO also expects to reduce its Curie temperature, because the seed Pt layer adjacent to Co also magnetized [8, 60, 61] and increase the effective Co thickness due to the magnetic proximity effect in Pt.

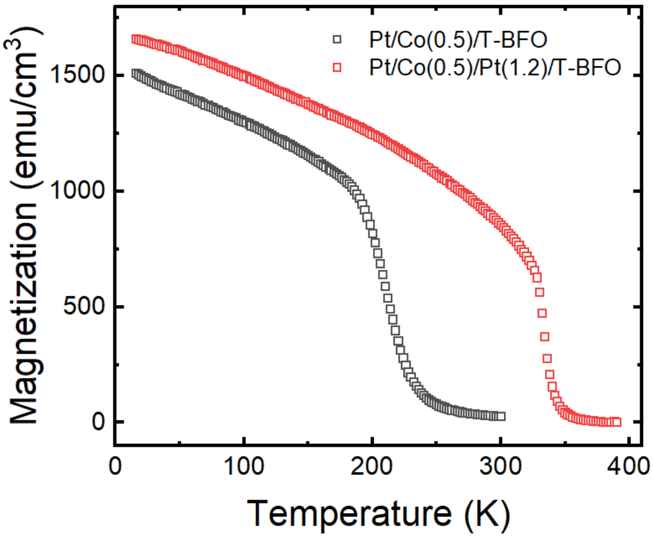

Figure 5.11: Temperature dependence field cooled (FC) out-of-plane magnetized magnetization M measured at 50Oe for (a) Co(0.5)/Pt(4) bilayer (black curve) and (b) Pt(1.2)/Co(0.5)/Pt(4) trilayer (red curve) on pure T-like phase BFO films.

Figure (5.11) shows the field cooled (FC) M vs T curves for Co(0.5)/Pt bilayer (black curve) and Pt(1.2)Co(0.5)/Pt trilayer (red curve) on pure T-like BFO thin films. The T_c is reduced from $\sim$ 340 K (above room temperature) for Pt(1.2)/Co(0.5)/Pt trilayer to $\sim 236K$ for Co(0.5)/Pt bilayer on BFO. What is more, the saturation magnetization M_S is also reduced from $\sim$ 1660 emu/cm^3 (Pt/Co/Pt/BFO) to $\sim$ 1500 emu/cm^3 (Pt/Co/BFO), the decrease in M_S is also explained by the magnetic proximity effect in Pt. In addition, the Co atoms in contact with BFO surface are oxidized on a certain level, this oxidation of Co will also reduce the effective Co thickness, hence reduce the T_c and magnetization.

Temperature dependence of MH curves measured by AHE method

Figure (5.12) shows temperature dependence of $M - H$ curves measured by AHE method for Co(0.5)/Pt bilayers sputtered on pure T-like phase and mixed-phase BFO thin films.

0.5-nm Co consists of only 2 ML of cobalt atoms, it approaches the 2D limit in some sense. Mermin-Wagner theorem has suggested that there is no long range magnetic order at finite temperature ($M \rightarrow 0$ for all $T > 0$) for an ideal 2D magnetic material [77]. In our Pt/Co(0.5)/BFO system, the 0.5-nm Co layer not only consists 2 layers of Co, but also coupled with the adjacent magnetized Pt atoms due to the magnetic proximity effect. Overall, the Co(0.5)/Pt bilayer on BFO has a curie temperature of $T_c \sim 200K$ as evidenced by series of temperature dependent $M - H$ hysteresis loops 5.12. This T_c ($\sim$ 200 K) is also consistent with the T_c ($\sim 236K$) as derived from the field cooled (FC) MT curve in Figure 5.11.

It is evident that for $T > T_c$, the Co(0.5)/Pt bilayers on BFO are paramagnets, Figure 5.12 (a) shows that the magnetization is not saturated even at a high magnetic field of 10000 Oe for $T = 300\ K$. When $T < T_c$, the Pt/Co(0.5) bilayers on BFO are perpendicularly magnetized and the $M - H$ hysteresis loops exhibit perfect squareness as shown in Figure (5.12). What is more, the Co(0.5)/Pt bilayer on mixed phase BFO also has a more rectangular shaped hysteresis loop and larger coercive field H_c than the Co(0.5)/Pt on pure T-like phase BFO, indicating a larger MAE K_{eff} for Co(0.5)/Pt on mixed-phase BFO film.

There are multiple factors that can influence the MAE K_{eff}, the mixed phase BFO film we studied in this Chapter has a larger $\frac{2\sigma}{W}$ value than the pure T-like phase BFO film as evidenced from Figure 5.5 (c) and (d), which means that the decrease in K_{eff} for Co(0.5)/Pt on mixed phase BFO film is larger than the decrease for Co(0.5)/Pt on pure T-like phase BFO film. The enhancement of K_{eff} for Co(0.5)/Pt on mixed-phase BFO should due to the different influence of the mixed phase BFO and pure T-like phase BFO on the adjacent Co layer.

It is possible that the Co oxidation state at the Co/BFO interface is influenced by the underlying BFO layer. From Figure (5.7), we can see that there is a slightly stronger CoO shoulder 779.8 eV (vertical blue line) for Co on mixed phase BFO (black

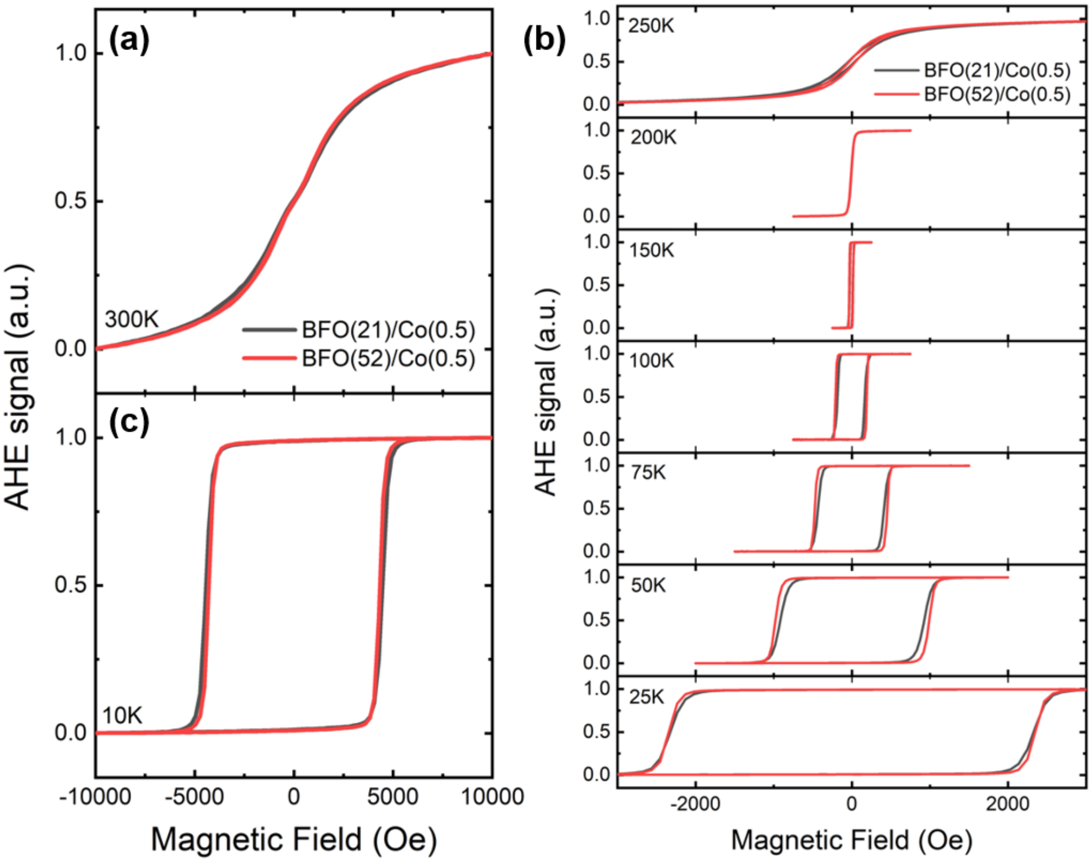

Figure 5.12: Temperature dependent AHE signals for Co(0.5)/Pt(4) on a pure T-like phase BFO film (black curves) and a mixed phase BFO film (red curves).

curve), indicating that Co at the Co/M-BFO interface is more oxidized. But this conclusion is not decisive, because the Co on pure T-like phase BFO (red curve) has a more prominent CoO shoulder at 777.3 eV (vertical dashed line).

Strengthened surface magnetism of mixed-phase BFO may also influence the adjacent Co at the Co/BFO interface[56, 74]. The T-like phase BFO is antiferromagnetic with iron magnetic moments aligned antiparallel with each other within the film surface [55]. The R-like BFO itself has weak ferromagnetism due to the canting of the neighboring antiparallel iron magnetic moments [78]. This weak ferromagnetism can be strengthened in mixed-phase BFO, forming detectable magnetic domains in the distorted monoclinic R-like BFO phases surrounded by the T-R phase boundaries [56]. The spontaneous magnetic moments are identified in the R-like BFO stripes of the mixed-phase BFO by XMCD-PEEM measurements and they are parallel to the long axis of the R-like BFO stripes [74].

Both strengthened Co oxidation state and enhanced surface magnetism of mixed phase BFO can contribute to the increased MAE K_{eff} of Co(0.5)/Pt bilayer sputtered on mixed-phase BFO films, further experimental and theoretical works are needed to understand the phenomena described here.

Anisotropy measurements

Since Co(0.5)/Pt bilayers on BFO films have perfect rectangular shaped hysteresis loops, we perform AHE measurements with the planar geometry [79] to decide the anisotropy fields H_A and study the temperature dependence of intrinsic anisotropy constants $K_u(T)$ for thin Co layer sputtered on BFO.

Callen and Callen [80] has predicted that anisotropy $K_u(T)$ will decrease as a power of the reduced magnetization $m(T) = M_S(T)/M_S(0)$, where $M_S(0)$ is the saturation magnetization at 0K. Specifically,

$$K_u(T)/K_u(0) \propto \left(M_S(T)/M_S(0)\right)^n, \tag{5.1}$$

where $n = l(l+1)/2$, l is the order of the anisotropy which is defined in angular dependence of uniaxial anisotropy energy $E_A(\theta)$ expanded as powers of $\sin\theta$

$$E_A(\theta) = K_1 \sin^2\theta + K_2 \sin^4\theta + K_3 \sin^6\theta + ..., \tag{5.2}$$

with $l = 2, 4, 6...$, where θ is the angle between the magnetization direction and the film normal. So for uniaxial anisotropy ($l = 2$), $K_u(T) \propto m(T)^3$, this $n = 3$ scaling law corresponds to the single-ion anisotropy [81].

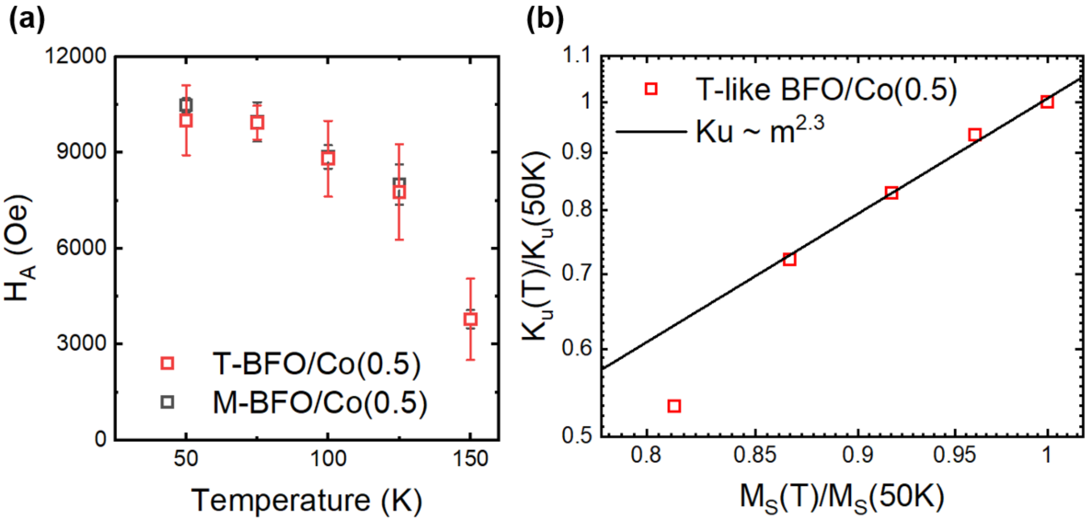

Figure 5.13: (a) Temperature dependence of anisotropy fields (H_A) for Co(0.5)/Pt bilayers sputtered on pure T-like phase BFO film (red) and mixed phase BFO film (black), respectively. (b) Log-log plot of the $K_u(T)/K_u(50K)$ vs $M_S(T)/M_S(50K)$ for Co(0.5)/Pt(4) bilayer sputtered on T-like BFO.

Figure (5.13) presents the coercive fields H_A for Co(0.5)/Pt bilayers on pure T-like phase BFO (red) film and mixed phase BFO film (black) by AHE measurements between 50 - 150 K, respectively. In addition, the Co(0.5)/Pt bilayer on mixed phase BFO film has a slightly higher H_A than the Co(0.5)/Pt bilayer on pure T-like phase BFO film.

Using $K_{eff}(T) = \frac{\mu_0}{2} M_S(T) H_\mathrm{A}(T)$, the temperature dependences of $K_{eff}(T)$ are derived from M_S(T) values of the $M - T$ curve presented in Figure 5.11 (a) and $H_\mathrm{A}(T)$ values in Figure 5.13 (a). The intrinsic perpendicular magnetic anisotropies $K_\mathrm{u}(T)$ are then calculated through $K_\mathrm{u}(T) = K_\mathrm{eff}(T) + \frac{\mu_0}{2} M_\mathrm{S}^2(T)$.

To fit the $K_u(T)$ with the Callen-Callen law (Eq. 5.1), we choose the lowest measurement temperature 50 K as the normalizing temperature T^* and make a log-log plot for $K_u(T)/K_u(T^*)$ vs $M_S(T)/M_S(T^*)$. Except the data point measured at 150 K which is close to the Curie temperature (T_c), other data points fit well with the power-law exponent $n \sim 2.3$. Since the power-law fitting $K_u(T)/K_u(50K) \propto m^n$ with a constant exponent n only works well for low temperature [82], removal of the 150 K data point is reasonable. The power law exponent $n = 2.3$ we fitted in Figure 5.13 (b) deviates from the $n = 3$ scaling law significantly.

The power-law exponent n in formula (5.1) is known to depend on the physical mechanism causing the magnetic anisotropy, n is equal to 3 for materials with a uniaxial single-ion anisotropy, and $n = 2$ for materials with a dominant two-ion anisotropy [83, 84] on the basis of a mean-field approach.

An anisotropic Heisenberg model with a single-ion anisotropy term [82, 84] is usually used for describing the ferromagnetic systems with both two-ion anisotropy and single-ion anisotropy

$$H = -\sum_{i<j} J_{ij}\mathbf{S}_i \cdot \mathbf{S}_j - \sum_{i<j} K_{ij} S_i^z \cdot S_j^z - \sum_i K_i (S_i^z)^2, \tag{5.3}$$

where $\mathbf{S}_i$ is the spin operator at lattice site i, J_{ij} is the isotropic exchange interaction constant, K_{ij} is the two-ion anisotropy constant, and K_i is the single-ion anisotropy constant. Treating the Hamiltonian (5.3) classically with precise atomistic computer simulations and Green's function theory, Evans et al. [82] get the power-law exponent $n \sim 2.246$ for pure two-ion anisotropy with fcc lattices in contrast to the mean-field value of $n = 2.0$ [80].

As a comparison, we also present the Callen-Callen plot for Pt(0.9)/Co(0.7)/Pt(4) on pure T-like phase BFO film. Figure 5.14 (a) shows the anisotropy fields H_A measured by AHE method [79] for Pt(0.9)/Co(0.7)/Pt(4) trilayers on both mixed phase BFO (black) and pure T-like phase BFO (red). In contrary to the results for Co(0.5)/Pt(4) bilayer on BFO, H_A for Pt/Co/Pt trilayer on pure T-like phase BFO is larger than that of the Pt/Co/Pt on mixed-phase BFO. With a 0.9-nm Pt seed layer inserted between Co and BFO, the Pt/Co/Pt trilayers are influenced mainly by the surface morphologies of the underlying BFO surface, since the sputtered metal layers adopted the morphologies of the covered BFO as shown in Figure (5.2).

Using the temperature dependence H_A data in Figure 5.14 (a) and the field cooled (FC) M vs T data measured by SQUID-VSM in Figure 5.14 (c) for Pt(0.9)/Co(0.7)/Pt trilayer on pure T-like phase BFO, the intrinsic anisotropies $K_u(T)$ are obtained. Choosing the lowest measurement temperature 10 K as the normalizing temperature (T^*), we then fit the data with the Callen-Callen law (5.1). The power law exponent

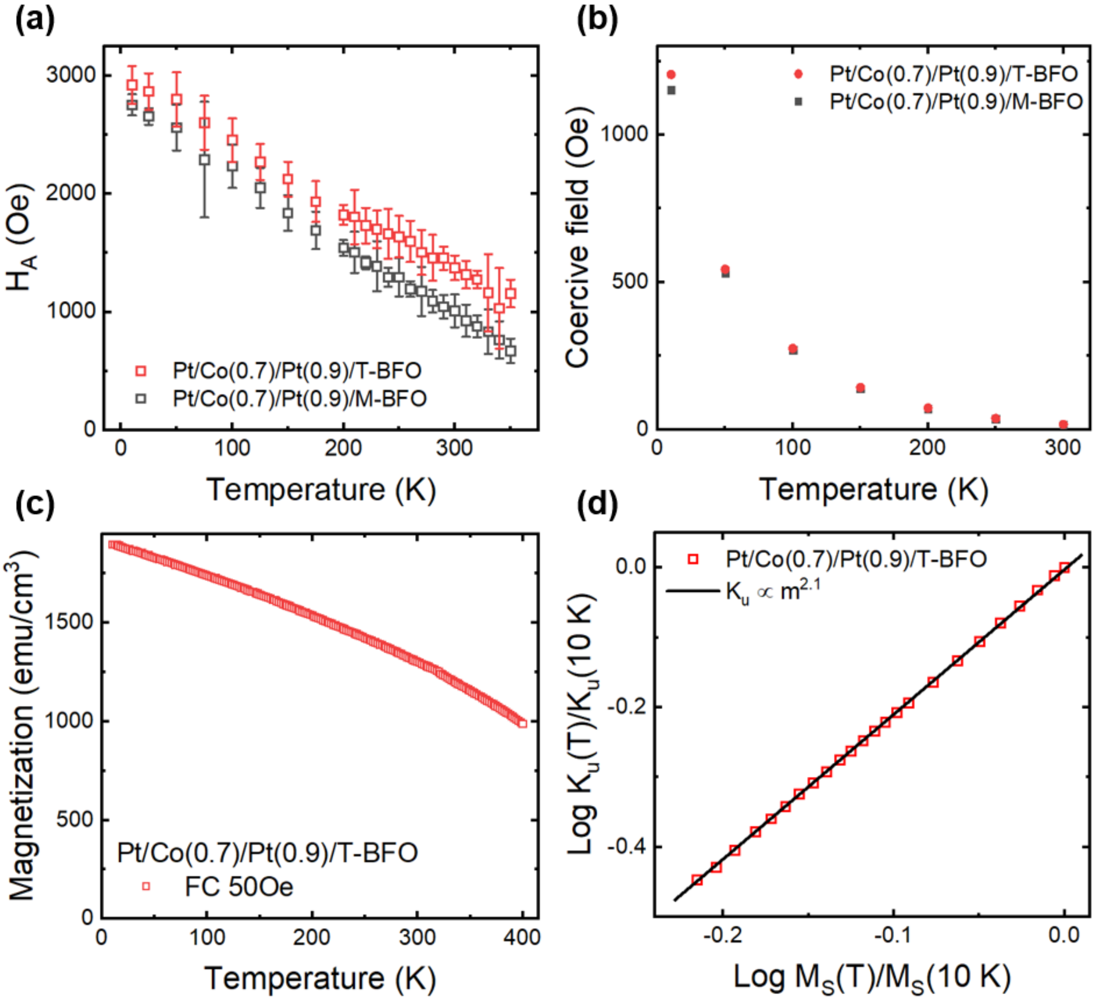

Figure 5.14: (a) Temperature dependences of anisotropy fields H_A for Pt(0.9)/Co(0.7)/Pt(4) on pure T-like phase BFO film (red) and mixed-phase BFO film (black), respectively. (b) Coercive fields H_c for Pt(0.9)/Co(0.7)/Pt(4) on pure T-like phase BFO film (red) and mixed phase BFO film (black), respectively. (c) Field cooled (FC) magnetization (M) vs Temperature (T) curve for Pt(0.9)/Co(0.7)/Pt(4) on pure T-like phase BFO film. (d) Log-log plot of the $K_u(T)/K_u(10K)$ vs $M_S(T)/M_S(10K)$ for Pt(0.9)/Co(0.7)/Pt(4) trilayer sputtered on T-like BFO.

n for Pt(0.9)/Co(0.7)/Pt trilayer sputtered on pure T-like phase BFO is fitted to be ~ 2.1 as shown in Figure 5.14 (d) which also deviates from the $n = 3$ scaling law.

Scaling exponents of $n \sim 2$ have been experimentally reported in $L1_0$ FePt alloys ($n = 2.1$) [85], $L1_0$ PtCo alloys (n=2.1) [83], CoFeB/MgO thin films ($n = 2.2$) [86], Pt/Co/Cu thin films [87] ($n = 2.1$) and most recently Pt/Co(Fe)B/Ir thin films ($n = 1.88 - 2.09$ for the different thin films) [59]. Our results on BFO/Co(0.5)/Pt(4) thin film ($n = 2.3$) and BFO/Pt(0.9)/Co(0.7)/Pt(4) thin film ($n = 2.1$) are also belonged to this category. Emergence of this $n \sim 2$ scaling is usually attributed to the dominance of the two-ion anisotropy at the interfaces [83] and the deviation from the $n \sim 2$ law signifies the departure from the mean-field theory of the two dimensional magnetic systems.

Exchange stiffness measurements

Exchange stiffness A_{ex} is an important parameter for determining domain wall width ($\delta_{DW} = \sqrt{\frac{A_{ex}}{K_{eff}}}$), domain wall energy density ($\sigma_{DW} = 4\sqrt{A_{ex}K_{eff}}$) and DMI constant ($D = \mu_0 M_S \delta_{DW} H_{DMI}$) et al. Most used method for estimating A_{ex} is to fit the temperature dependences of saturation magnetization $M_S(T)$ by the Bloch $T^{3/2}$ law (Eq. 2.24) in Chapter 2.

The dimensionality of magnetic systems is encoded in η value of Eq. (2.24) which came from a k-space integration, i.e.

$$\frac{M(T)}{M(0)} = 1 - \eta\sqrt{QS}\left(\frac{k_B T}{2A_{ex}a}\right)^{3/2}.$$

For 3D bulk magnetic systems [30], $\eta = 0.0587$, Q is the number of lattice points per unit cell (here we use $Q = 4$ for fcc lattice), $S = \frac{M(0)a^3}{Qg\mu_B}$ is the spin quantum number, a is the lattice constant (here we use $a = 3.54$Å for fcc Co) [88].

If we choose the 3D η value (0.0587) to fit A_{ex} of an ultra-thin Co film, it will lead to underestimated A_{ex} values. We get $A_{ex} = 3.3$ pJ/m for Pt(0.9)/Co(0.7)/Pt trilayer on pure T-like phase BFO film and $A_{ex} = 2.0$ pJ/m for Co(0.5)/Pt bilayer on pure T-like phase BFO film as listed in Table (5.2). These values are far too smaller than the well-known bulk value of Co (~ 31 pJ/m) [72] and A_{ex} measured in Pt/Co/Ir structure ($\sim 12 - 28$ pJ/m) [10], but consistent with A_{ex} measured in Co/oxide heterostructures such as Co(0.6-0.9)/CrO$_x$ (~ 3 pJ/m) [31] and MgO(2)/Co(0.27) ($\sim 2.9 - 3.7$ pJ/m) [88] using the same fitting process.

Parameter η in Eq. (2.24) comes in from the summation of magnon excitation numbers $\langle n_k \rangle_T$. For isotropic Heisenberg model, a gapless dispersion $\omega(k) = D_{sw}k^2$ (using the convention $\hbar = 1$) at the long-wave limit exists, leading to a finite integration $\int dk \, \langle n_k \rangle_T$ in 3D. While 2D (or 1D) integration $\int dk \, \langle n_k \rangle_T$ with a gapless dispersion diverges, this is the reason why we do not have satisfactory fittings through the 3D Bloch 3/2 law for ultrathin Co films in the context of spin wave theory. One way to remedy this problem is to include the anisotropies in isotropic Heisenberg model, such as the two-ion anisotropy term $-K_{ij}S_i^z \cdot S_j^z$ in Eq. (2.25).

Solving the anisotropic Heisenberg model, we have the gapped dispersion, $\omega(k) = \omega_0 + D_{sw}k^2$. Experimentally, the magnon gap ω_0 can be measured from ferromagnetic resonance (FMR) measurement [30, 31].

In this research, we use the H_{A} measured from AHE method at low temperature to estimate $\omega_0 = g\mu_0\mu_B H_A$ [31] as shown in Table (5.2). Using 2D Bloch law (Eq. 2.26), e.g.

$$\Delta M_{2D} = \frac{M(0)k_BT}{4\pi g A_{ex}(0)t} \ln\left[\frac{k_BT}{\hbar\omega_0}\right],$$

where t is the thickness of Co layer. For $k_BT \gg \hbar\omega_0$, we have $\Delta M_{2D} \propto T$, this linear dependence of magnetization (M) with temperature (T) is often observed for ultra-thin ferromagnetic films. Using 2D Bloch law, A_{ex} of Pt/Co(0.5)/T-BFO film is fitted to be 3.0 pJ/m and Pt/Co(0.7)/Pt(0.9)/T-BFO film is fitted to be 4.8 pJ/m. These 2D fitted A_{ex} values have improved as compared with the 3D fittings (Table 5.2), but they are still not satisfactory because the thin Co film is not an ideal 2D system.

A modified Bloch law [30] is introduced by Nembach et al. with a numerically calculated η by summing over all the lattice points of the multilayered structure. When the film thickness is large (20-100 nm), the calculated η value approaches the bulk value (0.0587). As the film thickness decreases, η increases monotonously. According to Nembach et al.'s calculation, here we choose $\eta = 0.3$ to evaluate A_{ex}. Using modified Bloch law with $\eta = 0.3$, A_{ex} of T-BFO/Co(0.5)/Pt sample is fitted to be 5.8 pJ/m and T-BFO/Pt(0.9)/Co(0.7)/Pt sample is fitted to be 9.8 pJ/m.

The exchange stiffnesses estimated by different approaches are listed in Table (5.2), fitting with the modified Bloch law with $\eta = 0.3$ [30] renders the most satisfied values for our samples. The significant increase of A_{ex} is the result of rapid increase of η from bulk value (0.0587) to multilayer value (0.3) and it is the manifesto of dimensional

Sample	A_{ex} (3D Bloch)	$\hbar\omega_0$ (meV)	A_{ex} (2D Bloch)	A_{ex} ($\eta = 0.3$)
Co(0.5)/Pt	2.0 pJ/m	0.116 meV	3.0 pJ/m	5.8 pJ/m
Pt(0.9)/Co(0.7)/Pt	3.3 pJ/m	0.036 meV	4.8 pJ/m	9.8 pJ/m

Table 5.2: Exchange stiffnesses of Co(0.5)/Pt and Pt(0.9)/Co(0.7)/Pt on T-like BFO fitted by different approaches.

effect. For isotropic Heisenberg model, dimension two is actually a critical case.

DMI measurements

The interfacial Dzyaloshinskii-Moriya interaction (DMI) is often found in thin magnetic films with perpendicular anisotropy and structural inversion asymmetry, such as Pt/Co/Ir [10], Pt/Co/AlO$_x$ [89], Pt/Co/MgO [88], Pt/Co(Fe)B/Ir [59], BTO/CoFeB/Ta [65] and even Pt/Co/Pt trilayers with different interface quality [90]. Since the Pt/Co/BFO samples we studied in this chapter have evident asymmetric structures, it's interesting for us to measure the DMI constants for the Co/Pt bilayers on BFO.

The DMI constant D in formula (2.6) can be expressed as

$$D = \mu_0 M_S \delta_{DW} H_{DMI}, \tag{5.4}$$

where $\delta_{DW} = \sqrt{A_{ex}/K_{eff}}$ is the domain wall width, only the DMI field H_{DMI} is unknown to us. To measure the DMI field H_{DMI} of the Co(0.5)/Pt bilayers on both pure T-like phase and mixed phase BFO films, here we use the electrical measurement method based on magnetic droplet nucleation [91].

Because the AHE voltage V_{xy} is proportional to M_z, we can observe the nucleation and propagation of the domain by measuring the AHE voltage of a sample with perpendicular magnetic anisotropy (PMA). The nucleation field H_n can be related with the DW energy σ_{DW} as

$$\mu_0 H_n = \frac{\pi \sigma_{DW}^2 t_{FM}}{2\mu_0 M_S p k_B T} \tag{5.5}$$

where t_{FM} is the thickness for ferromagnetic layer, M_S is the saturation magnetization, p represents the thermal stability factor [89]. When the external magnetic field H_x is applied parallel to the Néel-type domain wall, the domain wall energy $\sigma_{DW}(H_x)$ is given by [92]

$$\sigma_{DW}(H_x) = \begin{cases} \sigma_0 - \frac{\pi^2 \delta_{DW} M_S^2 \mu_0^2}{8K_D}(H_x + H_{DMI})^2 & , \quad \mu_0|H_x + H_{DMI}| < 4K_D/\pi M_S \\ \sigma_0 + 2K_D\delta_{DW} - \pi\delta_{DW}\mu_0\,|H_x + H_{DMI}| & , \quad otherwise \end{cases} \tag{5.6}$$

where K_D is the domain wall anisotropy energy density. Suppose H_{DMI} and K_D are sufficiently large, domain wall energy $\sigma_{DW}(H_x)$ 5.6 can be further simplified as [88, 91]

$$\sigma_{DW}(H_x) = \begin{cases} 2\sigma_0 + 4K_D\delta_{DW} + 2\pi\delta_{DW} M_S \mu_0 H_{DMI} & , \quad |H_x| < |H_{DMI}| \\ 2\sigma_0 + 4K_D\delta_{DW} + 2\pi\delta_{DW} M_S \mu_0 H_x & , \quad otherwise \end{cases} \tag{5.7}$$

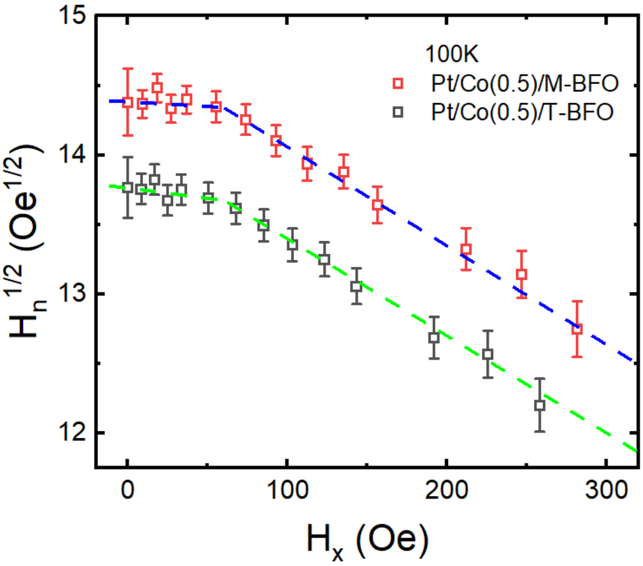

Figure 5.15: $H_n^{1/2}$ versus H_x plots of Co(0.5)/Pt bilayers on mixed phase and pure T-like phase BFO thin films at 100K.

Hence, total domain wall energy $\sigma_{DW}(H_x)$ of the droplet is constant when $|H_x| < |H_{DMI}|$. According to formula (5.5), σ_{DW} is proportional to $H_n^{1/2}$. Thus, if we measure H_n from the AHE curve with different H_x, we can derive H_{DMI} from the $H_n^{1/2}$ vs H_x plots. The disadvantages of using electrical measurement method based on magnetic droplet nucleation are first it cannot determine the sign of the DMI and second it is very time consuming.

We measured the H_{DMI} for Co/Pt bilayers on mixed phase and pure T-like phase BFO film at 150 K, 125 K and 100 K, respectively. No obvious H_{DMI} obtained at 150 K and 125 K. A small $H_{DMI} = 65 \pm 5$ Oe is observed at 100 K as shown in Figure (5.15), leading to a very small DMI constant $\sim$ 0.044 mJ/m^2 at 100 K. As a comparison, Lin et al. [65] have got DMI constants of 5.09 and 8.39 mJ/m^2 for the TiO_2 and BaO-terminated Pt/Fe/BTO heterostructures which are also magnetron sputtered magnetic metal multilayers on PLD grown oxide films. The low T_c and small exchange stiffness A_{ex} of Co(0.5)/Pt on BFO may be the reason why we didn't get larger DMI. Despite the smallness of DMI constants we got so far, more efforts with improved sample quality and experimental methods are needed to study the DMI effects on FM/Ferroelectric heterostructures.

5.3.3 Magnetic Properties of [Co(0.5 nm)/Pt(1.2 nm)]$_4$/Pt(2.8 nm) multilayers on BFO

To achieve room temperature PMA in Co/Pt multilayers on BFO without using the Pt seed layer, we sputtered [Co(0.5)/Pt(1.2)]$_4$/Pt(2.8) multilayer on pure T-like phase and mixed-phase BFO thin films on LAO substrates. It should be noted that the parameters of Co/Pt multilayers we used here, e.g. Co thickness. Pt thickness and repeat number for the Co/Pt stack are widely employed for sputtering Co/Pt multilayers with PMA on Ta buffered silicon substrates. The only exception is the absence of a $\sim$ 2 nm Pt seed layer in our case.

The XRD, XRR and AFM images of the FM/BFO samples are presented in Figure (5.16). Only (001), (002) T-like BFO and LAO peaks are identified in XRD scan (Figure 5.16 a), hence the BFO thin films deposited by PLD are phase pure and without any impurities. The thicknesses of Co, Pt and BFO are estimated by the growth rates of the material as we have described in previous sections on sample fabrication. The thicknesses of pure T-like phase BFO film and mixed phase BFO film are estimated to be $\sim$ 20 nm and $\sim$ 50 nm, respectively. The AFM image of pure T-like phase BFO film (Figure 5.16, d) shows a clear step-terrace featured surface topography and AFM image of mixed phase BFO thin film (Figure 5.16, d) shows many elongated dark regions consist by T/R-phase mixing emerged from the flat T-like phase matrix.

The magnetic properties of the [Co/Pt]$_4$ multilayers on BFO are characterized by AHE method both at room temperature and at low temperatures. Figure 5.17 (a) shows

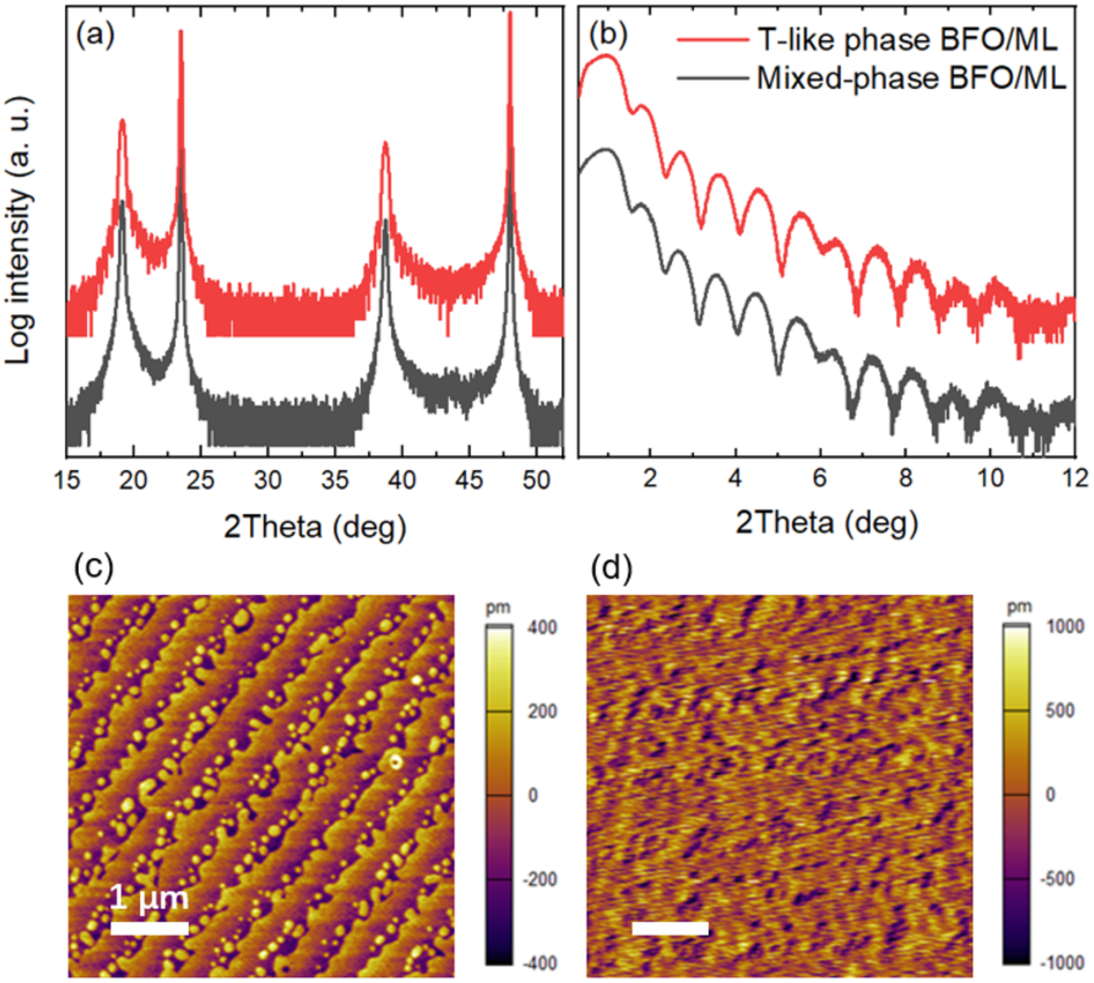

Figure 5.16: (a) XRD $\theta - 2\theta$ scans of a pure T-like phase BFO thin film (red curve) and a mixed phase BFO thin film (black curve) on LAO substrates. (b) XRR scans of $[\mathrm{Co}(0.5)/\mathrm{Pt}(1.2)]_4/\mathrm{Pt}(2.8)$ multilayers on a pure T-like phase BFO film (red curve) and a mixed phase BFO film (black curve). AFM images for $[\mathrm{Co}(0.5)/\mathrm{Pt}(1.2)]_4/\mathrm{Pt}(2.8)$ multilayers covered (c) pure T-like phase BFO and (d) mixed phase BFO films.

the magnetic hysteresis loops measured by AHE method at 310 K, $[\mathrm{Co/Pt}]_4$ multilayers on both pure T-like phase and mixed phase BFO thin films exhibit perpendicular magnetic anisotropy (PMA).

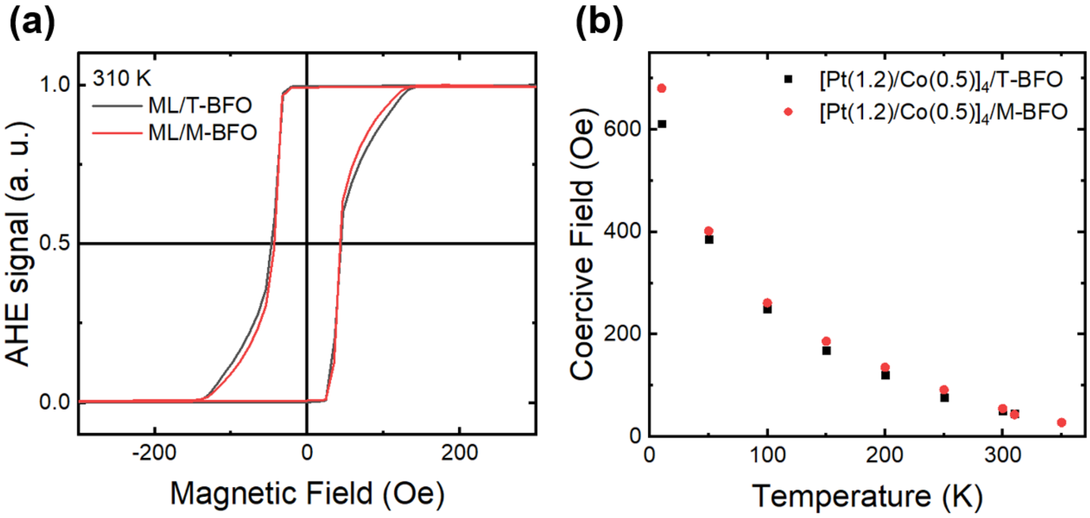

Figure 5.17: (a) AHE signals for $[\mathrm{Co}(0.5)/\mathrm{Pt}(1.2)]_4$ multilayers on pure T-like phase BFO (black curve) and mixed phase BFO (red curve). (b) Temperature dependences of coercive fields H_c for $[\mathrm{Co}(0.5)/\mathrm{Pt}(1.2)]_4$ multilayers on pure T-like phase BFO (black square) and mixed phase BFO (red circle).

The good PMA property of $[\mathrm{Co/Pt}]_4$ multilayers on BFO without using the Pt seed layer proves that absence of the Pt seed layer did not deteriorate the Pt (111) quality of subsequent sputtered Pt layer. Figure 5.17 (b) shows temperature dependences of the coercive fields H_c for $[\mathrm{Co/Pt}]_4$ multilayers sputtered on both mixed phase and pure T-like phase BFO thin films. Both samples have almost identical H_c at room temperature (also Figure 5.17 b), H_c of $[\mathrm{Co/Pt}]_4$ multilayers on mixed-phase BFO film is slightly higher than that of $[\mathrm{Pt/Co}]_4$ multilayers on pure T like-phase BFO film. As a comparison, Pt/Co/Pt trilayer on pure T-like phase BFO has a larger H_c than Pt/Co/Pt on mixed-phase BFO thin film as shown in Figure 5.14 (b).

Without the Pt seed layer sputtered between Co and BFO, the H_c behavior of $[\mathrm{Co/Pt}]_4$ sputtered on BFO is more like the Co directly sputtered on BFO (Figure 5.10 a-c and 5.12) instead of the Co on Pt covered BFO (Figure 5.14 b).

5.4 Summary

In this chapter, we sputtered Co(0.5, 0.7)/Pt directly on BFO thin films without using the seed Pt layer. Weak perpendicular magnetic anisotropies (PMA) were found for Co(0.7)/Pt sputtered on BFO at room temperature. The effective magnetic anisotropies K_{eff} of Pt/Co(0.7)/BFO and Pt/Co(0.7)/Pt(0.6)/BFO are derived from using the area method [70]. Pt/Co(0.7)/T-BFO sample actually has slightly larger K_{eff} ($\sim$ 37 kJ/m^3) than Pt/Co(0.7)/Pt(0.6)/T-BFO sample ($\sim$ 19 kJ/m^3) which means we have slightly higher interface anisotropy at BFO/Co(0.7) than at Pt(0.6)/Co(0.7). The positive contribution of PMA at BFO/Co interface should attribute to the Co-O bondings at the interface [28]. Using XAS method, the Co L_3 edge absorption peaks of Co(1) on mixed phase and pure T-like phase BFO films are investigated. In addition to the main Co peak at 778.6 eV, a shoulder at 779.8 eV is clearly seen for both samples, indicating the existence of CoO at the BFO/Co interface.

Better PMA as evidenced by improved squareness of MH hysteresis loops at low temperatures (below 200 K) are identified for 0.5-nm Co sputtered on BFO thin film. No PMA at room temperature were found for Co(0.5)/Pt sputtered on BFO thin films due to the decreased T_c ($\sim$ 236K) of Pt/Co(0.5)/BFO samples. The perfect squareness of MH hysteresis loops allowed us to measure the anisotropy fields H_A for Pt/Co(0.5)/BFO samples using the AHE method in a planar geometry. A larger anisotropy field was found for Co(0.5) sputtered on mixed phase BFO than on pure T-like phase BFO thin film. On the contrary, a larger H_{A} for Pt(0.9)/Co(0.7)/Pt sputtered on pure T-like phase BFO was found than Pt(0.9)/Co(0.7)/Pt on mixed phase BFO thin film. It is natural to infer that the interface anisotropy induced by BFO/Co has a larger contribution for M-BFO/Co interface than that for T-BFO/Co interface. A thin Pt layer inserted between Co and BFO can block this influence, magnetic properties of Co/Pt multilayers sputtered on Pt covered BFO are mainly influenced by the surface roughness of the underlying BFO as described in chapter 4.

The temperature dependences of intrinsic anisotropies $K_u(T)$ are studied by fitting the $K_u(T)$ vs $M(T)$ data with the Callen-Callen's theory $K_u(T) \propto m^n$, where m is the reduced magnetization. Our results on Pt(4)/Co(0.5)/T-BFO ($n = 2.3$) and Pt(4)/Co(0.7)/Pt(0.9)/T-BFO ($n = 2.1$) deviate from the single-ion $n = 3$ scaling law significantly, indicating dominance of the two-ion anisotropy of both samples. Exchange stiffnesses A_{ex} for both Pt/Co(0.5)/T-BFO and Pt/Co(0.7)/Pt(0.9)/T-BFO are estimated from fitting the $M - T$ curve with 3D Bloch 3/2 law, 2D Bloch law and the modified Bloch 3/2 law. Both 3D Bloch 3/2 law and 2D Bloch law fittings give too small A values ($\sim$ 3 pJ/m) as compared with bulk Co values ($\sim$ 31 pJ/m). Using a numerically calculated $\eta = 0.3$ for ultrathin Co layer, the modified Bloch 3/2 law gives improved A_{ex} values as $\sim$ 5.8 pJ/m for Pt/Co(0.5)/T-BFO and $\sim$ 9.8 pJ/m for Pt/Co(0.7)/Pt(0.9)/T-BFO. Using the A_{ex} value from the modified Bloch 3/2 law fitting, we evaluated the DMI constant for the asymmetric Pt/Co(0.5)/T-BFO sample at 150 K, 125 K and 100 K using the electrical measurement method based on magnetic droplet nucleation. Only the 100 K measurement gives a non-zero DMI constant value of $\sim$ 0.044 mJ/m^2 which is very small as compared with other room temperature PMA systems. The small DMI constant of Pt/Co(0.5)/T-BFO may be attributed to the low Curie temperature T_c and small exchange stiffness A_{ex} of Pt/Co(0.5)/T-BFO.

Lastly, we also studied the magnetic properties of [Co(0.5)/Pt(1.2)]$_4$ multilayers sputtered on BFO. With Co directly sputtered on oxides, PMA was achieved in [Co(0.5)/Pt(1.2)]$_4$ on BFO at room temperature.

Chapter 6

Freestanding Pt/Co/Pt/BFO films

6.1 Introduction

The Co/Pt multilayers with PMA sputtered on epitaxial BFO thin films were prepared and studied in previous chapters. The Pt(t_{Pt})/Co(0.7)/Pt(4) trilayers with a thin Pt seed layer of $t_{\mathrm{Pt}} \sim 1$ nm were studied in Chapter 4, the PMA of this structure is due to the strong spin-coupling interaction occurring at the Co/Pt (111) interface. In Chapter 5, the Co(0.7)/Pt(4) double layers with Co layer directly deposited on BFO also exhibit a weak PMA at room temperature which is slightly larger than that of the Pt(0.6)/Co(0.7)/Pt(4) trilayers on BFO, the $3d$-$2p$ hybridization at the lower Co/BFO interface plays an important role in this case. To utilize the FM/Multiferroic devices in industry, one important task is to integrate the FM/Multiferroic components with the current silicon based technique. In this vision, freestanding complex-oxide membranes [93, 94] are intensively studied recently. Besides this, there are several other motivations for studying the freestanding complex-oxide based devices, such as prospects for flexible electronics, strain engineering beyond substrate limitations and new physics of low dimensional structures.

In this chapter, we exfoliate a thin BFO film capped with a Co/Pt multilayer using a new sacrificial material $\mathrm{SrCoO}_{2.5}$[95, 96], which is soluble in weak acid environment. The Co/Pt multilayer sputtered on BFO acts as the support layer for the exfoliation process on the one hand, and the magnetic layer on the other hand. AHE measurement shows that the Pt(1.2)/Co(0.7)/Pt(4.8) on epitaxial BFO thin film has a rectangular shaped RH hysteresis loop at room temperature which is the sign for PMA. SQUID-VSM measurement on freestanding BFO thin film capped with a Pt(1.2)/Co(0.7)/Pt(4.8) trilayer shows that the PMA has largely survived from the etching, exfoliation and transfer processes. The squareness ratio (M_R/M_S) is estimated to be about 0.75, the weakened PMA is possibly caused by the comparatively high temperature (130°C) which we used for adhering the freestanding BFO with the silicon wafer. As a comparison, the freestanding Pt(4.8)/Co(0.7)/BFO heterostructure without using the Pt seed layer was prepared, which also preserves magnetic properties of the Co(0.7)/Pt(4.8) double-layer on epitaxial BFO.

6.2 Samples and Characterizations

In this chapter, brownmillerite $SrCoO_{2.5}$ (SCO) was used as the sacrificial material which was soluble in weak acid environment [95] to fabricate the freestanding Pt(4.8)/Co(0.7)/Pt(1.2)/BFO (shortened as Pt/Co/Pt/BFO) and Pt(4.8)/Co(0.7)/BFO (shortened as Pt/Co/BFO) heterostructures. Without the constraint of the substrate, the BFO lattices expect to relax to the bulk-like structure (R-like phase) at the freestanding state. Under this consideration, we choose the medium compressed $SrTiO_3$ (001) as the substrate to deposite the epitaxial BFO films. Design and fabrication of freestanding FM/BFO heterotructures are schematically presented in Figure 6.1 (a). Bulk SCO has an orthorhombic structure with a pseudo-cubic lattice ($a_{pc} = 3.905$Å and $c_{pc} = 3.936$Å) which has an identical pseudo-cubic in-plane lattice parameter with STO as shown in Figure 6.1 (b). Resemblance of the in-plane lattice parameters of SCO and perovskite oxides such as SRO and BFO (Figure 6.1 b) plus the high solubility of SCO in eco-friendly weak acids, make SCO an ideal candidate for acting as the sacrificial layer in fabrication of the freestanding complex-oxide membranes.

The high solubility of SCO in weak acids is attributed to the high reaction activity of the ionic bonds in SCO with the hydrogen ions (H^+) within the acids [95], leading to the breakdown of the crystal structure. To construct a conducting channel for hydrogen ions, we deposited a SRO layer on STO before we deposited the SCO sacrificial layer. Here SRO acts as an ion conductor of H^+ between the SCO layer and the weak acid. To reduce the time for dissolving the SCO layer, a large thickness of SRO layer (~ 60 *nm*) and a thin thickness of SCO layer (~ 7 *nm*) was used in this study (Figure 6.1 a).

6.2.1 Epitaxial growth of BFO films on SCO/SRO buffered STO substrates

$BiFeO_3$ films of ~ 35 *nm* were deposited on SCO(~ 7)/SRO(~ 60) buffered $SrTiO_3$ (001) substrates by pulsed laser deposition (PLD), using conditions listed in Table (6.1). A stoichiometric $BiFeO_3$ target was ablated at a high repetition rate of 10Hz using a KrF excimer laser (wave number of 248 *nm*). The STO substrate was glued on the heater at a distance of ~ 6 *cm* from the target. After the ablation, each sample was cooled down to room temperature (RT) at 20°C/min under an oxygen pressure of $\sim$ 1000 Pa. The sample thickness was controlled by the laser pulses with the calibrated growth rate and checked by the X-ray reflectometry measurements.

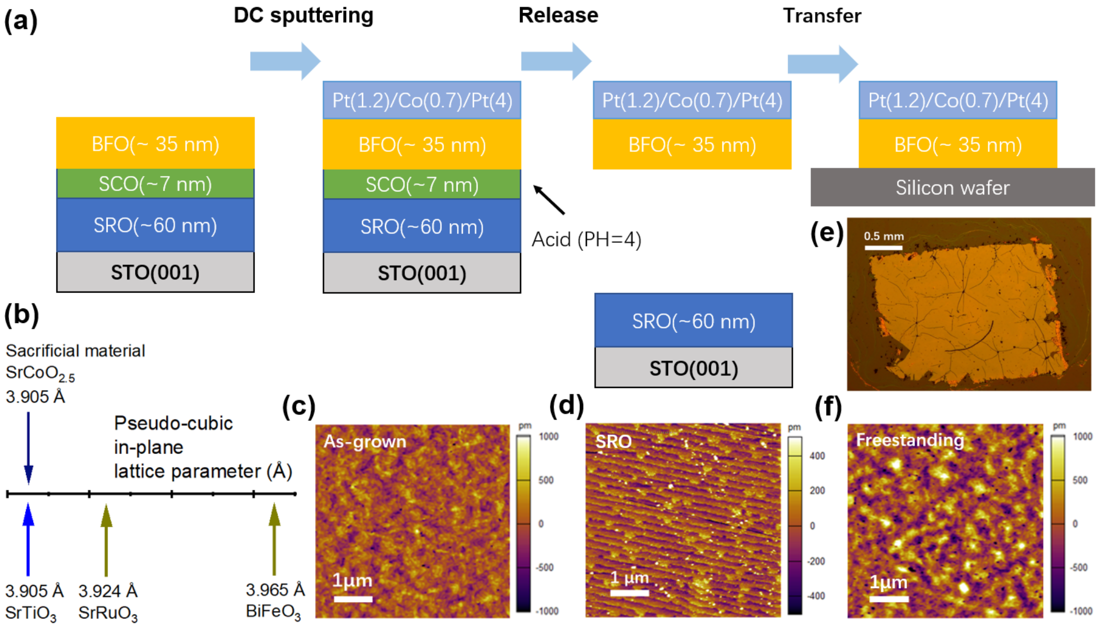

Figure 6.1: Design and fabrication of freestanding Pt/Co/Pt/BFO heterotructures. (a) Schematic illustration of the sputtering, exfoliation and transfer process with SCO as the sacrificial layer. (b) The pseudocubic in-plane lattice parameters of SCO (sacrificial material), STO (substrate), SRO and BFO. (c) The surface morphology of as-grown Pt/Co/Pt/BFO on SCO/SRO/STO(100). (d) The surface morphology of SRO/STO(100) after exfoliation. (e) Optical image of freestanding Pt/Co/Pt/BFO nanomembrane grown on SCO/SRO/STO(001) transferred to a SiO_2/Si substrate. (e) The surface morphology of freestanding Pt/Co/Pt/BFO after exfoliation.

Material	Growth Temperature	Oxygen partial pressure	Laser fluence	Repetition rate
SRO	700 °C	13 Pa	1.5 J/cm^2	10 Hz
SCO	720 °C	13 Pa	1.0 J/cm^2	2 Hz
BFO	680 °C	13 Pa	0.8 J/cm^2	10 Hz

Table 6.1: Growth condition for BFO on SCO/SRO buffered STO (100) substrate.

6.2.2 DC sputtering of Co/Pt multilayers on BFO/SCO/SRO samples

The BFO/SCO/SRO samples were put into the sputtering chamber for DC sputtering immediately after they were taken out of the PLD chamber. Co/Pt multilayers were then deposited by DC magnetron sputtering at room temperature in a 2.0 mTorr Ar atmosphere. Pt and Co targets were sputtered with 30W. The deposition rates were $\sim 1.0\text{Å}/s$ for Pt and $\sim 0.5\text{Å}/s$ for Co. Two series of samples were prepared in this chapter, one is the Pt(1.2)/Co(0.7)/Pt(4) trilayers sputtered on BFO/SCO/SRO heterostructures, another one is the Co(0.7)/Pt(4) bilayers on BFO/SCO/SRO heterostructures. The thicknesses of Pt and Co were controlled by the growth rate of Pt and Co respectively, and checked by X-ray reflectometry measurements. After the sputtering, atomic force microscope (AFM) images were taken for the as-grown FM/BFO/SCO/SRO samples. The AFM image of Pt/Co/Pt trilayers on epitaxial BFO is presented in Figure 6.1 (c), the as-grown Pt/Co/Pt/BFO sample is very flat with a small root mean square (RMS) roughness (R_q) of $\sim 195\ pm$ which signifies high quality of the epitaxial growth.

6.2.3 Fabrication of FM/BFO freestanding membranes

The dimensions of the as-grown Pt/Co/Pt/BFO/SCO/SRO heterostructures are $5\ mm \times 5\ mm$ which are defined by the size of the STO substrates we employed in this study. We then cut the as-grown sample into four pieces for the etching and exfoliation processes, typical areas of the cut samples are between 3-6 mm^2. The heterostructure was put in the $Fe(NO_3)_3$ water solution with a pH value of about 3-4 at room temperature to dissolve the SCO sacrificed layer. The as-grown heterostructure of size 3-6 mm^2 was actually floated on the surface of the $Fe(NO_3)_3$ water solution due to the surface tension.

The thin SCO layer will be reacted with the H^+ ions transported from the weak acid environment through the thick SRO layer. As Peng et al. [95] have suggested that the dissolution process occurred mainly through the SCO/SRO interface, which was essential for obtaining high-quality freestanding membranes. After only a few hours, the SCO layer was completely dissolved in the solution and the FM/BFO heterostructure was successfully released from the SRO coated STO substrate. We then dip the heterostructure in de-ionized water for cleaning. After the cleaning process, we pick up the freestanding FM/BFO heterostructure from the de-ionized water onto a clean silicon wafer (or other substrates). Next, the heterostructure was baked on a hot plate at 130°C for about ten minutes. Finally, the freestanding membrane with an intact size was successfully adhered to the silicon wafer.

The optic image of the freestanding Pt/Co/Pt/BFO membrane was presented in Figure 6.1 (e) which was largely complete and flat. The cracks at the sample surface are results of picking up freestanding heterostructure from the water. The atomically flat topographical surface of the freestanding membrane was presented in Figure 6.1 (f), the root mean square (RMS) roughness (R_q) of the membrane was only $\sim 325\ pm$ which was the same order of magnitude as that of the as-grown Pt/Co/Pt/BFO/SCO/SRO films ($R_q \sim 195\ pm$) in Figure 6.1 (c).

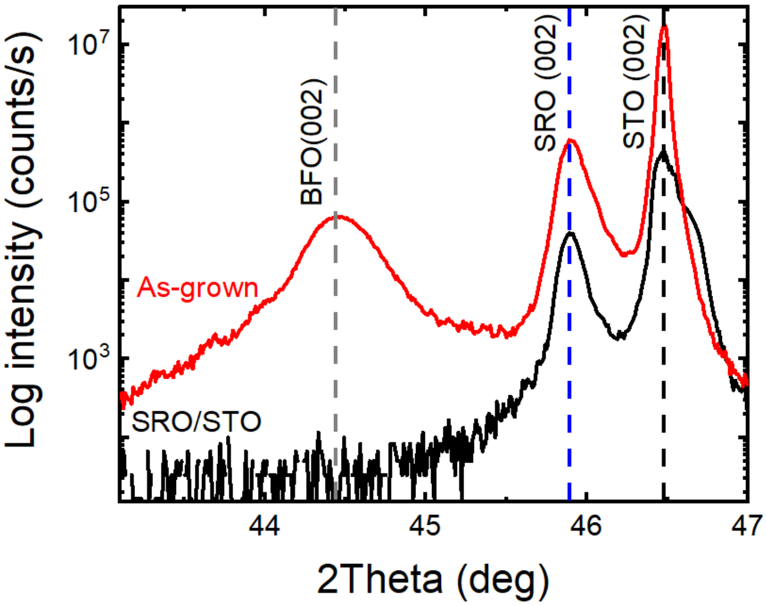

Figure 6.2: XRD $\theta - 2\theta$ plots of the as-grown BFO/SCO/SRO thin film (red curve) and detached SRO/STO film (black curve). The grey dashed line, blue dashed line and black dashed line are used to represent peak positions of BFO (002), SRO (002) and STO (002), respectively.

What is more, the detached SRO/STO film after the exfoliation process was examined by AFM and XRD. The AFM image of the detached SRO/STO film was presented in Figure 6.1 (d) which had an atomically flat step-and-terrace featured topographical surface. In a recent research, Li et al. [97] have revealed that a protonated compound of $HSrRuO_3$ can be formed through ionic liquid gating, accompanied by a notable c-lattice parameter increase. To examine whether the SRO has changed after the exfoliation process, we evaluate the c-lattice parameter of the SRO/STO film after the exfoliation process.

The XRD $\theta - 2\theta$ scans of as-grown BFO/SCO/SRO film and detached SRO/STO film are shown in Figure 6.2. We can see that SRO (002) peak of detached SRO/STO film coincides with SRO (002) peak of as-grown BFO/SCO/SRO film, indicating that the SRO film does not change after the exfoliation process. The SRO c-axis lattice parameter for both samples are estimated to be ~ 3.952 Å, which is in agreement with the result obtained by Peng et al. [95]

6.2.4 X-ray diffraction and structural characterization

X-ray diffraction (XRD) measuremnts, e.g. high-angle $\theta - 2\theta$ scan, low-angle X-ray reflectometry (XRR) and reciprocal space mapping (RSM) were carried out to determine the thickness, crystal structure and lattice parameters of the freestanding nanomembrane as well as the as-grown epitaxial thin film by using a SmartLab X-ray Diffractometer with Cu $K_{\alpha 1}$ radiation ($\lambda = 1.5406$ Å). The good sample quality of the transferred freestanding Pt/Co/Pt/BFO membrane can also be validated through the XRD $\theta - 2\theta$ scan and the XRR measurements.

XRD $\theta - 2\theta$ logarithm plot of the as-grown Pt/Co/Pt/BFO strained film on SCO/SRO buffered STO (001) substrate is shown in red curve of Figure 6.3 (a) where only BFO, SCO, SRO and STO peaks are clearly identified, the Pt (111) peak is vaguely presented around $\sim 40°$ due to the small thickness of the Pt layer. No other impurity phase or secondary phase is presented in the $\theta - 2\theta$ plot showing good crystalline quality of the as-grown epitaxial film. As a comparison, XRD $\theta - 2\theta$ logarithm plot of the freestanding Pt/Co/Pt/BFO nanomembrane is shown in black curve of Figure (6.3) where only BFO (001) and BFO (002) peaks are presented, the Pt (111) peak is barely seen from the plot. Both BFO (001) and BFO (002) peaks shifted to larger values in 2θ, indicating the decrease of the c-lattice parameter from $\sim 4.08 \pm 0.01$ Å to $\sim 3.99 \pm 0.01$ Å after freestanding. Besides, the c-lattice parameter decrease after freestanding was directly identified as comparing the RSM plots of as-grown Pt/Co/Pt/BFO/SCO/SRO sample (Figure 6.3 b) and freestanding Pt/Co/Pt/BFO sample (Figure 6.3 c). The in-plane lattice parameter expansion was also directly testified from the above mentioned RSM plots.

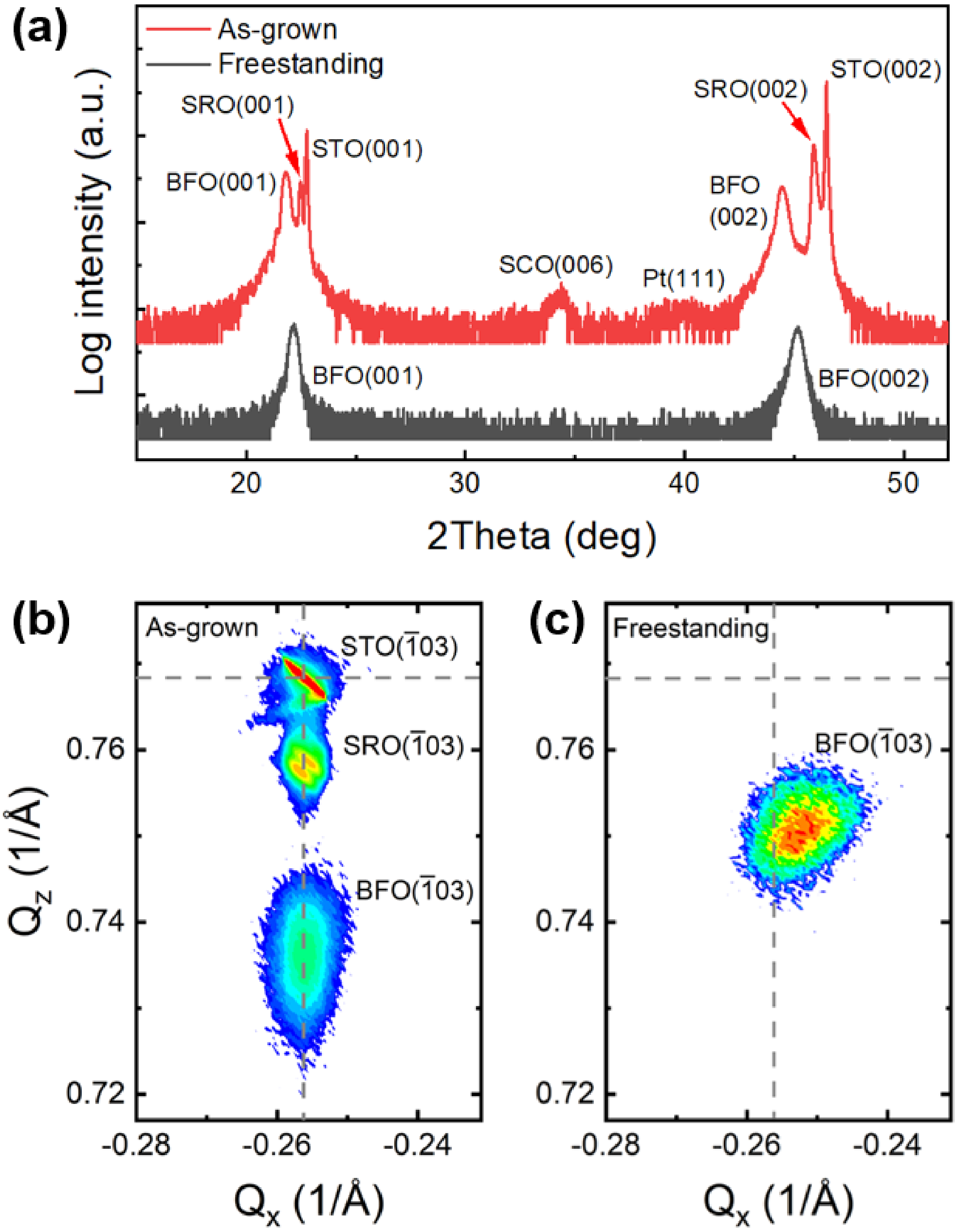

Figure 6.3: (a) XRD $\theta - 2\theta$ scans of the as-grown Pt/Co/Pt/BFO/SCO/SRO films on STO substrate (red) and the freestanding Pt/Co/Pt/BFO nanomembrane. (b) Reciprocal space mapping results of the as-grown Pt/Co/Pt/BFO strained film on SCO/SRO buffered STO (001) substrate measured around the STO ($\bar{1}03$) plane and (c) the corresponding freestanding nanomembrane measured around the BFO ($\bar{1}03$) plane. What is more, the freestanding BFO thin film is fully relaxed due to the calculation of the in-plane lattice constant a.

To figure out in-plane lattice parameter a and c-axis lattice parameter c numerically, we need to determine peak positions of thin film in RSM precisely. Strong diffraction peak caused by the substrate in RSM plot is usually used as the absolute value for calibration. However, absence of substrate in freestanding nanomembrane makes the calibration impossible. To resolve this problem, we first remind the inter-planar distance d_{hkl} in tetragonal crystal lattice:

$$\frac{1}{d_{hkl}^2} = \frac{h^2+k^2}{a^2} + \frac{l^2}{c^2}, \tag{6.1}$$

where c and d_{hkl} are calculated from the $\theta-2\theta$ scans around (001) and (hkl) planes, respectively. Using formula (6.1) and BFO peak positions in Figure 6.3 (a), (c) and Figure (6.4), the in-plane lattice parameter a is estimated to be $\sim 3.96 \pm 0.02$ Å, indicating that BFO lattices in the freestanding Pt/Co/Pt/BFO membrane are fully relaxed. As a comparison, the in-plane lattice parameter a of BFO for the freestanding $La_{0.7}Sr_{0.3}MnO_3(5)/BiFeO_3(40)$ nanomembrane is estimated to be ~ 3.97 Å according to Jin et al. [98]

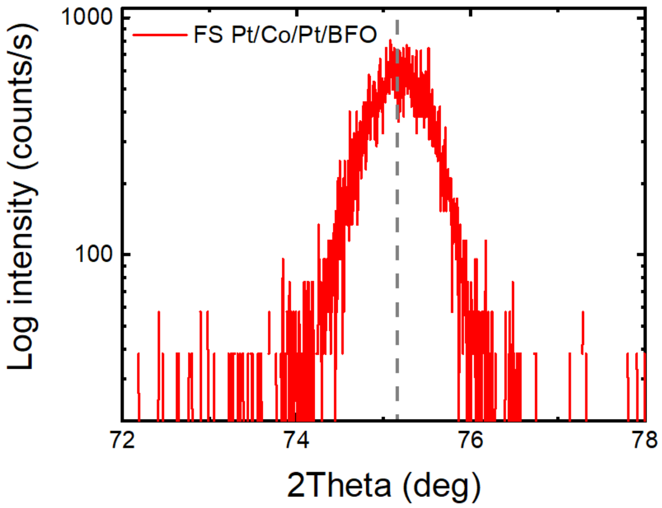

Figure 6.4: XRD $\theta-2\theta$ scan around the BFO($\bar{1}03$) diffraction peak.

The in-plane lattice parameter of BFO before freestanding can be evaluated from RSM plot as shown in Figure 6.3 (b) which was $\sim 3.91 \pm 0.01$ Å, showing a compressive strain for the as-grown sample.

Specular XRR pattern of the freestanding Pt/Co/Pt/BFO membrane is shown in

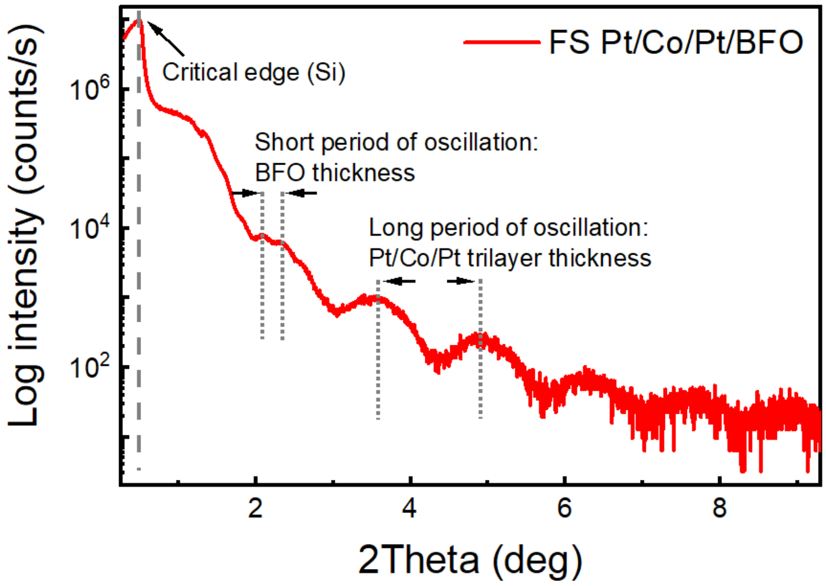

Figure 6.5: Specular XRR pattern of the freestanding Pt/Co/Pt/BFO membrane.

Figure (6.5). As the membrane is transferred onto the silicon wafer, the critical edge labeled by downward arrow is mainly determined by Si which is ~ 0.5. What is more, the short period oscillation was clearly seen from the XRR plot as superimposed on the long period oscillation, which is characteristic of good sample qualities, e.g. small surface roughness and small interface roughness. In addition, the thicknesses of the BFO layer and the Pt/Co/Pt trilayer can be roughly estimated from the short period of oscillation and the long period of oscillation as labeled by short dashed lines in Figure (6.5). The estimated thicknesses are $\sim 35.3\ nm$ for BFO layer and $\sim 6.64\ nm$ for the Pt/Co/Pt trilayer, respectively. The scheduled structure controlled by the growth rates of BFO, Co and Pt is Pt(4.8)/Co(0.7)/Pt(1.2)/BFO(36) which is in a good agreement with the values we estimated from the XRR plot.

6.3 Magnetic Characterization

Magnetic properties of as-grown FM/BFO/SCO/SRO samples (FM = Pt(4.8)/Co(0.7)/Pt(1.2), or Pt(4.8)/Co(0.7)) and freestanding FM/BFO membranes are characterized by using AHE and SQUID-VSM measurements. Since BFO has a very high resistance as compared with metal, the out-of-plane Hall resistance (R_H) vs magnetic field (H) hysteresis curves only include the magnetization (M) contribution from the magnetic metal layers. The R_H vs H curves are measured at room temperature to reveal the $M-H$ hysteresis curves of as-grown Pt/Co/Pt/BFO/SCO/SRO and Pt/Co/BFO/SCO/SRO samples, respectively.

Without the support of substrates, the freestanding FM/BFO nanomembranes transferred onto silicon wafer are expect to be more fragile. To avoid the complexity of making Hall bar structures on freestanding FM/BFO nanomembranes which is certainly feasible for our samples, we just measured the out-of-plane $M-H$ hysteresis loops for both freestanding membranes via SQUID-VSM at room temperature. To compare the magnetic properties of FM/BFO heterostructures before and after freestanding, we just normalized the $R_H - H$ curves for as-grown epitaxial thin films and the $M-H$ curves for freestanding nanomembranes. During SQUID-VSM measurements, we always demagnetize the samples first, and then use small magnetic fields ($< 500\ Oe$) to measure the magnetic moment. Thus, the magnetic contribution from BFO is negligible, and the linear background contribution from sample is always subtracted before normalizing the $M-H$ hysteresis curves.

The normalized $M-H$ hysteresis curves measured at room temperature for as-grown Pt/Co/Pt/BFO/SCO/SRO thin film (measured by AHE) and its corresponding Pt/Co/Pt/BFO freestanding nanomembrane (measured by SQUID-VSM) are presented in Figure 6.6 (a). AHE measurement shows that the Pt/Co/Pt trilayer on epitaxial BFO thin film has a rectangular shaped $M-H$ hysteresis loop which is the sign for PMA (red curve in Figure 6.6 a). SQUID-VSM measurement on freestanding Pt/Co/Pt/BFO nanomembrane shows that the PMA has largely survived from the etching, exfoliation and transfer processes (black curve in Figure 6.6 a). The squareness ratio (M_R/M_S) is estimated to be about 0.75, the weakened PMA is possibly caused by the comparatively high temperature (130°C) which we used for adhering the freestanding BFO with the silicon wafer.

As a comparison, the normalized $M-H$ curves of as-grown Pt/Co/BFO/SCO/SRO thin film measured by AHE (red curve) and its freestanding Pt/Co/BFO nano membrane measured by SQUID-VSM (black curve) are presented in Figure 6.6 (b). Both curves coincide, indicating that the freestanding Pt/Co/BFO nanomembranes can keep the magnetic properties of the as-grown epitaxial Pt/Co/BFO/SCO/SRO in above described SCO (weak acid) based freestanding procedure.

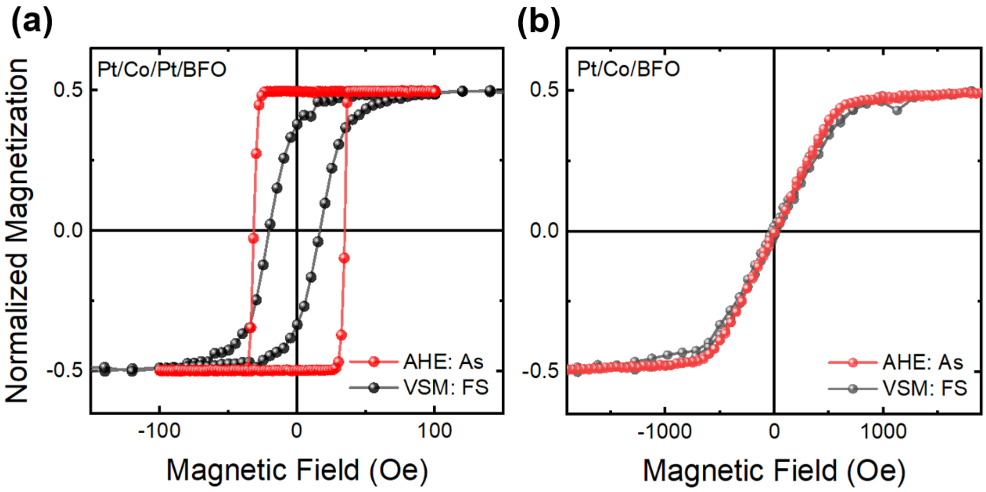

Figure 6.6: (a) Normalized M vs H hysteresis curves measured at room temperature for as-grown Pt/Co/Pt/BFO/SCO/SRO thin film measured by AHE (red) and freestanding Pt/Co/Pt/BFO nanomembrane measured by SQUID-VSM (black). (b) Normalized M vs H hysteresis curves measured at room temperature for as-grown Pt/Co/BFO/SCO/SRO thin film measured by AHE (red) and freestanding Pt/Co/BFO nanomembrane measured by SQUID-VSM (black).

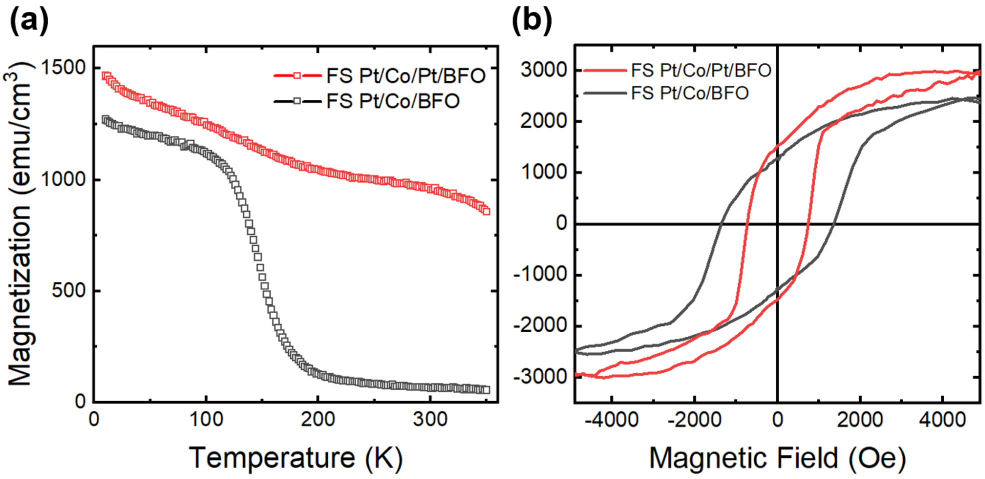

Figure 6.7: (a) Field cooled (FC) M vs T measurements for freestanding Pt/Co/Pt/BFO (red curve) and Pt/Co/BFO (black curve) nanomembranes. (b) M vs H measurements for freestanding Pt/Co/Pt/BFO (red curve) and Pt/Co/BFO (black curve) nanomembranes at 10 K.

The magnetization M vs T of the sample is measured via SQUID-VSM by recording the ZFC and FC magnetic moments. The sample was first cooled down to 10 K in zero field, and then a field of 30 Oe was applied in the out-of-plane direction. The zero field cooled (ZFC) magnetization curve was measured upon warming. Subsequently, the sample was cooled down again to 10 K in 5000 Oe, and then a field of 30 Oe was applied in the out-of-plane direction, the field cooled (FC) curve was recorded during warming.

Figure 6.7 (a) shows the field cooled (FC) magnetization M vs T of the freestanding Pt/Co/Pt/BFO and Pt/Co/BFO nano-membranes, respectively. The Pt/Co/Pt trilayer on freestanding BFO nanomembrane has larger magnetization value ($\sim$ 1450 emu/cm^3 at 10 K) than the Pt/Co bilayer on freestanding BFO nanomembrane ($\sim$ 1280 emu/cm^3 at 10 K) as shown in Figure 6.7 (a, b). The Pt/Co/Pt trilayer on freestanding BFO nanomembrane is a typical PMA sample at room temperature (Figure 6.6 a, black line), while the Pt/Co bilayer on freestanding BFO nanomembrane has a slanted hysteresis curve at room temperature (Figure 6.6 b, black line) and it transforms to an out-of-plane magnetized sample at $\sim$ 172 K when lowering the temperature (Figure 6.7 a, black line).

Figure 6.7 (b) shows the $M-H$ hysteresis loops for freestanding Pt/Co/Pt/BFO (red curve) and Pt/Co/BFO (black curve) nanomembranes at 10 K, respectively. The hysteresis loops are slanted because the SQUID-VSM measured magnetic moment consists of contribution from not only the FM layer, but also the BFO layer and the silicon wafer. To estimate the coercive fields of the FM layer, we shall deduct the contribution from BFO and silicon. Supposing that the magnetic moment of BFO and silicon is linear from -2000 Oe to 2000 Oe, the coercive fields at 10 K are estimated to be $\sim$ 820 Oe for Pt/Co/Pt trilayer and $\sim$ 1850 Oe for Co/Pt bilayer on BFO nanomembrane.

6.4 Summary

In this chapter, freestanding Pt/Co/Pt/BFO and Pt/Co/BFO nanomembranes were fabricated using the weak acid soluble $SrCoO_{2.5}$ (SCO) as the sacrificial layer. Epitaxial BFO films were deposited on SCO/SRO buffered STO substrates via PLD, then Co/Pt multilayers were sputtered on BFO via DC sputtering. SCO reacted with the H^+ ions at the SCO/SRO interface, where the H^+ ions were transported from the weak acid solution to SCO/SRO interface through SRO. Hence, the SCO resolved uniformly throughout the SCO/SRO interface, leading to a quick and high-quality exfoliation of the FM/BFO nanomembranes. Both XRD $\theta - 2\theta$ and RSM ($\bar{1}03$) scans show that the crystal lattices of freestanding BFO are fully relaxed, the in-plane lattice parameter a expands to $\sim 3.96 \pm 0.02$ Å and the c-axis lattice parameter decreases to $\sim 3.99 \pm 0.01$ Å.

AHE measurement shows that the epitaxial Pt/Co/Pt/BFO heterostructure has a rectangular shaped RH hysteresis loop at room temperature which is the sign of PMA. SQUID-VSM measurement on freestanding Pt/Co/Pt/BFO nanomembrane shows that the PMA has largely survived from the etching, exfoliation and transfer processes. The squareness ratio (M_R/M_S) is estimated to be about 0.75, the weakened PMA is possibly due to the comparatively high temperature (130°C) which we used for adhering the freestanding Pt/Co/Pt/BFO nanomembrane with the silicon wafer. As a comparison, the freestanding Pt(4.8)/Co(0.7)/BFO heterostructure was also prepared, which has almost the same magnetic properties with the Co(0.7)/Pt(4.8) double-layer on epitaxial BFO thin films.

Recently, Cheng et al. [99] have prepared freestanding BTO nanomembranes capped with $[\mathrm{Co/Pt}]_5$ magnetic multilayers which exhibit PMA at room temperature. Modulated by strain, the freestanding BTO nanomembranes can be in a wrinkle-patterned shape [100] with a space period of $\sim 15\ \mu m$. To further investigate the magnetic anisotropies of the Co/Pt multilayers influenced by the self-assembled regular patterns shall be a scientifically interesting and technologically important topic.

CHAPTER 7

Conclusions

7.1 Summary

This thesis has explored a full study of Co/Pt based magnetic multilayers on both epitaxial and freestanding $BiFeO_3$ films. As these structures can be applied in energy-efficient computing based on order parameters such as polarization, magnetization and strain [3], the need for understanding how to integrate FE/multiferroic material with FM layer with PMA and further integrate FM/FE (or multiferroic) devices into current silicon-based CMOS technology is of importance. So firstly, an introduction to the context of the work was given, and some required theoretical background was introduced. The experimental methods including the sample preparation techniques we used for this work are described before results of our experimental work. The results are described in three chapters on the basis of sample structure.

The Pt(t_{Pt})/Co(0.7)/Pt trilayers were magnetron sputtered ($t_{\mathrm{Pt}} = 0.6 - 2.4$) at room temperature on pure T-like phase and mixed phase BFO films. The BFO films of various thicknesses are deposited on CCMO buffered LAO substrates via PLD. PMA with square MH hysteresis loops were achieved for Pt seed layer thickness as small as 0.9 nm on both pure T-like and mixed phase BFO. Anisotropy fields H_{A} and effective anisotropy K_{eff} for Pt(t_{Pt})/Co(0.7)/Pt on BFO were measured, we find an increasing tendency of K_{eff} as we increase the Pt seed layer thickness and K_{eff} saturates when t_{Pt} is about 2 nm. Phase influence of BFO on PMA in Pt/Co/Pt structure was also studied by fixing $t_{\mathrm{Pt}} = 0.9, 1.2$. The change in K_{eff} can be explained by the surface anisotropy reduced by roughness $\frac{\Delta K_S}{K_S} = -\frac{2\sigma}{W}$ [62, 63]. Pt/Co/Pt trilayer sputtered on pure T-like BFO usually has a larger K_{eff} than Pt/Co/Pt sputtered on mixed phase BFO due to the smaller σ/W ratio.

To increase the coupling between the FM layer and the FE layer, we sputtered Co(0.5, 0.7) on BFO directly. A weak PMA with slanted MH hysteresis curve was found for Pt/Co(0.7)/BFO film at room temperature and its K_{eff} is slightly higher than Pt/Co(0.7)/Pt(0.6)/BFO. The positive contribution of PMA at Co/BFO interface shall attribute to the Co-O bonding at the interface and the existence of CoO state at Co/BFO interface is verified by examining the Co L_3 edge absorption peaks via XAS measurement. Co(0.5)/BFO sample is paramagnetic at room temperature due to the reduction of the Curie temperature T_c, and it has perfect square MH hysteresis loop below ~ 150 K as demonstrated by AHE. The temperature dependences of anisotropy field H_{A} and effective anisotropy K_{eff} are measured for Co(0.5)/Pt on both pure T-like phase and mixed phase BFO films. Unlike Pt/Co/Pt/BFO samples, Pt/Co(0.5)/M-BFO has a more rectangular shaped MH hysteresis loop and larger H_A than Pt/Co(0.5)/T-BFO. The strengthened surface anisotropy of Co on the mixed phase BFO, as compared with pure T-like phase BFO, should be responsible for this trend. Using SQUID-VSM measured MT curves, temperature dependences of intrinsic anisotropies $K_u(T)$ and magnetization $M(T)$ are studied by fitting the Cllen-Callen power law $K_u(T) \sim m^n$, where m is the reduced magnetization. We got $n = 2.3$ scaling for Pt/Co(0.5)/T-BFO and $n = 2.1$ scaling for Pt/Co(0.7)/Pt(0.9)/T-BFO, both deviate from the single-ion $n = 3$ scaling law significantly, indicating dominance of the two-ion anisotropy of both structures. Exchange stiffnesses A_{ex} are also measured for Pt/Co(0.5)/T-BFO and Pt/Co(0.7)/Pt(0.9)/T-BFO, the optimum values are obtained by using the modified Bloch 3/2 law [30]. The DMI constant for asymmetric Pt/Co(0.5)/T-BFO was measured at 150 K, 125 K and 100 K using the electrical measurement method. Only the 100 K measurement gives a non-zero DMI of ~ 0.044 mJ/m^2. The small DMI constant of Pt/Co(0.5)/T-BFO may be attributed to the low Curie temperature T_c and small exchange stiffness A_{ex}. PMA was also realized for $[\mathrm{Co}(0.5)/\mathrm{Pt}(1.2)]_4$ multilayers sputtered on BFO without using the Pt seed layer at room temperature.

Lastly, freestanding Pt/Co(0.7)/Pt(1.2)/BFO and Pt/Co(0.7)/BFO nanomembranes were fabricated using the weak acid soluble $\mathrm{SrCoO}_{2.5}$ (SCO) as the sacrificial layer. Epitaxial BFO films were deposited on SCO/SRO buffered STO substrates via PLD, then Co/Pt multilayers were sputtered on BFO via magnetron sputtering. SQUID-VSM measurement on freestanding Pt/Co/Pt/BFO nanomembrane shows that the PMA has largely survived from the etching, exfoliation and transfer processes. The squareness ratio (M_R/M_S) is estimated to be about 0.75, the weakened PMA is possibly due to the comparatively high temperature (130°C) which we used for adhering the freestanding Pt/Co/Pt/BFO nanomembrane with the silicon wafer. As a comparison, the freestanding Pt/Co(0.7)/BFO heterostructure has almost the identical MH hysteresis curve with the Co(0.7)/Pt(4) double-layer on epitaxial BFO thin films.

7.2 Future Work

The magnetic domain morphology of Co/Pt multilayers sputtered on BFO (or other FE/multiferroic materials) is a natural extension of this project and more asymmetric structures, e.g. [Ir/Pt/Co]$_n$/BFO and [Pt/Ir/Co]$_n$/BFO are worth a try. Both step-terrace featured T-matrix BFO surface morphology and stripe-patterned mixed phase BFO surface shall influence the domain morphology [64] and domain wall motion of the up sputtered Co-based multilayers. Other than the electrical measurement method based on magnetic droplet nucleation, more methods shall be tried for determining the DMI constant [101], especially the field-driven domain wall motion method by using the magneto-optic Kerr microscope. What is more, FE materials other than BFO, especially the CMOS-compatible FE material HfO$_2$ [102] shall be tried for integrating with the Co-based PMA structure.

BIBLIOGRAPHY

[1] G.E. Moore. No exponential is forever: but ”Forever” can be delayed! [semiconductor industry]. *ISSCC Dig. Tech. Pap.*, 1:20–23, 2003.

[2] R. H. Dennard, F. H. Gaensslen, H.-N. Yu, V. L. Rideout, E. Bassous, et al. Design of ion-implanted MOSFET’s with very small physical dimensions. *IEEE Journal of Solid-State Circuits*, 9:256–268, 1974.

[3] Sasikanth Manipatruni, Dmitri E. Nikonov, and Ian A. Young. Beyond CMOS computing with spin and polarization. *Nature Physics*, 14:338–343, 2018.

[4] R. Landauer. Irreversibility and heat generation in the computing process. *IBM J. Res. Dev.*, 5:183–191, 1961.

[5] B. Dieny and M. Chshiev. Perpendicular magnetic anisotropy at transition metal/oxide interfaces and applications. *Rev. Mod. Phys.*, 89:025008, Jun 2017.

[6] J. T. Heron, J. L. Bosse, Q. He, Y. Gao, M. Trassin, et al. Deterministic switching of ferromagnetism at room temperature using an electric field. *Nature*, 516:370–373, 2014.

[7] N. D’Souza, A. Biswas, H. Ahmad, M. S. Fashami, M. M. Al-Rashid, et al. Energy-efficient switching of nanomagnets for computing: straintronics and other methodologies. *Nanotechnology*, 29:442001, 2018.

[8] Vineeth Mohanan Parakkat, K. R. Ganesh, and P. S. Anil Kumar. Tailoring Curie temperature and magnetic anisotropy in ultrathin Pt/Co/Pt films. *AIP Advances*, 6:056118, 2016.

[9] Marine Schott, Anne Bernand-Mantel, Laurent Ranno, Stefania Pizzini, Jan Vogel, et al. The Skyrmion Switch: Turning Magnetic Skyrmion Bubbles on and off with an Electric Field. *Nano Letters*, 17:1530–6984, 2017.

[10] Philippa M. Shepley, Harry Tunnicliffe, Kowsar Shahbazi, Gavin Burnell, and Thomas A. Moore. Magnetic properties, domain-wall creep motion, and the Dzyaloshinskii-Moriya interaction in Pt/Co/Ir thin films. *Phys. Rev. B*, 97: 134417, 2018.

[11] A. V. Chumak, P. Kabos, M. Wu, C. Abert, C. Adelmann, et al. Advances in magnetics roadmap on spin-wave computing. *IEEE Transactions on Magnetics*, 58:1–72, 2022.

[12] Hamed Vakili, Jun-Wen Xu, Wei Zhou, Mohammad Nazmus Sakib, Md Golam Morshed, et al. Skyrmionicsâ€”computing and memory technologies based on topological excitations in magnets. *Journal of Applied Physics*, 130:070908, 2021.

[13] S Blundell. *Magnetism in Condensed Matter*, chapter 1. Oxford University Press, 2001.

[14] Nicola A. Spaldin. A beginner's guide to the modern theory of polarization. *Journal of Solid State Chemistry*, 195:2–10, 2012.

[15] R. Resta. Theory of the electric polarization in crystals. *Ferroelectrics*, 136(1): 51–55, 1992.

[16] R. D. King-Smith and David Vanderbilt. Theory of polarization of crystalline solids. *Phys. Rev. B*, 47:1651–1654, 1993.

[17] Raffaele Resta. Manifestations of Berry's phase in molecules and condensed matter. *Journal of Physics: Condensed Matter*, 12:R107, 2000.

[18] Nicola A. Hill. Why Are There so Few Magnetic Ferroelectrics? *J. Phys. Chem. B*, 104:6694–6709, 2000.

[19] N. A. Spaldin and R. Ramesh. Advances in magnetoelectric multiferroics. *Nature Materials*, 18:203–212, 2019.

[20] June Hyuk Lee, Lei Fang, Eftihia Vlahos, Xianglin Ke, Young Woo Jung, et al. A strong ferroelectric ferromagnet created by means of spin-lattice coupling. *Nature*, 466:954–958, 2010.

[21] L. W. Martin, Y.-H. Chu, and R. Ramesh. Advances in the growth and characterization of magnetic, ferroelectric, and multiferroic oxide thin films. *Materials Science and Engineering R*, 68:89, 2010.

[22] J. Wang, J. B. Neaton, H. Zheng, V. Nagajan, S. B. Ogale, et al. Epitaxial $BiFeO_3$ Multiferroic Thin Film Heterostructures. *Science*, 299:1719–1722, 2003.

[23] R. J. Zeches, M. D. Rossell, J. X. Zhang, A. J. Hatt, Q. He, et al. A strain-driven morphotropic phase boundary in $\mathrm{BiFeO_3}$. *Science*, 326:977–980, 2009.

[24] J. C. Yang, Q. He, S. J. Suresha, C. Y. Kuo, C. Y. Peng, et al. Orthorhombic $\mathrm{BiFeO_3}$. *Phys. Rev. Lett.*, 109:247606, 2012.

[25] Hongyu An, Qian Xie, Jian Wang, Takumi Sannomiya, Shinji Muraishi, et al. Highly (001) oriented L1-CoPt/TiN multilayer films on glass substrates with perpendicular magnetic anisotropy. *Journal of Vacuum Science & Technology A*, 33:021512, 2015.

[26] Seiji Yoshino, Hiroshi Takagi, Shigeru Tsunashima, Morio Masuda, and Susumu Uchiyama. Perpendicular Magnetic Anisotropy of TbCo Films . *Japanese Journal of Applied Physics*, 23:188, 1984.

[27] Patrick Bruno. *Physical Origins and Theoretical Models of Magnetic Anisotropy*, chapter 24. Ferienkurse des Forschungszentrums Jülich, 1993.

[28] H. X. Yang, M. Chshiev, B. Dieny, J. H. Lee, A. Manchon, and K. H. Shin. First-principles investigation of the very large perpendicular magnetic anisotropy at Fe/MgO and Co/MgO interfaces. *Phys. Rev. B*, 84:054401, 2011.

[29] Assa Auerbach. *Interacting Electrons and Quantum Magnetism*, chapter 2. Springer-Verlag, 1994.

[30] Hans T. Nembach, Justin M. Shaw, Mathias Weiler, Emilie Jué, and Thomas J. Silva. Linear relation between Heisenberg exchange and interfacial Dzyaloshinskii-Moriya interaction in metal films. *Nature Physics*, 11:825–829, 2015.

[31] Ivan A. Yastremsky, Oleksii M. Volkov, Martin Kopte, Tobias Kosub, Sven Stienen, et al. Thermodynamics and Exchange Stiffness of Asymmetrically Sandwiched Ultrathin Ferromagnetic Films with Perpendicular Anisotropy. *Phys. Rev. Applied*, 12:064038, 2019.

[32] H M Christen and G Eres. Recent advances in pulsed-laser deposition of complex oxides. *Journal of Physics: Condensed Matter*, 20:264005, 2008.

[33] Takayuki Konya. X-ray thin-film measurement techniques III. High resolution X-ray diffractometry. *The Rigaku Journal*, 25:2, 2009.

[34] Miho Yasaka. X-ray thin-film measurement techniques V. X-ray reflectivity measurement. *The Rigaku Journal*, 26:2, 2010.

[35] Matts Björck and Gabriella Andersson. *GenX*: an extensible X-ray reflectivity refinement program utilizing differential evolution. *Journal of Applied Crystallography*, 40(6):1174–1178, 2007.

[36] S. de Haan, C. Lodder, and T. J. A. Pompa. The (Anomalous) Hall magnetometer as an analysis tool for high density recording media. *Journal of the Magnetics Society of Japan*, 15:349, 1991.

[37] Noga Eden, Gregory Kopnov, Shachar Fraenkel, Moshe Goldstein, and Alexander Gerber. Longitudinal and transverse magnetoresistance in films with tilted out-of-plane magnetic anisotropy. *Phys. Rev. B*, 99:064432, 2019.

[38] Naoto Nagaosa, Jairo Sinova, Shigeki Onoda, A. H. MacDonald, and N. P. Ong. Anomalous Hall effect. *Rev. Mod. Phys.*, 82:1539–1592, 2010.

[39] Quantum Design. SQUID Magnetometer. `https://www.qdusa.com/products/mpms3.html`, 2021. [Online; accessed 23-August-2022].

[40] Ye Du, Shoma Arai, Shingo Kaneta-Takada, Le Duc Anh, Shutaro Karube, et al. Room-temperature perpendicular magnetic anisotropy of Pt/Co/AlOx trilayers on $SrTiO_3$ (001). *AIP Advances*, 10(10):105010, 2020.

[41] Xiong Deng, Chao Chen, Deyang Chen, Xiangbin Cai, Xiaozhe Yin, et al. Strain engineering of epitaxial oxide heterostructures beyond substrate limitations. *Matter*, 4(4):1323–1334, 2021.

[42] Zuhuang Chen, Zhenlin Luo, Chuanwei Huang, Yajun Qi, Ping Yang, et al. Low-symmetry monoclinic phases and polarization rotation path mediated by epitaxial strain in multiferroic $BiFeO_3$ thin films. *Advanced Functional Materials*, 21:133–138, 2011.

[43] Stuart R. Burns, Oliver Paull, Ralph Bulanadi, Christie Lau, Daniel Sando, et al. Empirical approach to measuring interface energies in mixed-phase bismuth ferrite. *Phys. Rev. Materials*, 5:034404, 2021.

[44] Kanghyun Chu, Byung-Kweon Jang, Ji Ho Sung, Yoon Ah Shin, Eui-Sup Lee, et al. Enhancement of the anisotropic photocurrent in ferroelectric oxides by strain gradients. *Nature Nanotech*, 10:972–979, 2015.

[45] Zuhuang Chen, S. Prosandeev, Z. L. Luo, Wei Ren, Yajun Qi, et al. Coexistence of ferroelectric triclinic phases in highly strained $BiFeO_3$ films. *Phys. Rev. B*, 84: 094116, 2011.

[46] Zoufei Chen, Yadong Wang, Dongfeng Zheng, Fei Sun, Xiong Deng, et al. Polarization tunable and enhanced photovoltaic properties in tetragonal-like $BiFeO_3$ epitaxial films with graphene top electrode. *Journal of Alloys and Compounds*, 811:152013, 2019.

[47] Peilian Li, Zhifeng Huang, Zhen Fan, Hua Fan, Qiuyuan Luo, et al. An Unusual Mechanism for Negative Differential Resistance in Ferroelectric Nanocapacitors: Polarization Switching-Induced Charge Injection Followed by Charge Trapping. *ACS Applied Materials and Interfaces*, 9:1944–8244, 2017.

[48] P. Yu, W. Luo, D. Yi, J. X. Zhang, M. D. Rossell, et al. Interface control of bulk ferroelectric polarization. *PNAS*, 109:9710–9715, 2012.

[49] Q. Zhang, L. You, X. Shen, C. Wan, Z. Yuan, et al. Polarization-Mediated Thermal Stability of Metal/Oxide Heterointerface. *Adv. Mater.*, 27:6934–6938, 2015.

[50] Charles Kittel. *Introduction to Solid State Physics*, chapter 14. John Wiley & Sons, 2005.

[51] Jean Comtet, Antoine Niguès, Vojtech Kaiser, Benoit Coasne, Lydéric Bocquet, et al. Nanoscale capillary freezing of ionic liquids confined between metallic

interfaces and the role of electronic screening. *Nature Materials*, 16:634–639, 2017.

[52] The Thomas-fermi screening potential is $V \sim V_0 e^{-\lambda r}$ with $\lambda^2 = \frac{4}{a_0}\left(\frac{3n_0}{\pi}\right)^{1/3}$, where a_0 is the Bohr radius, n_0 is the electron number density. The screening length can be estimated from $l_{TF} = \frac{1}{\lambda}$.

[53] P. F. Liu, J. Miao, Z. D. Xu, G. Jakob, Q. Liu, et al. Large modulation of perpendicular magnetic anisotropy in a $BiFeO_3/Al_2O_3/Pt/Co/Pt$ multiferroic heterostructure via spontaneous polarizations. *Appl. Phys. Lett.*, 113:062401, 2018.

[54] Hélène Béa, Manuel Bibes, Stéphane Fusil, Karim Bouzehouane, Eric Jacquet, et al. Investigation on the origin of the magnetic moment of $BiFeO_3$ thin films by advanced x-ray characterizations. *Phys. Rev. B*, 74:020101, 2006.

[55] G. J. MacDougall, H. M. Christen, W. Siemons, M. D. Biegalski, J. L. Zarestky, et al. Antiferromagnetic transitions in tetragonal-like $BiFeO_3$. *Phys. Rev. B*, 85: 100406, 2012.

[56] Q. He, Y.-H. Chu, J. T. Heron, S. Y. Yang, W. I. Liang, et al. Electrically controllable spontaneous magnetism in nanoscale mixed phase multiferroics. *Nat Commun*, 2:225, 2011.

[57] Lorenzo Vistoli, Wenbo Wang, Anke Sander, Qiuxiang Zhu, Blai Casals, et al. Giant topological Hall effect in correlated oxide thin films. *Nature Physics*, 15: 67–72, 2019.

[58] Bart F. Vermeulen, Johan Swerts, Sébastien Couet, Mihaela Popovici, Iuliana P. Radu, et al. Electronic voltage control of magnetic anisotropy at room temperature in high-κ $SrTiO_3/Co/Pt$ trilayer. *Phys. Rev. Materials*, 4:114415, Nov 2020.

[59] Khulaif Alshammari, Eloi Haltz, Mohammed Alyami, Mannan Ali, Paul S. Keatley, et al. Scaling of Dzyaloshinskii-Moriya interaction with magnetization in Pt/Co(Fe)B/Ir multilayers. *Phys. Rev. B*, 104:224402, 2021.

[60] T. Koyama, A. Obinata, Y. Hibino, A. Hirohata, B. Kuerbanjiang, et al. Dependence of Curie temperature on Pt layer thickness in Co/Pt system. *Appl. Phys. Lett.*, 106:132409, 2015.

[61] Motohiro Suzuki, Hiroaki Muraoka, Yuuki Inaba, Hayato Miyagawa, Naomi Kawamura, et al. Depth profile of spin and orbital magnetic moments in a subnanometer Pt film on Co. *Phys. Rev. B*, 72:054430, 2005.

[62] P Bruno. Magnetic surface anisotropy of cobalt and surface roughness effects within Néel's model. *J. Phys. F: Met. Phys.*, 18:1291, 1988.

[63] D Sander. The magnetic anisotropy and spin reorientation of nanostructures and nanoscale films. *Journal of Physics: Condensed Matter*, 16:R603, 2004.

[64] Joonghoe Dho. Aligned stripe magnetic domains in a Pt/Co/Pt film induced by a step-terrace substrate. *Journal of Magnetism and Magnetic Materials*, 545: 168765, 2022.

[65] Weinan Lin, Baishun Yang, Andy Paul Chen, Xiaohan Wu, Rui Guo, et al. Perpendicular Magnetic Anisotropy and Dzyaloshinskii-Moriya Interaction at an Oxide/Ferromagnetic Metal Interface. *Phys. Rev. Lett.*, 124:217202, May 2020.

[66] Yen-Lin Huang, Dmitri Nikonov, Christopher Addiego, Rajesh V. Chopdekar, Bhagwati Prasad, et al. Manipulating magnetoelectric energy landscape in multiferroics. *Nat Commun*, 11:2836, 2020.

[67] A. Manchon, C. Ducruet, L. Lombard, S. Auffret, B. Rodmacq, et al. Analysis of oxygen induced anisotropy crossover in Pt/Co/MOx trilayers. *Journal of Applied Physics*, 104:043914, 2008.

[68] Zeyu Zhang, Zhipeng Li, Kangkang Meng, Yong Wu, Jikun Chen, et al. Perpendicular magnetic anisotropy in $SrTiO_3$/Co/Pt films induced by oxygen diffusion from $CaTiO_3$ spacer layer. *Appl. Phys. Lett.*, 116:232402, 2020.

[69] Chong Bi, Yaohua Liu, T. Newhouse-Illige, M. Xu, M. Rosales, et al. Reversible Control of Co Magnetism by Voltage-Induced Oxidation. *Phys. Rev. Lett.*, 113: 267202, 2014.

[70] M T Johnson, P J H Bloemen, F J A den Broeder, and J J de Vries. Magnetic anisotropy in metallic multilayers. *Reports on Progress in Physics*, 59:1409, 1996.

[71] J. D. Livingston. A review of coercivity mechanisms (invited). *Journal of Applied Physics*, 52:2544, 1981.

[72] J. M. D. Coey. *Magnetism and Magnetic Materials*, chapter 7. Cambridge University Press, 2009.

[73] R. Moreno, R. F. L. Evans, S. Khmelevskyi, M. C. Muñoz, R. W. Chantrell, et al. Temperature-dependent exchange stiffness and domain wall width in Co. *Phys. Rev. B*, 94:104433, 2016.

[74] Y.-C. Chen, Q. He, F.-N. Chu, Y.-C. Huang, J.-W. Chen, et al. Electrical Control of Multiferroic Orderings in Mixed-Phase $BiFeO_3$ Films. *Adv. Mater.*, 24:3070–3075, 2012.

[75] Andrew P. Roberts, Yulong Cui, and Kenneth L. Verosub. Wasp-waisted hysteresis loops: Mineral magnetic characteristics and discrimination of components in mixed magnetic systems. *Journal of Geophysical Research: Solid Earth*, 100: 17909–17924, 1995.

[76] Q. T. Zhang, L. You, C. H. Wan, Z. H. Yuan, X. Zhang, et al. Influence of epitaxial $BiFeO_3$ on superparamagnetic behavior of CoFeB thin film. *Journal of Applied Physics*, 117:143904, 2015.

[77] S. Blundell. *Magnetism in Condensed Matter*, chapter 6. Oxford University Press, 2001.

[78] Claude Ederer and Nicola A. Spaldin. Weak ferromagnetism and magnetoelectric coupling in bismuth ferrite. *Phys. Rev. B*, 71:060401, 2005.

[79] P. M. Shepley, A. W. Rushforth, M. Wang, G. Burnell, and T. A. Moore. Modification of perpendicular magnetic anisotropy and domain wall velocity in Pt/Co/Pt by voltage-induced strain. *Scientific Reports*, 5:7921, 2015.

[80] Earl Callen and Herbert B. Callen. Magnetostriction, Forced Magnetostriction, and Anomalous Thermal Expansion in Ferromagnets. *Phys. Rev.*, 139:A455–A471, 1965.

[81] B. D. Cullity and C. D. Graham. *Introduction to magnetic materials (2nd edition)*, chapter 7. IEEE Press, 2009.

[82] Richard F. L. Evans, Levente Rózsa, Sarah Jenkins, and Unai Atxitia. Temperature scaling of two-ion anisotropy in pure and mixed anisotropy systems. *Phys. Rev. B*, 102:020412, 2020.

[83] R. Skomski, A. Kashyap, and D. Sellmyer. Finite-temperature anisotropy of PtCo magnets. *IEEE Trans. Magn.*, 39:2917, 2003.

[84] O. N. Mryasov, U. Nowak, K. Y. Guslienko, and R. W. Chantrell. Temperature-dependent magnetic properties of FePt: Effective spin Hamiltonian model. *Europhysics Letters*, 69:805, 2005.

[85] S. Okamoto, N. Kikuchi, O. Kitakami, T. Miyazaki, Y. Shimada, et al. Chemical-order-dependent magnetic anisotropy and exchange stiffness constant of FePt (001) epitaxial films. *Phys. Rev. B*, 66:024413, 2002.

[86] H. Sato, P. Chureemart, F. Matsukura, R. W. Chantrell, H. Ohno, et al. Temperature-dependent properties of CoFeB/MgO thin films: Experiments versus simulations. *Phys. Rev. B*, 98:214428, 2018.

[87] Sarah Schlotter, Parnika Agrawal, and Geoffrey S. D. Beach. Temperature dependence of the Dzyaloshinskii-Moriya interaction in Pt/Co/Cu thin film heterostructures. *Appl. Phys. Lett.*, 113:092402, 2018.

[88] Woo Seung Ham, Mio Ishibashi, Kwangsu Kim, Sanghoon Kim, and Teruo Ono. Observation of temperature-dependent Dzyaloshinskii-Moriya interaction within the 50-300 K range. *Japanese Journal of Applied Physics*, 61:020901, 2022.

[89] S. Pizzini, J. Vogel, S. Rohart, L. D. Buda-Prejbeanu, E. Jué, et al. Chirality-Induced Asymmetric Magnetic Nucleation in Pt/Co/AlO$_x$ Ultrathin Microstructures. *Phys. Rev. Lett.*, 113:047203, 2014.

[90] Adam W. J. Wells, Philippa M. Shepley, Christopher H. Marrows, and Thomas A. Moore. Effect of interfacial intermixing on the Dzyaloshinskii-Moriya interaction in Pt/Co/Pt. *Phys. Rev. B*, 95:054428, 2017.

[91] Sanghoon Kim, Peong-Hwa Jang, Duck-Ho Kim, Mio Ishibashi, Takuya Taniguchi, et al. Magnetic droplet nucleation with a homochiral Néel domain wall. *Phys. Rev. B*, 95:220402, 2017.

[92] Soong-Geun Je, Duck-Ho Kim, Sang-Cheol Yoo, Byoung-Chul Min, Kyung-Jin Lee, et al. Asymmetric magnetic domain-wall motion by the Dzyaloshinskii-Moriya interaction. *Phys. Rev. B*, 88:214401, 2013.

[93] David Pesquera, Abel FernÃ¡ndez, Ekaterina Khestanova, and Lane W Martin. Freestanding complex-oxide membranes. *Journal of Physics: Condensed Matter*, 34:383001, 2022.

[94] Francesco M. Chiabrera, Shinhee Yun, Ying Li, Rasmus T. Dahm, Haiwu Zhang, et al. Freestanding Perovskite Oxide Films: Synthesis, Challenges, and Properties. *Annalen der Physik*, page 2200084, 2022.

[95] Huining Peng, Nianpeng Lu, Shuzhen Yang, Yingjie Lyu, Zhiwei Liu, et al. A Generic Sacrificial Layer for Wide-Range Freestanding Oxides with Modulated Magnetic Anisotropy. *Adv. Funct. Mater.*, 32:2111907, 2022.

[96] Weikun Zhou, Wenqiao Han, Yihao Yang, Liang Shu, Qinggui Luo, et al. Synthesis of freestanding perovskite oxide thin films by using brownmillerite $SrCoO_{2.5}$ as a sacrificial layer. *Appl. Phys. Lett.*, 122:062901, 2023.

[97] Zhuolu Li, Shengchun Shen, Zijun Tian, Kyle Hwangbo, Meng Wang, et al. Reversible manipulation of the magnetic state in $SrRuO_3$ through electric-field controlled proton evolution. *Nature Communications*, 11:184, 2020.

[98] Cai Jin, Yuanmin Zhu, Wenqiao Han, Qi Liu, Sixia Hu, et al. Exchange bias in flexible freestanding $La_{0.7}Sr_{0.3}MnO_3/BiFeO_3$ membranes. *Appl. Phys. Lett.*, 117: 252902, 2020.

[99] Yuxin Cheng, Guohua Dong, Yaojin Li, Guannan Yang, Butong Zhang, et al. Strain Modulation of Perpendicular Magnetic Anisotropy in Wrinkle-Patterned $(Co/Pt)_5/BaTiO_3$ Magnetoelectric Heterostructures. *ACS Nano*, 16:11291–11299, 2022.

[100] Guohua Dong, Suzhi Li, Tao Li, Haijun Wu, Tianxiang Nan, et al. Periodic Wrinkle-Patterned Single-Crystalline Ferroelectric Oxide Membranes with Enhanced Piezoelectricity. *Adv. Mater.*, 32:2004477, 2020.

[101] M. Kuepferling, A. Casiraghi, G. Soares, G. Durin, F. Garcia-Sanchez, et al. Measuring interfacial Dzyaloshinskii-Moriya interaction in ultrathin magnetic films. Rev. Mod. Phys. (accepted), 2022.

[102] Bart F. Vermeulen, Florin Ciubotaru, Mihaela I. Popovici, Johan Swerts, Sébastien Couet, et al. Ferroelectric Control of Magnetism in Ultrathin HfO_2/Co/Pt Layers. *ACS Appl. Mater. Interfaces*, 11:34385–34393, 2019.